High-Speed Quasi-Distributed Optical Fiber Sensing Based on Ultra-Weak Fiber Bragg Gratings

Lingmei Ma

Dissertation submitted to the faculty of the

Virginia Polytechnic Institute and State University

in partial fulfillment of the requirements for the degree of

Doctor of Philosophy

In

Electrical Engineering

Anbo Wang, Chair

Aloysius A. Beex

Gary R. Pickrell

Yong Xu

Yizheng Zhu

11/30/2016

Blacksburg, VA

Keywords: fiber Bragg grating, ultra-weak, sensing, fiber dispersion

High-Speed Quasi-Distributed Optical Fiber Sensing Based on Ultra-Weak Fiber Bragg Gratings

Lingmei Ma

ABSTRACT

Invention of silica based optical fiber not only led to revolution in communication but also provided fundamental basis for many research areas. One example area is distributed optical fiber sensing, which has been attracting research interests for decades. Optical fiber sensors are immune to electromagnetic interference, and resistant to corrosion and can endure harsh environment so they have found applications such as structural health monitoring, intrusion detection and oil downhole measurement.

Significant research efforts have been paid to fiber sensing area, many techniques have been developed and some of them have been successfully demonstrated, however achieving both high-speed and long-range is still under intensive research.

This dissertation proposes and demonstrates a technique with the capability of simultaneous long-range and high-speed sensing by employing serial ultra-weak fiber Bragg gratings (UW-FBGs) and dispersive components. Various factors which have influence on the system performance, including wavelength resolution, spatial resolution and sensing rate, are analyzed. Different types of light sources and dispersive units were designed and a sensing system was built. With this system, both static and dynamic response were measured, and a sensing link consisting of more than 2000 UW-FBGs was successfully measured at the speed of 20kHz. The noise sources of the system were also theoretically analyzed and experimentally measured. This demonstrated sensing technique can be applied to long range temperature and strain sensing.

High-Speed Quasi-Distributed Optical Fiber Sensing Based on Ultra-Weak Fiber Bragg Gratings

Lingmei Ma

GENERAL AUDIENCE ABSTRACT

Optical fiber is a thin glass rod with normally two layers of slightly different silica. Because of its low loss, optical fiber can guide light for a long distance without causing significant signal fading. Modifications can be made to a small section of an optical fiber to form a fiber Bragg grating, whose optical characteristics are dependent on its temperature or the strain applied to it.

This dissertation proposes a technique with the ability of measuring the temperature or strain of a long length of optical fiber which has large quantity of fiber Bragg gratings fabricated in it. Along with the capability of long range sensing, this technique also has high sensing speed. It has been demonstrated that the sensing system could perform measurement in every 50μs when the optical fiber has about 2000 fiber Bragg gratings in it. The resolution, if converted to temperature, is about 1.5°C and the accuracy is 2°C.

With the ability of monitoring temperature or strain of a large span at high speed, this technique could be used in areas such as civil structure and air craft health monitoring, instruction detection and high speed temperature monitoring.

Acknowledgements

I would like to express my deepest appreciation to my academic advisor Dr. Anbo Wang. Because of Dr. Wang's trust that I could get a chance to be a member of this excellent group, in which I could improve myself, and because of his continuous support, encouragement and guidance that I could carry on and complete this research. Outside academic area, Dr. Anbo Wang is also a role model for me and I learnt optimistic attitude toward life from him. I would also like to extend my gratitude to my other committee members: Dr. Louis Beex, Dr. Gary R. Pickrell, Dr. Yong Xu and Dr. Yizheng Zhu, thank you for the valuable comments and support during this work.

I am also in debt of gratitude to the members of CPT. Thanks to Dr. Yunjing Wang, Dr. Cheng Ma and Dr. Bo Dong for the valuable discussions and advices in the research. Thanks to Mr. Zhipeng Tian, Mr. Di Hu, Mr. Li Yu, Miss Jing Wang, Mr. Amiya Behera and Mr. Yunbin Song, for their support and help.

Finally I would like to thank my family. The unconditional support from my parents helped me to overcome all the difficulties that I encountered. My brothers' encouragement, care and advices also guided me through frustrations. Without all the love and support from my family members, this work could not have been completed.

Table of Contents

List of Figures

List of Tables

Acronyms and Abbreviations

ADC	Analog-to-Digital Converter
APD	Avalanche Photodiode
ASE	Amplified Spontaneous Emission
AWG	Arrayed Waveguide Grating
BOTDA	Brillouin Optical Time-Domain Analyzer
CDMA	Code Division Multiple Access
DCF	Dispersion Compensating Fiber
EDFA	Erbium-Doped Fiber Amplifier
ENOB	Effective Number of Bits
EOM	Electro-Optic Modulator
FBG	Fiber Bragg Grating
FWHM	Full Width at Half Maximum
IFPI	Intrinsic Fabry-Perot Interferometer
LED	Light Emitting Diodes
OFDR	Optical Frequency Domain Reflectometry
OPD	Optical Path Difference
OTDR	Optical Time Domain Reflectometry
PMD	Polarization Mode Dispersion
PRBS	Pseudorandom Bit Sequence
SBS	Stimulated Brillouin Scattering
SLD	Superluminescent Diode
SNR	Signal to Noise Ratio
SOA	Semiconductor Optical Amplifier
SVEA	Slow Varying Envelop Approximation
T-LPG	Traveling Long Period Grating
TDM	Rime Division Multiplexing

UW-FBG	Ultra-Weak Fiber Bragg Gratings
UV	Ultra-Violet
WDM	Wavelength Division Multiplexing

Chapter 1 Introduction

For their compact size, light weight, immunity to electromagnetic interference, high sensitivity and large bandwidth, fiber optic sensors have gained success in various areas, such as civil structure health condition assessment [1-3], aircraft health monitoring [4, 5], gas sensing [6, 7], oil well downhole pressure monitoring [8-11], intrusion detection [12-15] and biochemical detection [16-20]. For the low loss of optical fiber, signal can travel large distance without experiencing significant degradation, and this enables fiber optical sensing the ability of large scale sensing in either fully or quasi distributed manner.

1.1 Fully distributed fiber sensing

Fully distributed sensing means theoretically speaking measurand of any desired position is addressable, and can be based on various nonlinear optical effects. The most successful examples are the sensing systems for temperature or strain measurement based on stimulated Brillouin scattering (SBS) or spontaneous Raman scattering (SRS) [21-30]. Optical Kerr effect has also been used for fully distributed temperature sensing [31, 32], but attracts less attention comparing those using SBS or SRS because high power pump is essential for the Kerr effect based approach. Besides, Rayleigh backscattering, traveling long period grating (T-LPG), phase perturbation and cladding fluorescence can also be used to realize fully distributed sensing for various measurands [6, 13, 19, 33-39].

The backscattered signals can be analyzed using various methods, such as spectrum analysis, optical time domain reflectometry (OTDR) and optical frequency domain reflectometry (OFDR). The rest of this section introduces examples of some of the fully distributed sensing systems classified by the interrogation techniques.

1.1.1 Brillouin optical time-domain analyzer

Stimulated Brillouin scattering is a process in which a relatively strong incident light (pump) can generate a backscattered light with downshifted frequency v_B due to electrostriction [40]. v_B depends on the characteristics of the fiber and is usually around 10GHz in silica fiber. SBS can provide a gain in power to another counter propagating

light (probe) as long as its frequency lies in the range of the backscattered light from the pump. Since the gain peak is dependent on temperature and strain, fully distributed temperature or strain sensing can be realized by characterizing the gain profile as a function of position [21-25]. Some alternative methods measure the loss spectrum of the pump but its operating principle is essentially the same [26, 27].

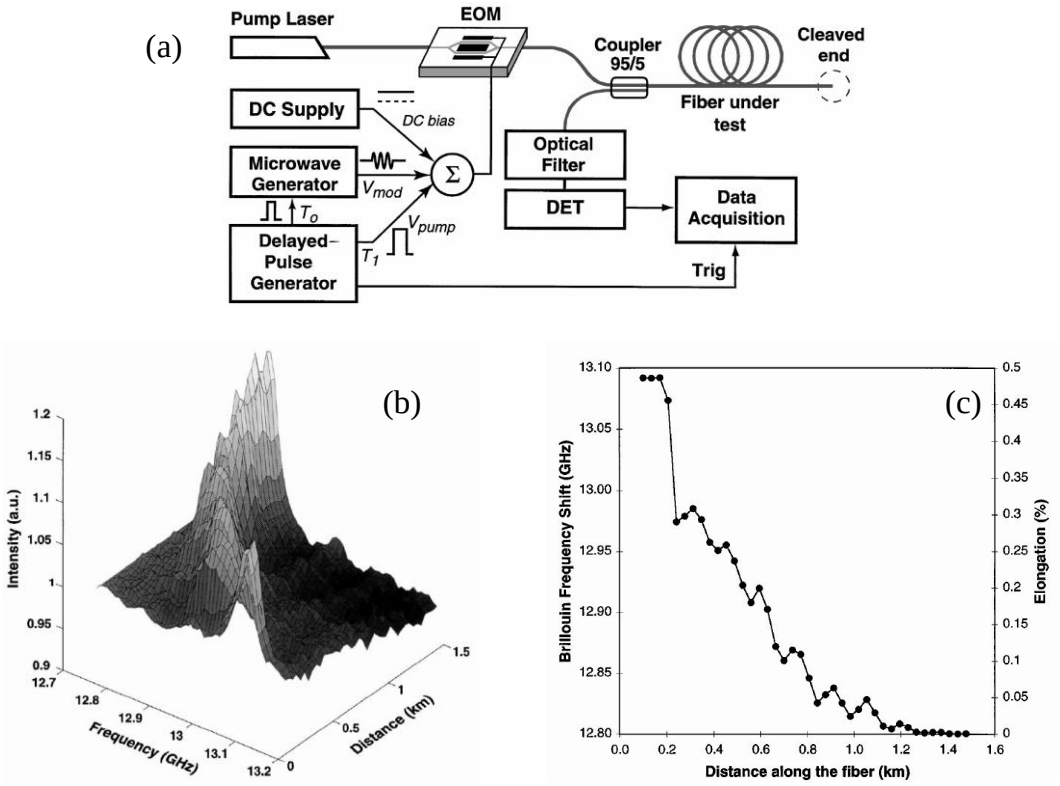

Figure 1-1 Experiment setup and results of a BOTDA system [21] (a) Setup of the experiment. (b) Distributed Brillouin gain profile. (c) Brillouin frequency shift and corresponding strain along the fiber

Figure 1-1(a) shows a Brillouin optical time-domain analyzer (BOTDA) system for distributed strain sensing [21]. Continuous wave (CW) with frequency of f_0 from a laser is modulated by an electro-optic modulator (EOM) which is driven by a specially configured electric signal, producing two pulses with a differential delay of ΔT. The first pulse, which is used as a probe, has an additional modulation at frequency f_m and this modulation will create two side bands in the spectrum of the probe pulse, one of which is downshifted by f_m from the original frequency and the other is upshifted by the same amount. The second pulse works as the pump and its frequency is unchanged. When f_m is close to ν_B, the downshifted frequency component of the probe lies in the gain spectrum

of the probe pulse, so after being reflected by the far end of the sensing fiber, it will meet the delayed forward propagating pump pulse at a certain position and will get amplified. By monitoring the amplitude of the reflected probe pulse while scanning f_m, Brillouin gain spectra could be obtained. SBS gain spectra of different positions can be addressed by changing the delay ΔT between the two pulses.

Figure 1-1(b) and (c) show the results obtained by the experiment setup in Figure 1-1(a). A length of 1.4km fiber was interrogated using a 50ns long pulse and strain was measured with a spatial resolution of 45m. The spatial resolution depends on the pulse width and delay tuning in this scheme so it could be improved by reducing the pulse width and using more precise delay tuning. However, the threshold of SBS increases as the pulse width gets smaller and SBS can hardly occur when the pump pulse is narrower than 1ns [41], so the spatial resolution is limited to the order of meters. Various schemes have been developed to improve the spatial resolution down to the order of millimeters, while the highest speed is several tens of hertz for a sensing range of several hundreds of meters [4, 25, 42, 43].

It should be noted that for BOTDA, sensing speed is essentially limited by the nature of gain spectrum measurement, which requires frequency scanning. Also, to get a high signal to noise ratio (SNR), data averaging is required, which again compromises the sensing speed. For large scale sensing, the speed is generally on the order of hertz. Comparing with the other fully distributed sensing technologies to be described in the rest of this section, BOTDA has faster response but it is not high enough for dynamic measurement in long sensing distance.

1.1.2 Optical time-domain reflectometry

Optical time domain reflectometry (OTDR) is a technique which characterizes fiber by monitoring the distributed Rayleigh backscattering from the fiber [44]. However, by utilizing other backscattering signals, for example, Raman, along with other signal demodulation techniques, its application has been broadened to detection of various parameters, such as temperature, polarization mode dispersion (PMD) and strain [28, 33-35].

Raman OTDR has been successfully used to perform fully distributed temperature measurement. The mechanism of Raman OTDR is that the power ratio of anti-Stokes and Stokes signals from spontaneous Raman scattering has a temperature dependence given by [28]:

$$R(T) = \left(\frac{\lambda_s}{\lambda_a}\right)^4 \exp\left(\frac{hc\kappa}{kT}\right) \tag{1.1}$$

where λ_a and λ_s are the wavelengths of anti-Stokes and Stokes signals, κ is the wavenumber separation from the incident signal, h is Plank's constant, c is the velocity of light in vacuum and T is the absolute temperature of the position where scattered light comes from.

Figure 1-2(a) illustrates a distributed temperature sensing system using spontaneous Raman scattering and the corresponding results are given in Figure 1-2 (b). The laser diode gives a pulsed output with high peak power at a certain repetition rate. After the beam splitter, part of the power is coupled into the sensing fiber and experiences back scattering, and the scattered light will meet the grating after being deflected by the beam splitter. Since the Stokes, anti-Stokes and incident signal have different frequencies, the grating can separate them in the spatial domain. By adjusting the position of fiber pigtail of the avalanche photodiode (APD), the Stokes, anti-Stokes or Rayleigh scattering signal can be picked up by the APD and then amplified. Temperature can be calculated using Equation 1.1 from the levels of the anti-Stokes and Stokes signals.

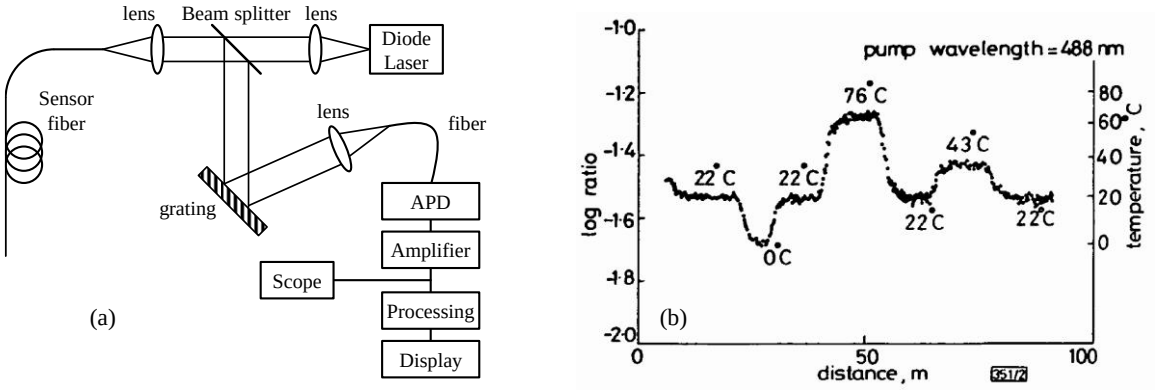

Figure 1-2 Temperature sensing system using Raman-OTDR [28] (a) Experiment setup (b) Distributed temperature sensing result

Spontaneous Raman scattering is rather weak so that a lot of data averaging is required to get a decent SNR, and consequently speed is rather low. The spatial resolution is determined by the width of the incident pulse so using shorter pulse will give better spatial resolution at the expense of a lower SNR and a system higher cost. Typical spatial resolution is on the order of meters and it may take minutes to finish one measurement.

Other configurations based on Rayleigh scattering are also developed to demonstrate fully distributed sensing using the OTDR technique. Figure 1-3 illustrates a polarization-OTDR system for vibration detection [33]. Polarization state of the pulse injected into the sensing fiber is carefully adjusted to maximize Rayleigh scattering, and a polarizer is placed before the photodiode to produce polarization dependent signal strength. When there is disturbance from vibration, the polarization state of the backscattered light will be affected so that the position of the vibration could be addressed, thus an event of vibration can be detected.

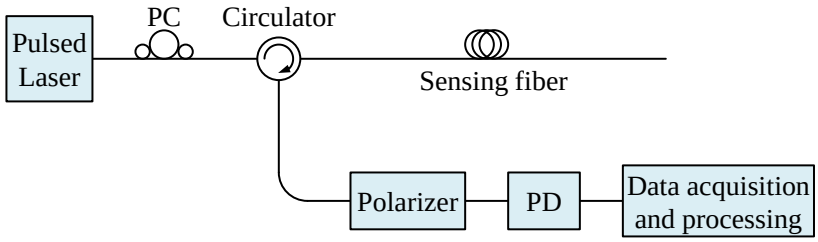

Figure 1-3 Vibration sensing system using polarization-OTDR. (PD: photodetector, PC: polarization controller) [33]

Another technique, similar to the polarization-OTDR introduced above, detects the phase variation from disturbance instead of polarization to identify vibration [34], and the system is shown in Figure 1-4. A CW laser with frequency f is divided into two parts by an optical coupler; one of them, expressed as $E_{LO}(t)exp\ (j2\Delta ft)$, goes directly to one arm of a second coupler while the other is modulated by an acousto-optic modulator (AOM) at frequency Δf. After being amplified by an erbium-doped fiber amplifier (EDFA) and filtered by a band pass filter, the modulated light enters into the sensing fiber via an optical circulator. The light from Rayleigh scattering, expressed by $E_b(t)exp(j2\pi(f+\Delta ft)+\varphi(t))$, exits the circulator and goes to the other arm of the second coupler. The two

light beams with frequency difference of Δf will mix and produce a signal $I(t)$ expressed as:

$$I(t) \propto E_{LO}{}^2(t) + E_b{}^2(t) + 2E_{LO}(t)E_b(t)\cos(\theta t)\cos(2\pi\Delta f t + \varphi(t)) \qquad (1.2)$$

where $\theta(t)$ is the relative polarization angle and $\varphi(t)$ is the phase shift between the Rayleigh scattered light and the local light.

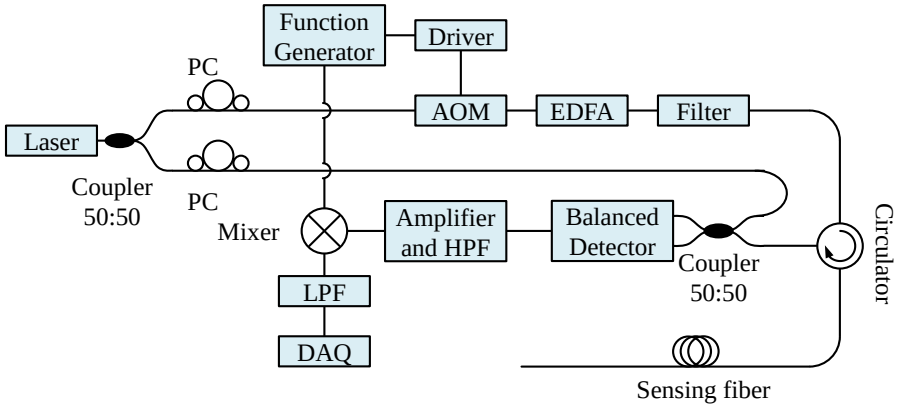

Figure 1-4 Vibration sensing system based on phase-OTDR [34]

The AC component contains the information of the position in the phase term $\varphi(t)$. Using a balanced detector, the DC component can be eliminated. The detected AC signal is then mixed with a local signal with frequency of Δf and finally the phase term could be extracted using a low pass filter. Vibration causes phase change in the backscatter signal and this phase change will be reflected in the signal level after the low pass filter. Similar to the polarization-OTDR, continuously monitoring the power level of a certain position could yield information about the vibration.

Both the polarization-OTDR and phase-OTDR method can identify the event of vibration at any point along the fiber, but same as the traditional OTDR, their spatial resolution is limited by the pulse width so it is generally in the order of meters. The signal from Rayleigh backscattering is also weak so data averaging is required for a better SNR and the data averaging compromises the sensing speed. To improve the signal quality, a fiber Bragg grating (FBG) assisted polarization-OTDR method was developed and it has ability of increasing the signal quality because the returned signals by FBGs are stronger than the signals from Rayleigh backscattering [45].

1.1.3 Optical frequency domain reflectometry

Like the OTDR, optical frequency domain reflectometry (OFDR) also uses backscattered light to perform fully distributed sensing. The difference is that the original signal received is in frequency domain, and the position of an event is determined by the Fourier transform. OFDR systems using different backscattered signals have been developed [29, 30, 36-39]. This technique can measure both strain and temperature.

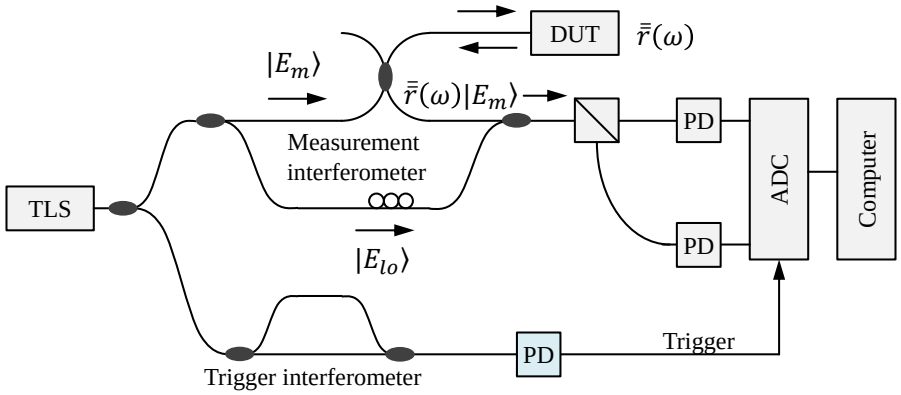

Figure 1-5 Distributed sensing with Rayleigh-OFDR [38] (ADC: analog-to-digital converter)

Figure 1-5 shows a system using Rayleigh backscattering for component characterization based on OFDR [38], and a similar system can also be used to measure temperature or strain [39]. The output of a tunable laser is split into two parts by an optical coupler. The first part passes a Mach-Zehnder interferometer (MZI) and works as a trigger for a data acquisition card. The other part of the light is again split into two beams by a second coupler. One of the light beams goes to the sensing fiber via a circulator and generates backscattered light which is collected by a third coupler. The other light beam directly goes to the third coupler as a local reference. The two signals will mix at the output of the third coupler. A polarization beam splitter (PBS) is used before photodiodes to minimize signal fading due to polarization misalignment of the interfering measurement and local oscillator [38]. Since the frequency of the laser is being tuned during measurement, the frequency difference between the backscattered light and the local oscillator is determined by the position where the scattering occurs. Each scattered light will beat with the local oscillator and produce an interference pattern with the frequency difference, and

the received signal is the superposition of all the interference patterns. By performing Fourier transform, signals from different positions can be discriminated from each other.

Theoretically speaking, the OFDR can provide fully distributed sensing [46], but in practical cases, due to discrete frequency sampling, the measurement results are from discrete positions. For the scheme in Figure.5, the spatial resolution and maximum sensing range are given by [46]:

$$L_{max} = \frac{c\tau}{cn_g} \tag{1.3}$$

$$\Delta L \approx \frac{c}{2n_g \Delta f} \tag{1.4}$$

where c is speed of light in vacuum, τ_g is the differential delay of the MZM, n_g is group index of the sensing fiber and Δf is the maximum frequency tuning range. So the sensing range and spatial resolution are both highly dependent on the tunable laser. The OFDR method can provide a spatial resolution in the order of micrometers but the sensing range is generally limited to a few kilometers. Also the sensing speed is usually on the order of Hertz.

Comparing the three methods discussed in this section, the OFDR offers the highest spatial resolution but the sensing range is limited, and it requires tunable laser with narrow linewidth which could be expensive. Both OTDR and BOTDA can be used for long range sensing, but spatial resolution is on the order of meters. Using special configuration or data processing method, the spatial resolution of the BOTDA can be improved to millimeters. The BOTDA requires frequency tuning and data averaging so the sensing speed is limited to the order of hertz for a long sensing range, and the OTDR requires even larger number of average so the sensing speed is lower, requiring time of minutes to complete one measurement.

There are other techniques for distributed sensing, for example, strain sensing based on Kerr effect induced polarization rotation [31], vibration sensing using Mach-Zehnder interferometer [13], oxygen sensing based on fluorescent emission from cladding and

biochemical sensing using T-LPG [19]. Each of these has some drawbacks, such as requiring high power, system complexity, the use of a specially fabricated fiber or limited sensing range, and therefore are less popular in comparison with the methods introduced in this section.

1.2 Quasi distributed fiber sensing

Quasi distributed fiber sensing is usually achieved by using multiple sensing elements in one or more fibers. These sensing elements are located at different positions so information about measurement parameters of interest at these locations can be obtained. Fiber Bragg grating is perhaps the most commonly used sensing element in quasi-distributed sensing for its compact size, mass production capability and sensitivity to both temperature and strain. A Fabry-Perot (FP) interferometer is another option for temperature, strain and pressure measurement [10, 47, 48], and it can also be multiplexed to provide quasi-distributed sensing.

1.2.1 Multiplexed Fabry-Perot sensors

Figure 1-6 shows a quasi-distributed sensing system based on multiplexed intrinsic Fabry-Perot interferometer (IFPI) sensors [49]. IFPI sensors fabricated by the use of a femtosecond laser are located at different positions along the fiber and each of them has different optical path differences (OPDs). A spectrum interrogator scans the light wavelength and obtains the reflection spectrum of the entire sensing link. Since the sensors have different OPDs, they will be represented by different frequency peaks in the spatial frequency domain after Fourier transform, thus they can be discriminated from each other. These OPDs could be calculated from the spatial frequencies and variations in temperature or strain can be obtained because each OPD is temperature and strain dependent.

One advantage of multiplying multiple distinctive Fabry Perot interferometers is that the system is simple, and the theory involved in the signal demodulation is straightforward. However, because this technology requires distinctive OPDs for all the sensing elements,

the capacity of multiplexing is determined by the wavelength range and resolution of the spectrum measurement.

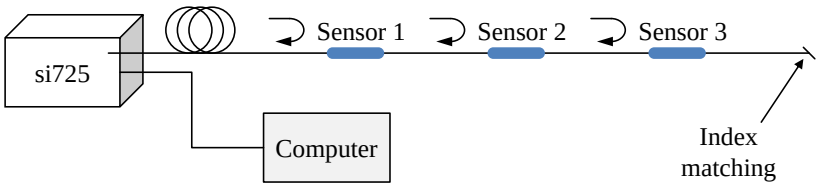

Figure 1-6 FP based quasi distributed sensing [49] (Si725: optical sensing analyzer by Micron Optics)

Another method, which uses multiple identical FP sensors formed by pairs of FBGs [12], does not require spectrum analysis so the number of sensing elements is not limited by the wavelength range and resolution of the spectrum measurement. However, this technology can only correctly capture a dynamic event in the sensing fiber if it is the only high speed event, and this limits this technology's application.

1.2.2 Multiplexed FBG sensors

The reflection spectral peak of an FBG is sensitive to strain and temperature so FBGs are widely used in distributed strain or temperature sensing. Since the reflection peak wavelength is the information of interest, various methods have been developed to measure the reflection spectra of multiplexed FBGs in a sensing link. Two major FBG interrogating techniques are time division multiplexing (TDM) and wavelength division multiplexing (WDM), and examples of them will be introduced in this section.

1.2.2.1 Time-division multiplexing

The TDM method has been intensively investigated for its straightforward concept and configuration [50-52]. Figure 1-7 illustrates a TDM-based quasi-distributed FBG sensing system. The sensing link is formed by serial ultra-weak FBGs (UW-FBGs) with almost identical reflection wavelengths. The output of a tunable laser is modulated by an EOM, which is driven by a pulsed electrical signal, and then gets amplified by an EDFA for higher power.

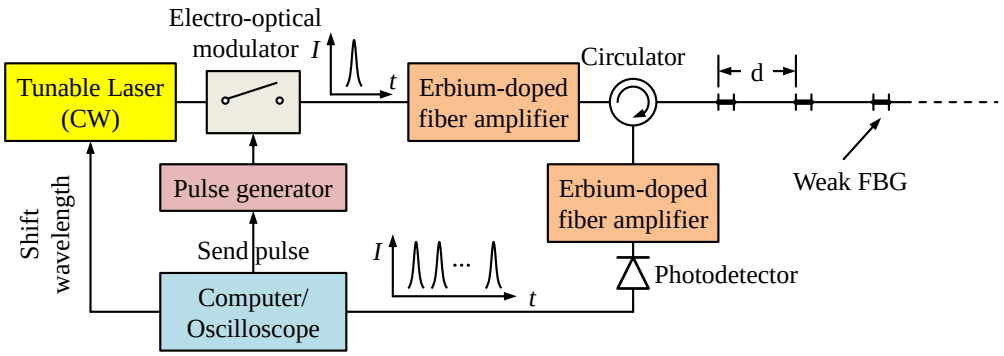

Figure 1-7 FBG based quasi distributed sensing using TDM [52]

The amplified optical pulse enters the sensing link via a circulator and gets reflected by the FBGs, and the consecutive reflections form a pulse train. The reflected pulses are then amplified by another EDFA and detected by a photodetector. Amplitude of each pulse is dependent on the reflection spectrum of the FBG and the wavelength of the source. By scanning the wavelength and tracking the amplitude of the pulse from each FBG, the reflection spectra of the FBGs can be obtained and temperature or strain variation can be monitored.

Another TDM method uses a broadband pulsed source to avoid wavelength scanning, as Figure 1-8 (a) shows [51]. Since the input pulse has a broadband spectrum, every FBG in the sensing link can reflect part of the input power so a pulse train is produced. At the output of the sensing link, a pulse selection structure, illustrated in Figure 1-8 (b), is used to locate only one pulse from a certain FBG and the peak wavelength of this FBG can be determined by measuring the spectrum of the pulse. By changing the delay of the pulse selection signal, all the FBGs can be measured.

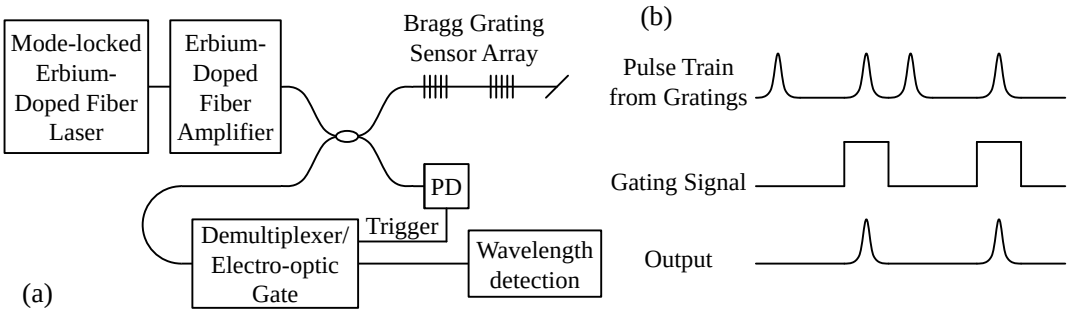

Figure 1-8 FBG based quasi distributed sensing using TDM and pulse selection [51]

C. Hu et al proposed another method which uses a tunable laser instead of a broadband source to measure the spectrum of FBGs [53]. A semiconductor optical amplifier (SOA), which is driven by an electrical pulse delayed with respect to the injected light pulse, is used to locate the reflected pulse from a certain FBG. Any pulse can be selected by the control of the pulse delay so all the FBGs can be measured.

The sensing speed is limited in the two methods mentioned above for different reasons. For the broadband light source based scheme, the time required for wavelength scanning is saved, but the speed can still not be high because the spectrum of only one FBG can be measured each time. To obtain the information from the entire sensing link, FBGs have to be sequentially measured one after another, so the time required increases linearly with the number of FBGs. For the method in [52], additional time is needed for the wavelength scanning so the sensing speed is further limited.

1.2.2.2 Wavelength-division multiplexing

WDM is another method to measure the reflection spectra of multiplexed FBGs [54, 55]. The idea of WDM is to use FBGs with different peak wavelengths and track each reflection peak in the entire reflection spectrum. In this case CW light would be sufficient. To have an adequate dynamic range, wavelength multiplexing should be sparse, which restricts the number of the sensing elements.

Figure 1-9 (a) illustrates a WDM based FBG interrogation system potentially for fast response [54]. It uses a broadband light source and an arrayed waveguide grating (AWG) to interrogate the FBGs and to demultiplex the signals from the FBGs. As Figure 1-9 (b) shows, the FBGs are specially designed to make sure that each reflection peak is located at approximately the center of a pair of neighboring channels of the AWG, and the outputs of the two channels are detected by two separate photodetectors. The power ratio of the two outputs will give a relative position of the reflection peak with respect to the channel position in the wavelength domain. As the peak wavelength of an FBG changes due to a temperature or strain variation, the ratio will change accordingly and temperature or strain sensing could thus be achieved. The number of AWG channels and photodetectors used has to be twice the number of FBGs in the sensing link.

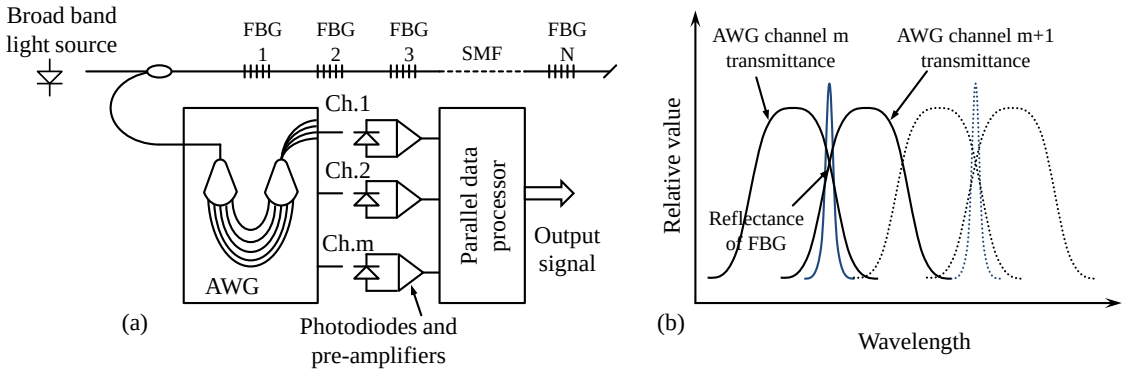

Figure 1-9 FBG based quasi distributed sensing using AWG [54] (SMF: single mode fiber)

One advantage of this WDM method is that all the FBGs can be monitored at the same time, neither wavelength scanning nor pulse selection is required, so the speed can be high. And all the FBGs have different wavelengths, so the power depletion problem associated with some other methods does not exist here. However, this scheme has two major limitations. Firstly, the sensing range is limited because the maximum number of FBGs is given by the separation between adjacent reflection peaks and the wavelength range that the broadband source can cover. Also, the channel number of the AWG is another limitation because it has to be twice the number of the FBGs. Secondly, to achieve high speed sensing, each channel should be detected by one photodetector and the system cost will thus grow with the sensing range. Besides, it requires balancing between the photodetector pairs and temperature control of the AWG to avoid unwanted errors. All of these make the system complex and costly thus not practical for large scale distributed sensing.

Another interesting method uses both the WDM and code division multiple access (CDMA) techniques to make dense WDM possible [56]. Instead of using a CW optical signal, the output of the light source is modulated by a pseudorandom bit sequence (PRBS). When the signal from an FBG is detected, the same PRBS pattern is used as a local signal to mix with the signal reflected by a FBG. By adjusting the delay of the local PRBS signal, the reflected signal from a specific FBG in an FBG array can be extracted. Then by the tuning of light source wavelength, the reflection spectrum of each FBG can be measured. This method eliminates the limitation on the FBG multiplexing capacity in

the previously described WDM method, but still requires one photodiode for each FBG, so it is still costly.

1.2.2.3 Optical frequency domain reflectometry

OFDR could also be used to measure the spectrum of a large number of FBGs multiplexed in one fiber with high density, as it is demonstrated in [57]. More than 3000 FBGs are multiplexed in four fibers, each with 800 gratings densely distributed, 1 cm apart from each other. Firstly the reflection spectrum of the entire sensing link was measured by tuning the wavelength of the light injected into the fiber. With Fourier transform, the FBGs are mapped in the spatial domain and thus distinguished from each other. Figure 1-10 (a) shows an example when the FBGs have spatial interval of 2.54cm, in which each peak comes from one grating in the fiber. By performing inverse Fourier transform, the spectrum of each FBG could be obtained, as Figure 1-10 (b) shows.

This method has the advantage of obtaining spectra of all the FBGs in one round of measurement. However, the nature of interference requires the light source to be coherent, subsequently the sensing range is limited by the coherence length of the tunable laser. Besides, the wavelength tuning needs to be linear and is relatively time consuming if the tuning range and wavelength resolution is to be guaranteed.

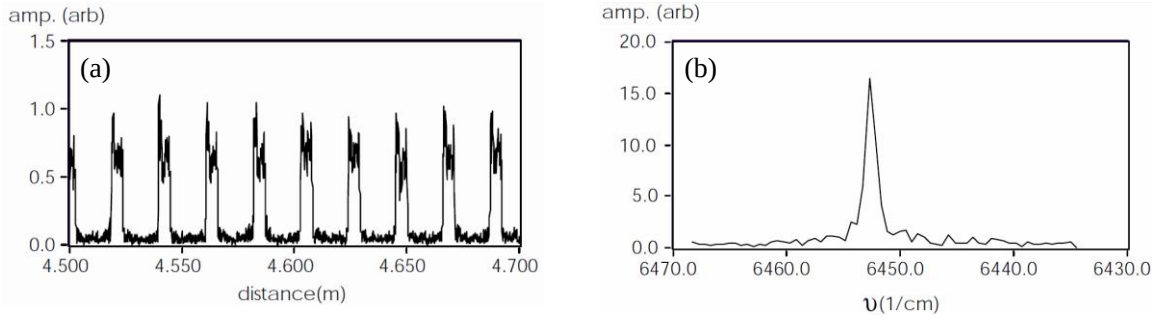

Figure 1-10 OFDR based FBG interrogation (a) Fourier transform of the raw signal. (b) Inverse Fourier transform of one peak in (a) [57]

1.2.2.4 Spectral-temporal conversion based methods

Some other researchers also proposed various methods for multiple FBG interrogation using a broadband light source and a dispersion compensating fiber (DCF) [58-60]. Figure 1-11 shows one sensing system uses broad band amplified spontaneous emission

(ASE) as a light source to interrogate multiple FBGs with distinct wavelengths [58]. The incident CW ASE to the FBGs are reflected by every FBG and the returned light, which is also continuous wave, has multiple wavelengths which are the same as those of the FBGs.

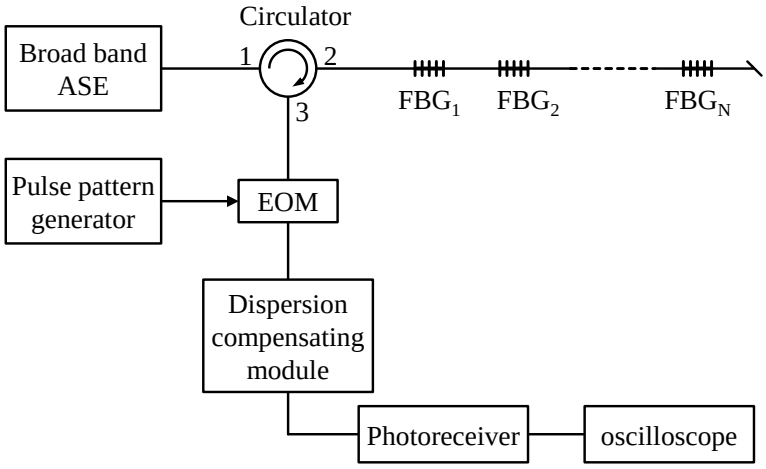

Figure 1-11 FBG based sensing using DCF and pulse modulation [58]

The returned light is modulated by an EOM, which is driven by a pulse pattern generator, and then becomes a multiple-wavelength pulse. When passing through the DCF, the different wavelength components of the pulse will separate in the time domain due to the chromatic dispersion of the DCF. With sufficient dispersion, one multiple-wavelength pulse will split to multiple pulses, each representing one FBG. The time of arrival reflects the reflecting wavelength of the corresponding FBG. Using this method, 2.4MHz detection of three FBGs was achieved.

This is a simple yet effective wavelength-to-time mapping method. However it is not suitable for long range sensing, because to separate the pulses in the time domain, the FBGs have to have different wavelengths. This means the total number of FBGs is limited by the light source. Not to mention that the fabrication of a sensing link with distinct wavelengths is not cost effective.

H. Xia also proposed FBG interrogation techniques using chromatic dispersion, exploiting wavelength-to-time mapping, instead of using continuous ASE, and an femtosecond laser was used as light source [59]. However this method also has the

drawback of limited sensing range due to the requirement of different FBGs in the sensing link.

1.3 Discussion of existing distributed sensing techniques

Quasi distributed sensing techniques, both FP and FBG based, have spatial resolution determined by the spatial interval between two adjacent sensing elements. With the capability of mass production, the cost of a sensing link could be relatively low, even though it requires modifications to the fiber. Comparing with the fully distributed sensing techniques introduced in Section 1.1, they require less complicated signal processing while usually having higher cost for the sensing fiber. Typical spatial resolution for a distributed sensing methods is on the order of meters, which is similar to that of BOTDA and OTDR. Although quasi distributed sensing techniques usually have a lower spatial resolution than OFDR, they offer larger a sensing range.

However, none of the techniques provides high speed sensing, for example, on the order of Kilohertz, and a large sensing range at the same time. Limitations to sensing speed originate from either frequency scanning or data averaging, while the sensing range is either compromised by the coherent length or the bandwidth of the light source. In the next chapters, a quasi-distributed sensing system is proposed and demonstrated. This UW-FBG based system has the ability of achieving a high speed (kHz) and a long sensing distance (km) simultaneously.

Chapter 2 Sensing approach and principle of operation

2.1 Principle of operation

As mentioned in Section 1.2.2, FBG's reflecting spectrum, especially the peak wavelength, reflects the temperature and strain of the environment. So most of the FBG based sensing methods measure the spectrum of the grating by either light wavelength scanning or by the use of a broadband light source and an optical spectrum analyzer. These methods determine the peak wavelength of each FBG and relates it to temperature or strain. However, as it has already been pointed out, the operation of obtaining the spectrum is time consuming so the speed of measurement is essentially limited.

Chromatic dispersion in some optical devices provides a solution for converting information in the spectrum domain to the dime domain. Due to the existence of chromatic dispersion, the speed of light in the medium is wavelength dependent. For sufficient dispersion, light components with different wavelengths will separate in time as they travel through the dispersive medium, thus a spectral-temporal conversion is achieved. The spectral-temporal conversion is in analogy to the dispersive Fourier transformation and has been widely used in various areas such as spectroscopy, fast laser scanning and photonic assisted analog-to-digital conversion [61]. In our approach, this effect is exploited to demodulate the variations in FBG spectra.

The main idea of the proposed approach is to interrogate a large number of nearly identical UW-FBGs using a broadband pulsed laser and to translate the temperature/strain dependent wavelength of each FBG to time-delay of pulses, as illustrated in Figure 2-1. Fiber sensing schemes have been proposed and demonstrated using FBGs and dispersive components [58-60]; however, they either require distinct FBGs to separate the sensing elements from each other in the spectrum domain, or exploit interference of light, which results in more complicated signal demodulation.

As Figure 2-1 shows, the sensing system consists of four parts: a broadband pulsed light source, a sensing link which consists of a large number of UW-FBGs, a dispersive unit

and a signal detection and demodulation subsystem. Each of these parts will be discussed in detail in the following subsections.

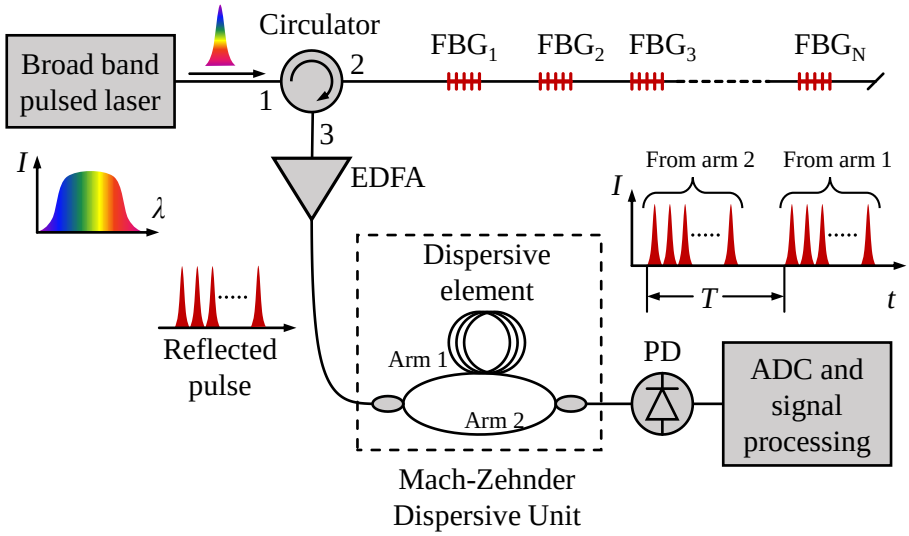

Figure 2-1 Quasi-distributed sensing system based on UW-FBG and chromatic dispersion

2.1.1 Light source

The light source is designed such that it has a relatively broadband spectrum and a pulsed output to accommodate the sensing link.

The UW-FBGs in the sensing link are identical at idle state, but the reflecting wavelengths of the gratings change when the measurand, such as temperature and strain, changes, and this is in fact the basis of the sensing. So the FBGs will have different wavelengths. Besides, there will be nonuniformity in the FBG fabrication process so the gratings cannot be exactly identical. For these two reasons, it is expected that the reflecting wavelengths of the FBGs cover a portion of the optical spectrum. Since the signal is the reflected light from the gratings, the spectrum of the incident light needs to be broad enough to cover all possible wavelengths of the gratings to make sure all the FBGs are detected, as Figure 2-2 shows. The maximum and minimum wavelengths of the gratings in the sensing link are well in the range of the spectrum of the incident source so all the gratings will generate corresponding reflections as needed for signal demodulation.

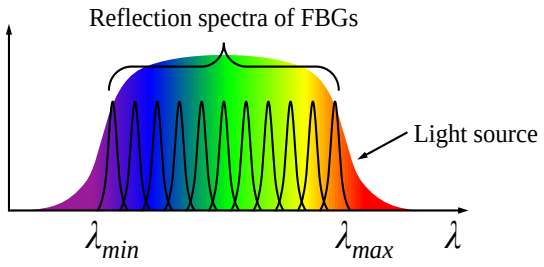

Figure 2-2 Illustration of the spectrum of light source and the reflection spectra of the FBGs

If continuous optical wave is injected into the sensing link, the reflected light from different FBGs cannot be distinguished from each other because they will overlap in time. These reflections may also overlap in the wavelength domain because the FBGs are designed to be identical. The pulsed output from the light source ensures that all the returned light form the gratings in the sensing link is separated in the time domain. They can thus be demodulated separately, so this is a typical TDM system.

When such a light source is launched into the sensing link, every grating in the sensing link can reflect a portion of the injected pulse and the reflected pulse from a certain FBG will have the same wavelength as this grating. These pulses will be sufficient for demodulating the wavelengths so all the FBGs are interrogated in one measurement without wavelength scanning or delayed gating.

The pulse width of the light is dictated by factors such as the sensing spatial resolution, the data sampling rate after the detection and the desired sensing resolution. Its influence on the spatial resolution and the performance of the system will be analyzed in the upcoming sections and chapters.

The light source could be realized by externally modulating a broadband continuous source. The broadband light source could be a superluminescent diode (SLD), an EDFA. The light source could also be a supercontinuum laser which is commercially available but not cost effective.

2.1.2 Sensing link

2.1.2.1 Fiber Bragg grating

Fiber Bragg grating is a section of fiber with periodic refractive index variation along the longitudinal axis. The period of the grating is named pitch, which is either constant or varying along the fiber. If the incident light is at the wavelength where the reflected light along the grating forms constructive interference, the FBG will effectively reflect the incident light. Otherwise, the light can pass through it with negligible loss, as Figure 2-3 shows. Ideally the transmission and reflection spectra are complementary.

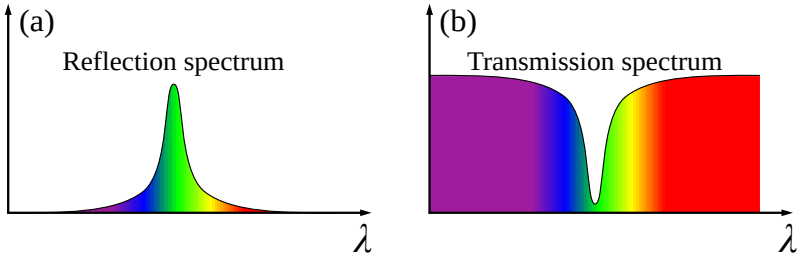

Figure 2-3 Spectrum of FBG (a) Reflection spectrum (b) Transmission spectrum

For an FBG with pitch of Λ and the group index n of the fiber, the reflecting wavelength λ_{FBG} is given by:

$$\lambda_{FBG} = 2n\Lambda \tag{2.1}$$

Due to the thermo-optic effect and the photo-elastic effect, the refractive index and the pitch are both dependent on temperature or strain applied to the fiber. The reflecting wavelength can therefore be used as a measure of the temperature or the strain so an FBG could be used as a sensor.

2.1.2.2 FBG multiplexing

The sensing link is a fiber cable with a large number of UW-FBGs inscribed on it. The interspace between two neighboring UW-FBGs determines the spatial resolution of the

sensing system. Same as traditional FBGs, the UW-FBGs can response to variation of temperature or strain by wavelength shift of the reflection spectrum.

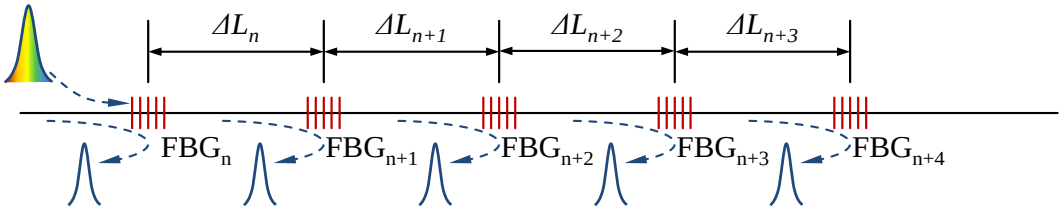

Figure 2-4 Reflection of the injected pulse by each FBG in the sensing link

As Figure 2-1 shows, the pulsed broadband light is launched into the sensing link via a circulator. As mentioned in Section 2.1.1, the spectrum range of the injected pulse is broad enough to cover the reflecting peaks of all the FBGs so each FBG will reflect part of the input light, forming a pulse train, as Figure 2-4 shows. Since the FBGs are spatially separated, pulses reflected by the gratings are separated in the time domain with time interval determined by the spacing between the gratings. The positions of the gratings can be determined by the arrival times of the pulses at the detectors. It should be pointed out that the spacing between the adjacent FBGs is not required to be uniform. The criterion for the minimum spacing between the FBGs is that no overlap should occur between pulses from two adjacent FBGs. However, there is a minimum spacing determined by the pulse width and the maximum possible change of wavelength.

In order to maximize the utilization of the bandwidth of the light source, identical UW-FBGs are preferred. In fact, the requirement of identical FBGs simplifies the process of FBG fabrication. As it has been demonstrated, identical gratings can be written during the fiber drawing [62], so the cost of such a sensing link can be significantly reduced comparing with a fiber consisting FBGs with distinct wavelengths.

2.1.3 Dispersive unit

The reflected pulses will exit the circulator from port 3 and then reach the dispersive unit, which has two designs as shown in Figure 2-5.

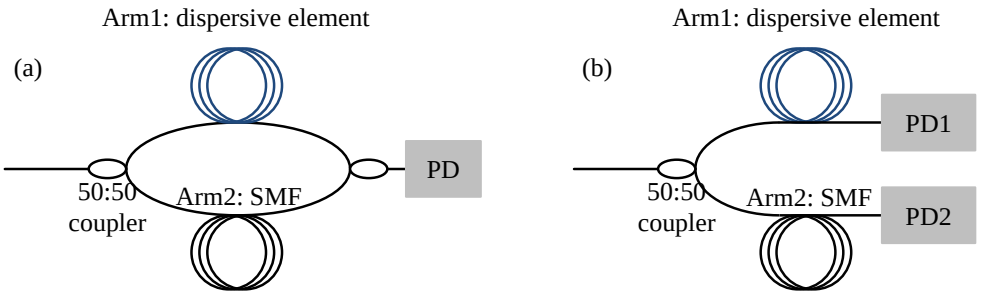

Figure 2-5 Two designs of the dispersive unit (a) Mach-Zehnder structure with one photodetector. (b) Branch structure with two photodetectors.

2.1.3.1 Mach-Zehnder structured dispersive unit

For the Mach-Zehnder structured dispersive unit in Figure 2-5(a), the reflected pulses are split by one fiber coupler into the two arms of the structure and then are recombined by another 1×2 fiber coupler, forming a longer pulse train with two groups of pulses, as Figure 2-6 shows.

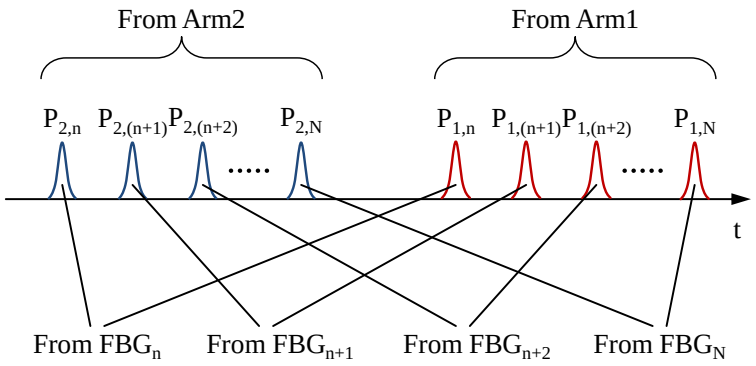

Figure 2-6 Pulses detected by the PD at the output of the Mach-Zehnder structured dispersive unit

The lengths of the two arms are designed that pulses from Arm1 do not overlap with the pulses from Arm2, that is, the optical path difference between the two arms should introduce a delay that is equal or larger than the duration of each of the groups. It could be arranged that the pulses from one arm reach the photodetector before or after the other group, although in the figure only the case that pulses from Arm1 arrives later is illustrated. Minimizing the duration of the signal in each measurement can increase the maximum possible sensing speed, so it is preferred that the lengths of the two arms to be adjusted that the two groups of pulses have minimum possible time gap between them.

In Figure 2-6, $P_{m,n}$ demotes the pulse reflected by the *n*-th FBG and arriving at the detector via Arm *m*, in which m is either 1 or 2. Assuming the number of the FBGs in the sensing link is *N*, each pulse group will have *N* pulses from the FBGs. These *2N* pulses form *N* pairs, and in each of the pairs, both of the pulses are originated from the same FBG but pass through the dispersive unit via the different arms.

For the *n*-th pulse pair, the delay between the two pulses, which is denoted as τ_n, is needed to deduce the wavelength information because its variation reflects the wavelength's change. Assuming $t_{1,n}$ and $t_{2,n}$ are arrival times of pulses from Arm1 and Arm2, respectively, the pulse delay τ is given by:

$$\tau_n = t_{1,n} - t_{2,n} \tag{2.2}$$

2.1.3.2 Branch-structured dispersive unit

The design in Figure 2-1(b) is a modified version from the one in Figure 2-5(a) by removing the optical fiber coupler which combines the light from the two arms, and by using two photodiodes instead of one. After entering the dispersive unit, the returned light is split into two arms, in which Arm1 has the dispersive element in it, while the other arm has a length of regular single mode fiber. The two groups of pulses are detected directly by the two photodetectors without beam recombination.

In this design, the lengths of the two arms are designed so that the pulses from the same FBG reach the two photodetectors at almost the same time, as Figure 2-7 illustrates. This helps simplify the process of pairing the pulses from the same FBG, and will finally be beneficial in the signal processing. Synchronization of the two groups of pulses is achievable by the control of the length of the SMF in Arm2, which is cost effective and easy to implement.

As Figure 2-7 illustrates, when the synchronization is achieved, the two groups of pulses are detected and paired. The delay is defined the same as that described in 2.1.3.1.

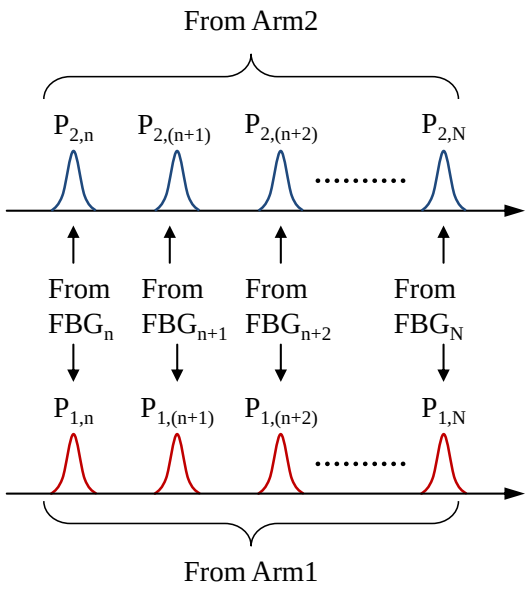

Figure 2-7 Pulses detected by the PDs at the outputs of the branch-structured dispersive unit

Comparing with the Mach-Zehnder structured design, with the expense of one more photodetector, this modified design gains the advantage of higher sensing speed for the same sensing range, simpler data processing process and better usage of optical power. The sensing speed will be discussed in Section 2.2.

The branch-structured dispersive unit simplifies the data processing because the pulses can be paired only by the time of arrival and there is no need to search back in time to find the other pulse, which arrives much earlier. This is a significant improvement when the sensing range is large, which generates large amount of data and making data searching more time consuming.

The Mach-Zehnder structured dispersive unit drops off half of the received power when combing the light from the two arms, but all the power is used in this modified branch-structured design. This is an advantage because power is proved to be important to the system SNR, which is a key factor to the system's performance, as it will be discussed in Section 2.5.1.

2.1.3.3 Wavelength-to-delay conversion

When the temperature or the strain of the FBG changes, the reflected pulse will have a wavelengths shift. Because of the existence of the dispersive element, the speed of light in the two arms, mainly in Arm1 which has the dispersive element, of the dispersive unit will vary, thus the delay between the pulses from this FBG will be dependent on the wavelength of pulse. The change of the delay, denoted as $\Delta\tau_n$, reflects the variation of the wavelength, $\Delta\lambda_n$, of the FBG. The relation between $\Delta\tau_n$ and $\Delta\lambda_n$ is given by:

$$\Delta\tau_n = D \cdot L \cdot \Delta\lambda_n \tag{2.3}$$

where D is the dispersion of the dispersive element in [ps/nm/km] and L is the length of the dispersive element. By monitoring the change of delay, variation of the wavelength can be calculated, thus the change of temperature or strain of this FBG can be obtained. This delay calculation can be applied to all the FBGs in the sensing link, so distributed measurement can be achieved. This case is illustrated in Figure 2-8(a) and (b), in which solid lines are the detected signal from Arm1 and the dashed lines are the signals from Arm2. $\Delta\tau_n$ is given by τ_n-τ_n' in the figure, of which τ_n and τ_n' are the delays between the two pulse originated from the same FBG but from different measurements.

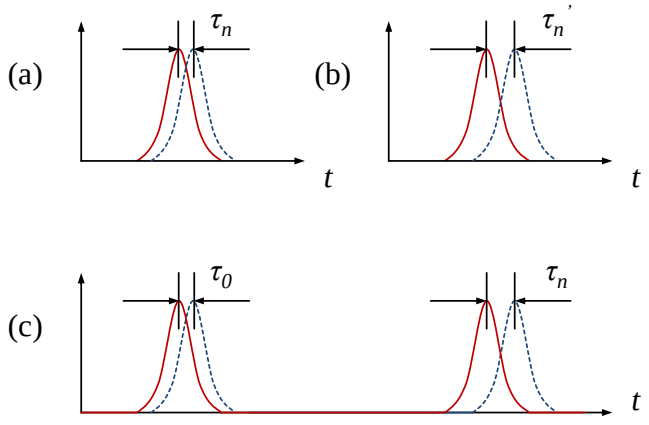

Figure 2-8 Two cases of the measurement. (a) and (b) show traces of two measurements of one FBG. Solid lines are detected signal from Arm1 and dashed lines are signals from Arm2. (c) Shows signals from two FBGs in one measurement. Solid line is from Arm1 and dashed line is from Arm2.

This method can also be used to measure the wavelength distribution of the FBGs in the sensing link, as Figure 2-8(c) illustrates. In this case, signal from one measurement is considered, only the comparison of delay is performed between different FBGs. In Figure 2-8(c), when two FBGs with different wavelengths are measured, the delay of the pulse pairs will be different. If delays are defined as τ_0 and τ_n, $\Delta\tau_n$, which is given by τ_n-τ_0, can also be used to calculate the wavelength difference between the two FBGs. This measurement can be extended to the entire sensing link so the wavelengths of all the FBGs can be obtained. Knowing this, a calibrated FBG in the sensing link which is kept in a stable environment can act as a reference to the system, helping obtain absolute wavelength of every FBG in the system. In this case, the definition of $\Delta\tau_n$ in Equation 2.3 is not the delay change of the *n*-th FBG's pulse pair, rather the delay difference between the data pairs of the *n*-th FBG and the reference FBG.

2.1.3.4 Dispersive elements

There are various choices for the dispersive element, which may be either non-fiber structured or fiber structured. In our system, because the system is mostly fiber based, a fiber based dispersive element is the preferred choice because it is more compatible with other devices in the system.

Regular single mode fibers usually have small positive dispersion at 1550nm because of the characteristics of the material and the waveguide effect. For Corning SMF28, which is a commonly used fiber in optical communications and other applications, the dispersion is about 18ps/nm/km at 1550nm. With a sufficient fiber length, the total dispersion can be enough to generate wavelength dependent time delay as needed in the proposed sensing scheme. However, regular fibers can only be used in the dispersive unit with the Mach-Zehnder structure because this structure allows a large optical path balance between the two arms. In contrast, the branch-structured dispersive unit requires the two arms to have approximately the same length to make sure the two pulse sequences arrive at the two photodetectors nearly at the same time. If a regular fiber is used as the dispersive element, then both of the arms have the same type of fiber and length, thus the net dispersion, which is the dispersion difference between the two arms,

is around zero for the dispersive unit, and there will be no wavelength dependent delay between two pulses from the two arms.

A preferable option is a fiber with significantly larger dispersion than the regular single mode fiber. This will reduce the footprint of the dispersive element and allow the use of a regular single mode fiber in Arm 2 to adjust length difference between the two arms. Such a design is suitable for both the Mach-Zehnder structured and the branch-structured dispersive units. DCF, which has large negative dispersive because of its specially designed index profile, is a suitable candidate. Figure 2-9 shows two typical index profiles of DCFs. Comparing with the telecommunication regular single mode fiber, which usually has its core and cladding with different effective refractive indices, DCF fiber often has an extra low-index layer between the core and the cladding [63, 64]. This design provides additional waveguide dispersion so a DCF usually offers a larger dispersion than regular single mode fiber. Typically a DCF has a dispersion around -100ps/nm/km [63].

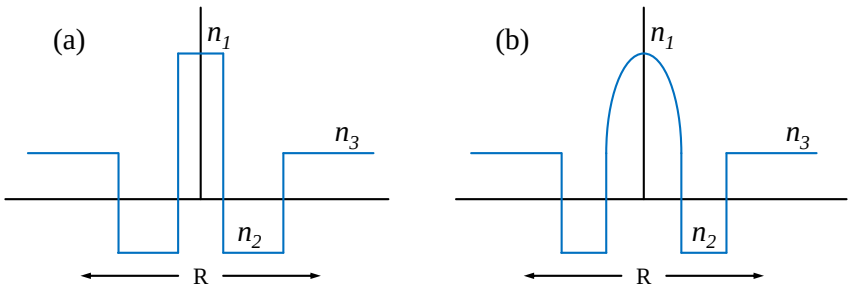

Figure 2-9 Two index profiles of dispersion compensating fibers (a) Step index W-shaped index profile [63] (b) W-shaped central parabolic index profile [64]

Besides DCF, some special designs of photonic crystal fibers (PCFs) could provide negative dispersion even higher than DCF. Figure 2-10 shows the design and simulated dispersion characteristic of the PCF presented in [64]. With this specific design, this fiber can have a dispersion as high as -2,200ps/nm·km at 1550nm [65]. The periodic structure creates allowed bands and forbidden bands in the transmission spectrum of the fiber. As a result, the dispersion characteristics are dramatically different from traditional fibers and large waveguide dispersion can be achieved. Researchers went even further to increase the dispersion to -18,000ps/nm·km with a similar design [66]. With such a high

dispersion, the total length needed for the dispersive element can be significantly reduced so the size of the dispersive unit can be smaller accordingly. The benefit of using a fiber with larger dispersion is not limited to the reduced size, but the increased resistance to the influence of the environment, which will be discussed in detail in Section 3.1.3.

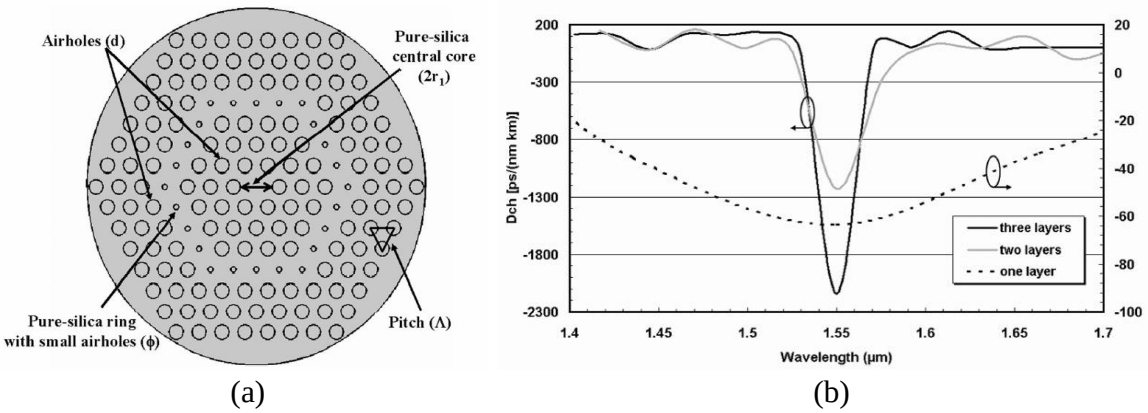

Figure 2-10 PCF based DCF (a) Transverse section of the PCF (b) Simulated dispersion characteristic of the PCF with different number of airhole layers surrounding the center core [65].

Chirped Bragg grating is another option for the dispersive element [67]. A chirped FBG, as Figure 2-11 shows, is a fiber Bragg grating with gradually changing period along the fiber. Since the reflection wavelength is dependent on the period of the grating, the grating's reflecting wavelength changes along the fiber accordingly. Incident light with different wavelength travels for different length along the fiber before being reflected, thus a wavelength dependent delay is introduced. Theoretically speaking, the dispersion can be managed by changing the rate of the period of the grating changes.

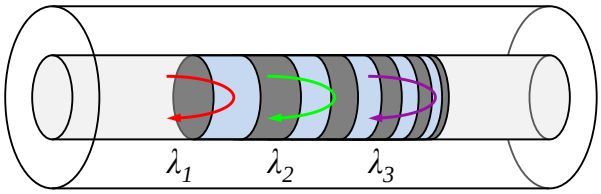

Figure 2-11 Chirped fiber Bragg grating with negative dispersion

One advantage of the chirped FBG is its tunability [68]. Due to the thermal-optic and photo-elastic effects, the refractive index of the optical fiber is dependent on temperature and strain, so the FBG's equivalent period changes according to its temperature or the

strain applied to it. This results in a change in the center reflecting wavelength and thus the dispersion. Based on this feature, temperature or strain can be used to tune the FBG.

Furthermore, if a temperature or strain gradient can be generated to a uniform FBG, a chirped FBG is created. Various methods have been proposed to generate chirped FBG from a uniform FBG [69]. However, with the matured technology of FBG writing, directly writing a chirped FBG to the fiber is more cost effective if there is no special requirement such as controlled existence of the chirp. Besides, the sensitivity to temperature and strain can potentially cause instability if the chirped FBG is not placed in a stable environment.

For the three types of dispersive elements described above, each has its strengths and weaknesses. Regular DCF is the most commonly used device when large dispersion is required in a fiber optical system and it is the most cost effective option. PCF based DCF has higher dispersion and thus it reduces the size of the dispersive unit, but due to the structure difference between the PCF and regular fiber, higher loss is expected at the fiber connection. Also PCF is more expensive comparing with regular DCF. Chirped FBG has the smallest size of the three options, and the best flexibility in terms of tunability of the dispersion. However its fabrication complexity may compromise feasibility of mass-production and result in a higher device cost.

2.1.4 Signal detection and demodulation subsystem

The pulses from the dispersive unit carry the information to be demodulated, which is the delay between the two pulses reflected from the same FBG. To obtain the delay information, three consecutive steps are needed: signal detection, analog-to-digital conversion and delay calculation. Figure 2-12 illustrates the two configurations for the two designs of the dispersive unit. For the Mach-Zehnder structured dispersive unit, only one photodetector is needed. For the dispersive unit based on the branch structure, two photodetectors are employed and consequently two ADCs are required.

The signal detection part converts light signal to electrical signal using photodetectors. Since the FBGs in the system are ultra-weak, the returned pulses are expected to have

low power. For better detection, an EDFA can be added before the dispersive unit to increase the power to the photodetectors. Also because the reflected pulses are from a large number of gratings and are expected to have a relatively large wavelength range, narrow band filters cannot be added after the EDFA to reduce the ASE noise. At the same time, broadband filters will have a limited effect to ASE noise reduction. For this reason, the EDFA is preferred to be a pre-amplifier to minimize the additional noise.

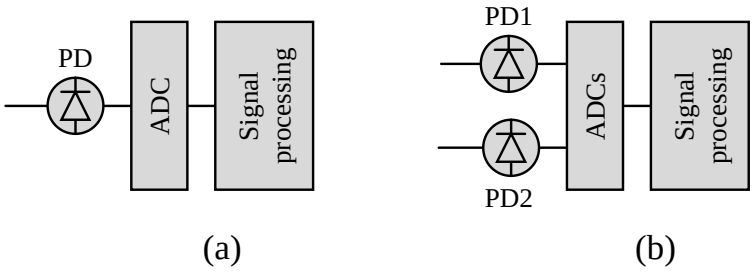

Figure 2-12 Signal detection and demodulation subsystem for (a) Mach-Zehnder structured dispersive unit (b) Branch-structured dispersive unit

The photodetectors can be PIN or APD photodiodes depending on the level of the received power. In addition, electronic amplifiers can be used to boost the signal level before the analog-to-digital conversion. However, the electric noise should also be taken into account to evaluate its influence on the performance of the system. A detailed analysis of the system's noise is presented in Section 4.3.

The detected pulses are sent to ADC(s), which converts the analog signal to digital data points. The sampling rate of the ADC(s) has influence on the system's performance and further analysis is presented in Section 2.5.2.

The digitized signals are then collected by a signal processing system, which can be based on digital signal processors (DSPs) or field programmable gating arrays (FPGAs). The signal demodulation algorithm is designed such that the delay can be calculated in real time.

2.2 Spatial resolution and sensing speed

2.2.1 Spatial resolution

Since it is a quasi-distributed sensing system, the spatial resolution is determined by the spacing between two adjacent sensing elements, which, in our case, are UW-FBGs. It is understandable that there is a minimum spacing between the adjacent FBGs because pulses need to be distinguishable from each other in the time domain. As it is discussed in Section 2.1.1, the pulse width also has influence on the spatial resolution.

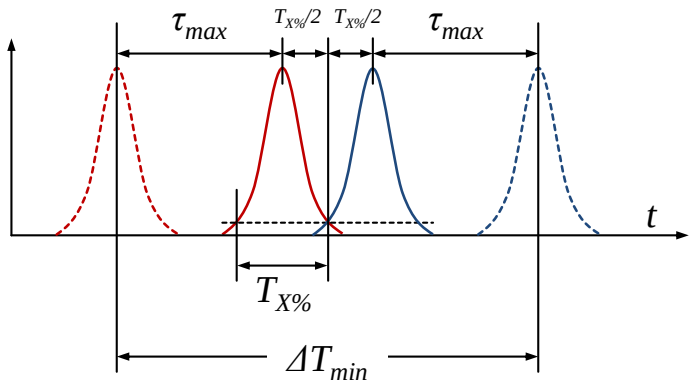

Figure 2-13 Illustration of the case in which maximum and opposite delays are experienced by adjacent Pulses

Figure 2-13 illustrates the condition which determines the minimum spacing between two adjacent FBGs. The red and blue lines illustrate the reflected pulses from two different FBGs. The dashed lines are the pulses when the FBGs are at room temperature and no strain is applied, while the solid lines are the pulse when the two FBGs experience the opposite extreme conditions, which change their wavelengths in such a way that the two pulses move toward each other in time. Assuming ΔL_{min} is the minimum spacing of FBGs in the sensing link, v_g is the group velocity of the light in the fiber, τ_{max} is the maximum delay that can be caused by the extreme condition, and $T_{X\%}$ is the pulse width measured at X% of the peak value, the minimum spacing can be given by:

$$\Delta L_{min} = v_g \left(2\tau_{max} + T_{X\%}\right)/2 \tag{2.4}$$

Assuming that the dispersion of the dispersive unit is -2,500ps/nm, the temperature variation range is ±60°C, the temperature coefficient is 10pm/°C, the group velocity is 2×10^8m/s and X is 10, the relation between the minimum spacing between neighboring FBGs and the pulse width is shown in Figure 2-14. With a pulse width of 2ns, the minimum spatial resolution is about 0.75m.

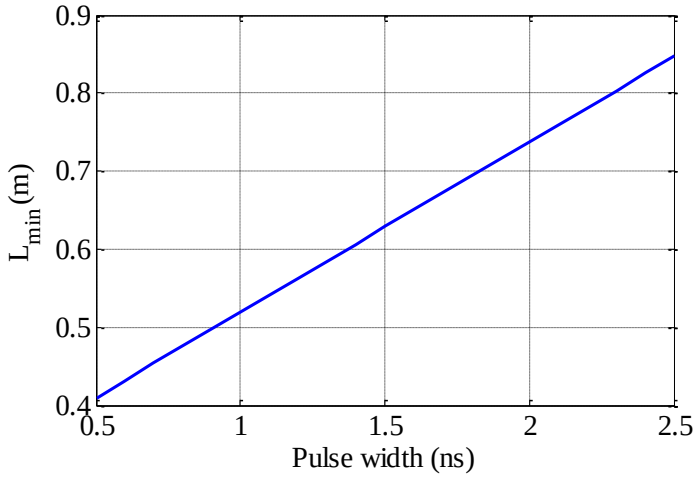

Figure 2-14 The minimum spatial resolution versus the pulse width

2.2.2 Sensing speed

The sensing speed of the system is mainly determined by the sensing range, for the returned pulse train generated by two consecutive input pulses should not overlap with each other in the time domain. The maximum possible sensing speed is different in the two proposed dispersive units.

For the Mach-Zehnder structured dispersive unit, pulses from the two arms are combined before being detected, so the number of pulses detected in each measurement is twice of the number of the gratings. If the FBGs cover fiber length of L_{sensor}, the minimum total duration of the returned signal in each measurement is:

$$T_{signal} = 4L_{sensor} / v_g \qquad (2.5)$$

And subsequently the sensing speed is given by:

$$f_{max}^{MZ} = \frac{v_g}{4L_{sensor}} \tag{2.6}$$

where f_{max}^{MZ} is the maximum sensing speed of the system based on the Mach-Zehnder structured dispersive unit.

This is achieved by adjusting the imbalance between the two arms to be $2L_{sensor}$. In Arm1, the delay introduced by the dispersive unit may be either shorter or longer than the optimum delay, which is $T_{signal}/2$, for the highest sensing speed. But the imbalance can always be adjusted by adding a section of regular single mode fiber to either of the arms. Since regular single mode fiber has much lower dispersion than the dispersive unit, the influence on the effective dispersion of the dispersive unit is not significant.

For the branch-structured dispersive unit, since the pulses from the two arms are sent to two different detectors, the duration of the signal is reduced to half of the value in the previous case, so the sensing speed is doubled:

$$f_{max}^{BR} = \frac{v_g}{2L_{sensor}} \tag{2.7}$$

Here f_{max}^{BR} is the maximum sensing speed for the branch-structured dispersive unit based system.

Figure 2-15 plots the maximum sensing speed versus the sensing range for the two designs of the dispersive unit, by assuming that the group velocity of light is 2×10^8m/s. When the sensing range is 10km, the maximum possible sensing speed is as high as 5kHz. This shows that the high-speed and long-range distributed sensing can be achieved simultaneously. High speed not only enables the ability of detecting high frequency signal, but also provides room for averaging when the required sensing speed is not critical but the performance, such as measurement resolution and accuracy, is more important.

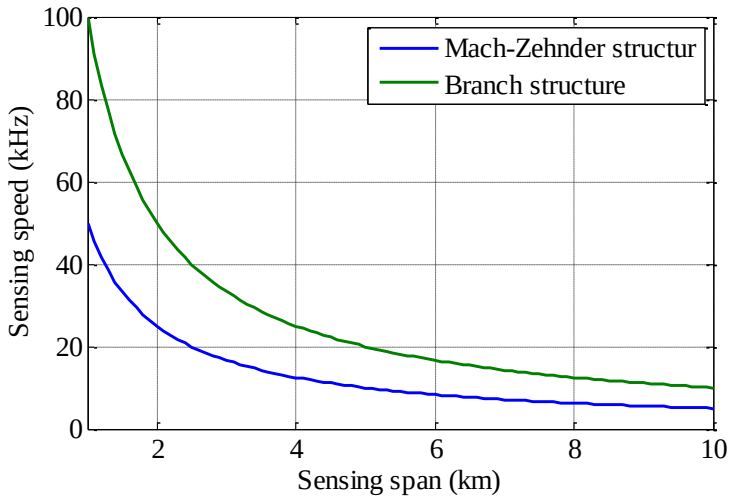

Figure 2-15 Maximum sensing speed versus sensing range of the two designs of the dispersive unit

2.3 Algorithm of signal demodulation

After the pulses are detected and digitized, the delay between the two pulses are then calculated using a cross-correlation algorithm. As it is discussed in Section 2.1.3.3, the delay, τ, is related to the wavelength of the reflected pulse.

The two pulses are firstly extracted from the acquired data using two N-point long windows. Denoting P_1 and P_2 as the N-point long data sequences of the pulses from Arm1 and Arm2, the cross-correlation of the two sequences is expressed as:

$$\begin{aligned} C(n) &= \sum_{m=1}^{n} P_1(N-n+m)\cdot P_2(m) \qquad n \le m \\ C(n) &= \sum_{m=1}^{2N-1} P_1(m)\cdot P_2(n-N+m) \qquad n > N \end{aligned} \tag{2.8}$$

where $C(n)$ is the n-th point in the ($2N$-1)-long cross-correlation result.

Since the two pulses are originated from the same injected pulse, they have similar pulse shapes and therefore the cross-correlation curve is symmetric. For this cross-correlation curve, its peak position is related to the relative positon of the pulses in each of the windows. Assuming the index of the peak position of the curve C is I, the delay between the two pulses can be calculated by:

$$\tau = (I - N) \times \Delta t + T_2 - T_1 \qquad (2.9)$$

where τ is the delay, which is defined in Equation 2.2 in Section 2.1.3.1. Δt is the time interval of the sampling in the analog-to-digital conversion. T_1 and the T_2 are the starting times of the two time windows which locate the pulses from Arm1 and Arm2.

Finding the peak positon I in the cross-correlation curve is critical in the delay calculation. Since the sampling rate of the ADC cannot be infinitely high, it is impractical to use small Δt to improve the accuracy of I.

To achieve a higher resolution of I, it is possible to interpolate the raw data to have a smaller sampling interval, then to calculate the cross-correlation and find the peak by searching the maximum point. However, this increases the amount data to be processed and thus results in slower data processing speed, and this may not be as effective as it is hoped to be, especially considering the fact that the received signal is weak and has relatively low SNR.

Another method is to exploit the fact that the correlation curve is symmetric. In this case, if parabolic curve fitting is applied to the data points in a small vicinity of the maximum point, the peak position of the fitted curve can well represent the peak positon of the correlation curve, and this is particularly important when the signals are noisy.

Another advantage of the proposed algorithm is that cross-correlation can tolerate more noise. One can simply find the peaks of the two pulses by searching for the maximum value, and then use the positions to calculate the delay. However, this result is very sensitive to noise and the accuracy of the calculated delay may be significantly compromised when the SNR is low. In comparison, the process of cross-correlation involves data multiplication and summation, which helps average out the noise and produce a much smoother curve. Finding the peak position from this noise-suppressed correlation curve will lead to a higher accuracy.

Simulation is carried out to verify the previous statement. Assuming the input pulse is Gaussian and thus its electric field can be expressed by normalized amplitude *U(z,T)* [41]:

$$U\left(0,T\right)=\exp\left[-\frac{T^2}{2T_0^2}\right] \tag{2.10}$$

where T_0 is related to full width at half maximum (FWHM) τ by relation $T_0=\tau/\left(2\sqrt{\ln 2}\right)$, and the optical power is:

$$I\left(0,T\right)\propto U\left(0,T\right)\cdot U^{*}\left(0,T\right) \tag{2.11}$$

At the output of the dispersive unit, the normalized amplitude of the electric field is [41]:

$$U\left(z,T\right)=\frac{T_0}{\left(T_0^2-i\beta_2 z\right)^{1/2}}\cdot\exp\left[-\frac{T^2}{2\left(T_0^2-i\beta_2 z\right)}\right] \tag{2.12}$$

In Equation 2.12, z is the length of the dispersive element, and β_2 represents the dispersion parameter, which is related to fiber dispersion D by:

$$\beta_2 z=-\frac{\lambda^2}{2\pi c}D\cdot z \tag{2.13}$$

where $D\cdot z$ is the total dispersion given in ps/nm, and it is known for a given dispersive unit. λ is the wavelength of light and c is the speed of light in vacuum. Optical power at the output of the dispersive element can also be expressed in the way similar to Equation 2.12. Knowing parameters of the pulse and dispersive unit, pulses at input and output of the dispersive unit can be calculated, and simlation can be carried out based on this.

For a Gaussian pulse with FWHM of 2ns, assuming it has normally distributed noise, SNR is 7dB and the dispersion of the dispersive unit is -2,500ps/nm, the pulses and the

cross-correlaton curve are ploted in Figure 2-16. Figure 2-16(a) and (b) show the two noisy pulses before the correlation and Figure 2-16(c) is the cross-correlation. The result shows that the pulses quality is significantly improved after the crossc-correlation, and the SNR improvement is certainly beneficial to the delay calculation.

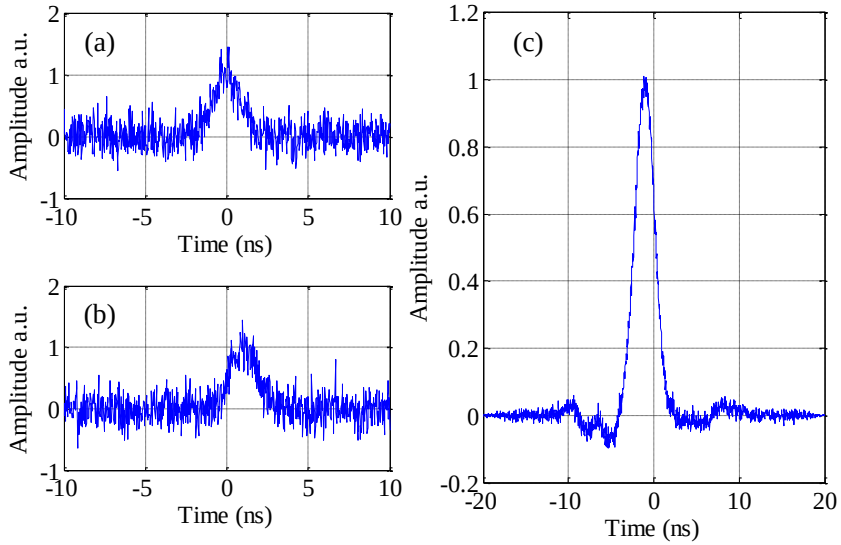

Figure 2-16 Pulses with SNR of 5dB before and after cross-correlation (a) Pulse from Arm1 (b) Pulse from Arm2 (c) The cross-correlation curve

Figure 2-17 shows the cross-corelaton curve and its parabolic curve fitting when the SNR is 7dB. It is obvious that there are small fluctuations in the cross-correlation curve, which will cause uncertainty to maximum point searching results. In comparison, the parabolic fitted curve, which fits quite well with the cross-correlation results, is capable of giving a more accurate peak position.

To evaluate the effectiveness of the cross-correlation and curve fitting method for delay calculation, simulations are carried out to compare the standard deviation (STD) of the delay using four different methods. Method 1 is to directly find the maximum points of each pulse, use them as the peak positions, and then calculate the delay by subtracting one from the other. Method 2 is to perform parabolic curve fitting to the located pulses first, calcuate the peak positons and then subtracing one from the other to get the delay. Mehtod 3 is interpolating the located pulses down to smaller time interal, which in this

case is 1ps, calculating the cross-correlaton, locating its peak by finding the maximum point, and then obtaining the delay using the relation given in in Equation 2.9.

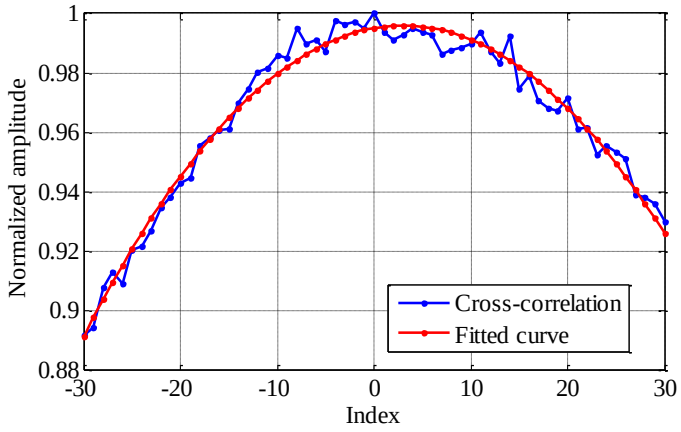

Figure 2-17 cross-correlation curve and its parabolic curve fitting result. Blue: cross-correlation curve, red: parabolic curve fitting

Method 4 is using the algorithm proposed here: performing parabolic curve fitting after cross-correlation. Figure 2-18 plots the dependence of the standard deviation of the calculated delay on the SNR. In the calculation, for each SNR, normally distributed noise is added to the pulses and the delay is calculated 100 times to obtain the standard. Pulses are sampled at 40GS/s.

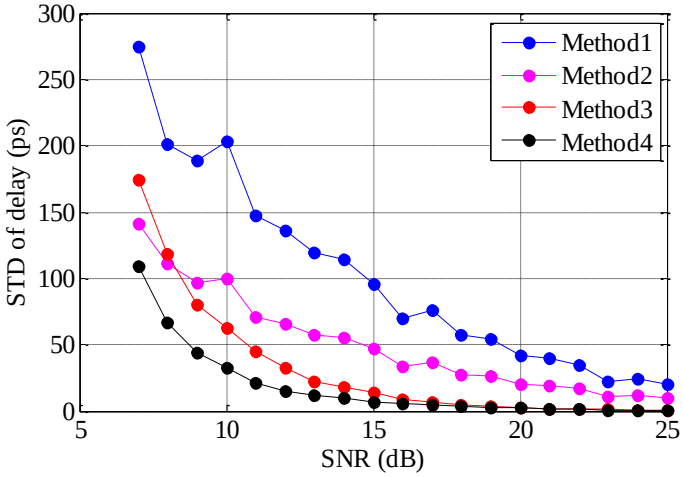

Figure 2-18 Standard deviation of delay calculated using four different methods with different SNR

The simulation results show that the method combining cross-correlation and the parabolic curve fitting provides superior performance over the other three as expected. This is attributed to the noise tolerance of the cross-correlation and parabolic curve fitting.

2.4 Power budget and crosstalk

The requirement of identical FBGs means that the reflected pulses will become weaker as the FBGs are farther from the light source due to the reflections by the previous FBGs [50]. For a given reflectance, there is a limit to the total number of the gratings. If the total number exceeds this limit, the reflected pulses from the far end will become too weak to provide accurate demodulation results. This phenomenon is called power depletion. Also, because the FBGs have the same wavelength, the incident pulse will bounce back and forth between FBGs to cause crosstalk [50, 51]. Besides the power depletion and crosstalk, spectrum shadowing also has an impact on the spectrum of the reflected pulse, which may have influence on the signal demodulation. To maximize the number of FBGs multiplexed in the sensing link and keep crosstalk low, it is necessary to investigate the dependence of power and crosstalk on the number of FBGs and reflectivity.

2.4.1 Power budget

Assuming that all FBGs have the same wavelength and peak reflectivity of R, when incident power on the first FBG is P_0, the reflected power from the n-th FBG will be [53]:

$$P_n = R\left(1-R\right)^{2(n-1)} P_0 \tag{2.14}$$

Figure 2-19 shows the calculated P_n as a function of the number of FBGs and reflectivity. For stronger FBGs, more power is reflected by each FBG thus making the transmitted power, which is the incident power to the rest of the FBGs down the fiber, lower. Lower reflectivity will allow more sensing elements before causing power depletion but it will also result in overall lower signal strength. So the balance between the quantity and the reflectance of the FBGs should be kept to meet the requirement of the sensing span and

the signal quality. For 1,000 FBGs, reflectivity less than -35dB will be able to provide power variation less than 3dB. Considering the power level issue, reflectivity between -35dB and -40dB will be a reasonable choice. If the FBGs have stronger reflectance, for example -30dB, the power is rapidly depleted and the power reflected from the 1,000th FBG is about 8.7dB lower than that form the first FBG. When the reflectance is reduced to -45dB, the 1,000th FBG is only about 1.1dB lower than the power from the first FBG, which is negligible and may be around the level of the reflectance inaccuracy occurred in the FBG fabrication.

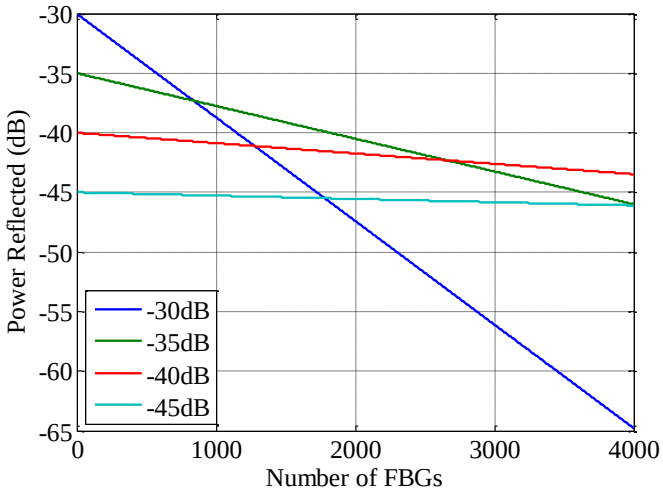

Figure 2-19 Reflected power without fiber loss

The previous discussion did not involve the spacings between FBGs because the loss of the fiber was not taken into account. For traditional FBGs, fiber loss is negligible compared to the reflection of a traditional FBG. However, it is not the case for UW-FBGs. Standard Corning SMF28 has loss of about 0.22dB/km at 1550nm, if the spatial interval of FBGs is 1m, the fiber loss of one round trip is equivalent to that caused by a FBG with reflectivity of -39.94dB, which is similar to the reflectance of a UW-FBG. Assuming 1 m spatial resolution and taking the loss of fiber into account, the power from the *n*-th FBG should be:

$$P_n = \alpha^{2(n-1)} R\left(1-R\right)^{2(n-1)} P_0 \qquad (2.15)$$

where α is calculated from fiber loss A in dB/m by $\alpha = 10^{-A/10}$. For FBGs with -40dB reflectivity each, the results calculated from Equation 2.14 and 2.15 are plotted in Figure 2-20 for comparison. When the fiber loss is considered, reflected power from the 671st FBG will drop to the level of the 1,000th when loss is not taken into account. So for a sensing link consisting of UW-FBGs, the fiber loss is a considerable factor partially limiting the sensing span.

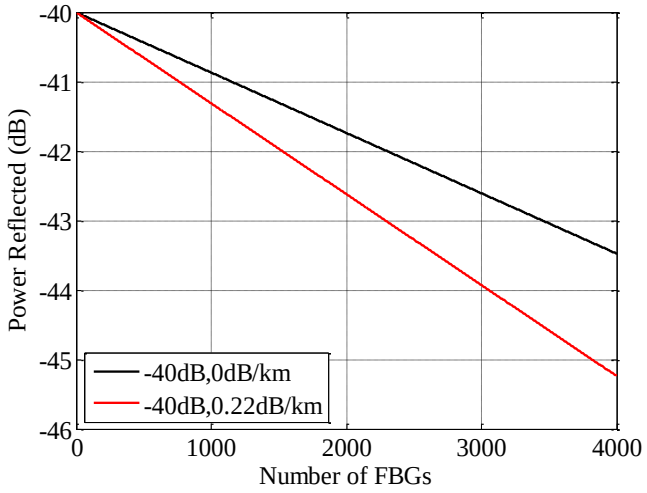

Figure 2-20 Comparison between the reflected power with and without fiber loss at1m spacing

2.4.2 Crosstalk

Crosstalk is another factor which limits the number of FBGs in the sensing link. The crosstalk is caused by the light that is reflected multiple times by more than one FBG and arrives at the same time at the detector as the primary reflection from an FBG. Since the gratings are ultra-weak, higher order crosstalk, which is attributed to the light from more than two additional reflections, can be neglected. The mechanism of the first order crosstalk generation is illustrated in Figure 2-21.

When the FBGs are evenly distributed along the sensing link, pulses reflected from another FBG can be reflected two more times and reach the photodetector and overlap with the pulse reflected by the target FBG. The expression for the first order crosstalk is [51]:

$$C_n = \frac{(n-1)(n-2)}{2}\left(\frac{R}{1-R}\right)^2 \tag{2.16}$$

Equation 2.16 shows that the stronger the FBGs are, the higher the crosstalk is. The crosstalk also becomes stronger as the number of FBGs increases.

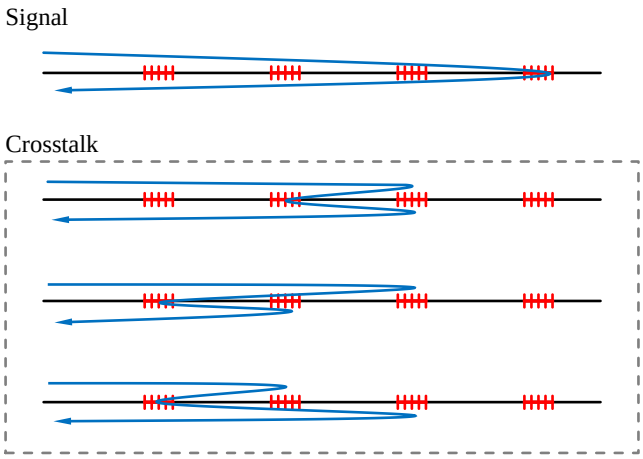

Figure 2-21 Mechanism of crosstalk and evolution of crosstalk as number of FBGs increases

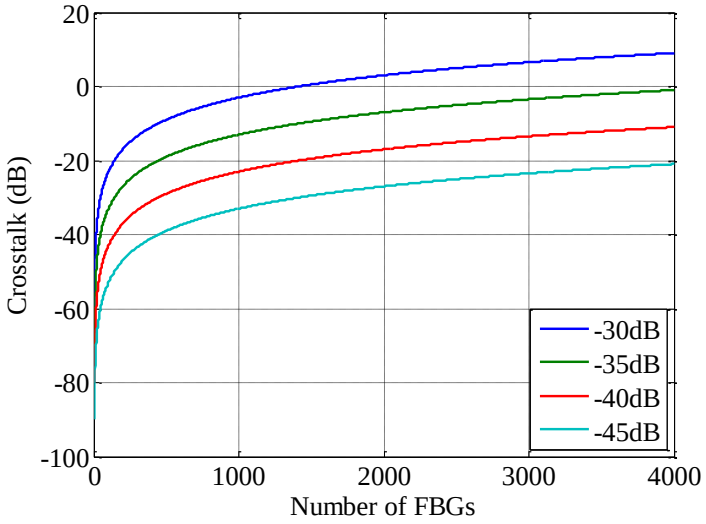

Figure 2-22 Crosstalk versus number of FBG and reflection

Figure 2-22 shows the dependence of crosstalk on the reflectivity and number of FBGs. For strong FBGs, the power from the crosstalk may become even higher than that of the

signal pulse. When the reflectivity is -40dB, the highest crosstalk is less than -20dB for the 1,000th FBG, which is sufficiently low for signal demodulation. So considering the power depletion and crosstalk, -40dB is a reasonable choice for a 1,000-element sensing link.

Another form of crosstalk may come from spectral shadowing, which is also induced by the reflections by the FBGs between the light source and the target FBG. For the *n*-th FBG, the reflections by the 1st to the *(n-1)*-th FBG not just reduced the incident power to it, but modify its spectrum. So the spectrum of the reflected light by the *n*-th FBG is not simply a multiplication of the incident spectrum and the FBG's reflecting spectrum, instead, it has the form of:

$$R_n(\lambda) = S(\lambda)\cdot\left[1-R(\lambda)\right]^{2(n-1)} \tag{2.17}$$

in which $S(\lambda)$ is the spectrum of the light source, $R(\lambda)$ is the reflecting spectrum of the UW-FBG, $1-R(\lambda)$ is the transmittance of the FBG. Assuming the incident light has uniform spectrum and the FBGs have Gaussian shaped reflecting spectrum expressed as [51]:

$$R(\lambda) = R_{FBG}\cdot\exp\left[-4\ln 2\left(\frac{\lambda-\lambda_{FBG}}{B_{FBG}}\right)\right] \tag{2.18}$$

Figure 2-23 shows the distortion caused by spectral shadowing when the FBGs have reflectance of -35dB and -40dB. The calculated spectra show that not only is the peak reflectance lower than the real value, which is already represented by power depletion, but also the shape of the reflecting spectrum is distorted to a different degree. But the proposed sensing scheme measures the pulse delay instead of the spectra of the FBGs, this distortion does not have direct influence on the measurement. The flattening of the spectrum can cause a pulse distortion in the time domain, but this is only influential when the distortion is so significant that the pulse distortion affects the results of crosstalk. Comparing with the power depletion and the crosstalk from multiple reflections, this is a minor issue.

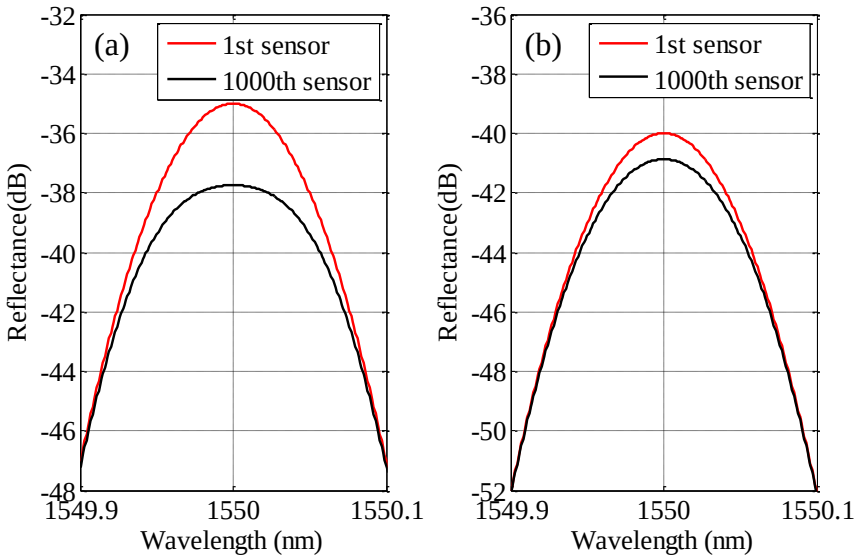

Figure 2-23 Spectral shadowing with reflectance of (a) -35dB and (b) -40dB

2.4.3 Position dependent reflectance

Since the power depletion comes from the previous reflection, it is inevitable that the power reflected by an FBG is weaker than that by the preceding FBGs. This could be compensated by increasing the reflectance along the fiber. The reflectance could be carefully managed that the reflectance of the *n*-th FBG can compensate the loss introduced by the fiber and the preceding FBGs. Assuming that the *n*-th FBG has reflectance of r_n, the reflectance of the *(n+1)*-th FBG is:

$$r_{n+1} = \frac{r_n}{\alpha^2 (1 - r_n)^2} \tag{2.19}$$

Given different initial reflectance, the reflectance of the following FBGs will increase at different rate. At a certain point, the required reflectance will be too high to be considered as the UW-FBG and may even not be practical to fabricate, so there will be a maximum number allowed. Figure 2-24 plots the variation of the reflectance of the FBG along the fiber if this scenario is used. The fiber loss is assumed to be 0.22dB/km and the FBG spacing is 1 m. If the sensing link starts with a stronger FBG, the reflectance of the subsequent FBGs increases faster to compensate for the loss introduced by the fiber and

the previous FBGs. When the first FBG has reflectance of -45dB, the reflectance of the 4,000th FBG is -41.62dB, which is still quite weak. However, for stronger FBGs, the reflectance can increase to a quite high level. When starting with -30dB, the 440th FBG is already as reflectance of around -20dB. For -35dB and -40dB, the numbers at which the reflectance reaches -20dB are 1,419 and 3,998. Given a maximum reflectance allowed, there will a maximum number of FBGs achievable.

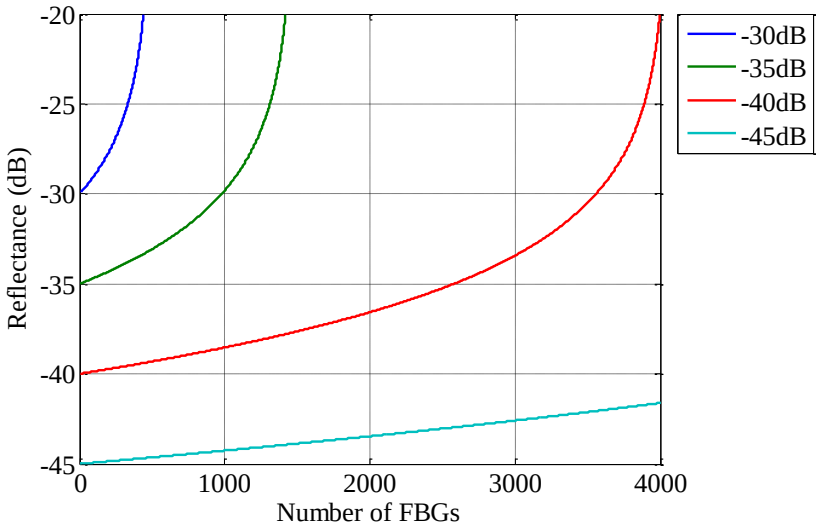

Figure 2-24 Reflectance variation along the fiber if the reflected power is maintained

This is just a theoretical method to solve the problem of power depletion and it has some drawbacks. One drawback is that the fabrication of such a sensing link is not as simple as that of identical FBGs. To ensure that the reflected power is the same, the reflectance of the FBGs should always be monitored in the FBG writing process, and this makes it rather difficult to write FBGs in a fiber during the fiber fabrication. Another drawback is that the wavelengths of the FBGs may not be the same at all times because the change of environment is expected. In this case the constant reflected power is no longer exactly maintained.

2.5 Simulation of influential factors

The ability to accurately calculate the delay defines the performance of the system because the measurands are deduced from the delay. Several factors are crucial to the

delay calculation. Some of these factors include the system SNR, the input laser pulse width, the ADC sampling rate and the total dispersion of the dispersive unit. Using the algorithm provided in Section 2.3 and the Gaussian pulse assumption described in the same section, the influence of each factor could be simulated.

2.5.1 Signal to noise ratio

Since UW-FBGs are used in the sensing link, the returned pulses are naturally weaker comparing with other schemes where stronger FBGs are employed. The algorithm exploits cross-correlation which has high tolerance of the noise, but it is necessary to evaluate the influence of the SNR in order to understand the requirements on the key components in the system. As it is mentioned above, the total dispersion is a factor which influences the performance, because it determines the conversion factors from delay to strain and delay to temperature. So the simulations are all carried out under different dispersions. It should also be mentioned that the total dispersion also influences the pulse broadening but it can be kept under a negligible level by limiting the total dispersion and pulse width.

In order to provide more straight forward results, the simulation results are given in strain, by assuming the strain coefficient of the FBGs are 1.23pm/με. Gaussian white noise was assumed to be the only noise source. The input pulse had a Gaussian profile and full width at half maximum (FWHM) of 2ns. The sampling rate was assumed to be 40GS/s. At each SNR and dispersion, 100 calculations were performed and the standard deviation of the delay was used to determine the resolution of the strain. The strain resolution was obtained by dividing the delay standard deviation by the delay-to-strain conversion factor, which was calculated by multiplying the strain coefficient of the FBG and the dispersion of the dispersive unit. Dispersion used in simulation was negative because dispersion compensating devices usually have negative dispersion.

The simulation results are shown in Figure 2-25. Figure 2-25(a) and (b) gives the dependence of the strain resolution on SNR with different dispersion. The first conclusion from the results is that the resolution improves exponentially as SNR increases. Another observation is that higher dispersion provides better strain resolution.

This is quite expected because higher dispersion means that the same amount of strain will cause larger delay, and thus make the strain easier to be detected.

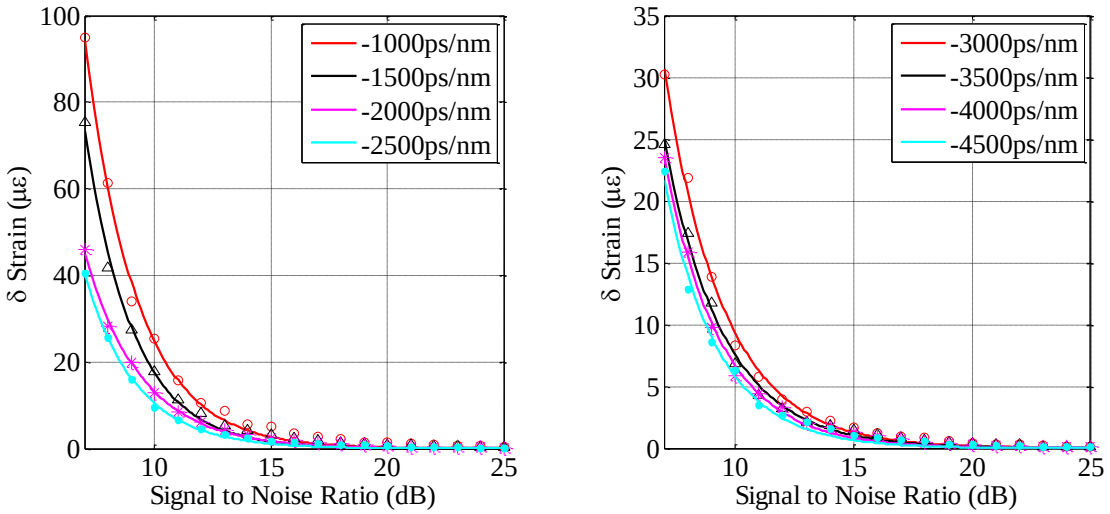

(a) With lower dispersion

(b) With higher dispersion

Figure 2-25 Dependence of strain on SNR of the received signal. Markers: simulated values. Solid lines: exponentially fitted curve

With dispersion of -2,500ps/nm, in order to have strain resolution of 10με, the required SNR is around 10dB. If the SNR is increased to 15dB, the strain resolution is improved to about 1με. If the dispersion is -4,500ps/nm, for SNR of 10dB, the strain resolution is 6.3με, which is equivalent to the value when dispersion is -2,500ps/nm and SNR is 11dB. In this case, improving the SNR by 1dB is as effective as increasing the dispersion by 2,000ps/nm, so SNR has a more significant impact on the system's performance.

2.5.2 Pulse width and sampling rate

Pulse width is another factor which has influence on the resolution of sensing. One straight forward way to understand this is that the same amount of change in delay will be more detectable for a narrower pulse. However, other factors such as the sampling rate, and the bandwidth of modulation and detection, can limit the pulse duration. Also, shorter pulses carry less energy and the SNR may be compromised when the optical signal is amplified by an EDFA. Simulations are also carried out to study the influence of pulse

width under the same circumstances as it was in the previous SNR simulation, except that the SNR here is fixed at 15dB, and the results are shown in Figure 2-26. The simulations show that as the pulse gets broader, the standard deviation of strain increases linearly. When the dispersion is -1,500ps/nm, and the pulse width is increased from 1ns to 2ns, the strain resolution increases from 3.3με to 4.7με. To maintain the same level of resolution while pulse width is 2ns, the dispersion should be increased from -1,000ps/nm to -1,500ps/nm. The same resolution can be achieved with pulse width of 3.3ns if the dispersion is -2,000ps/nm. For higher dispersion, similar relation holds.

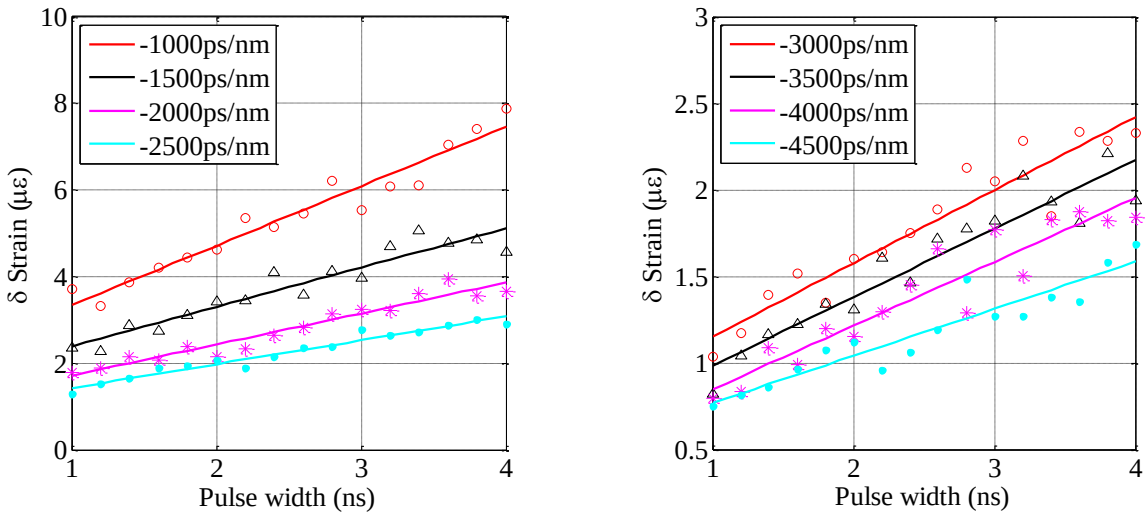

(a) With lower dispersion

(b) With higher dispersion

Figure 2-26 Dependence of strain resolution on pulse width. Markers: simulated values. Solid lines: linearly fitted curve.

The previous simulations were carried out by assuming a sampling rate of 40GS/s, which is achievable by a high speed oscilloscope, but it has high cost and it would be better if lower sampling speed could also provide reasonable performance. The relation between the strain resolution and time interval (sampling rate) can provide a guideline to determine a sampling rate given the targeted performance. With pulse width of 2ns and SNR of 15dB, the dependence of the resolution on the sampling interval was obtained by simulation and is shown in Figure 2-27. Standard deviations were calculated from results of 100 simulations.

According to the results, as the sampling interval increases, the strain standard deviation increases linearly. When the dispersion is -1,000ps/nm, and the sampling interval is increased from 25ps to 100ps, the corresponding strain resolution increases from 5.4με to 9.5με. Since the standard deviation increases as the sampling interval increases and higher total dispersion provides better performance, it is possible to use higher dispersion to compensate the degradation caused by the larger sampling interval. It should be noted that this simulation was carried out with SNR of 15dB, which is relatively high in this scheme. For a lower SNR, the resolution will be mainly limited by the SNR other than the sampling rate. It should be mentioned that a larger sampling interval has another advantage, which is, for the same pulse width, it results in fewer data points, which reduces the workload of the subsequent signal demodulation.

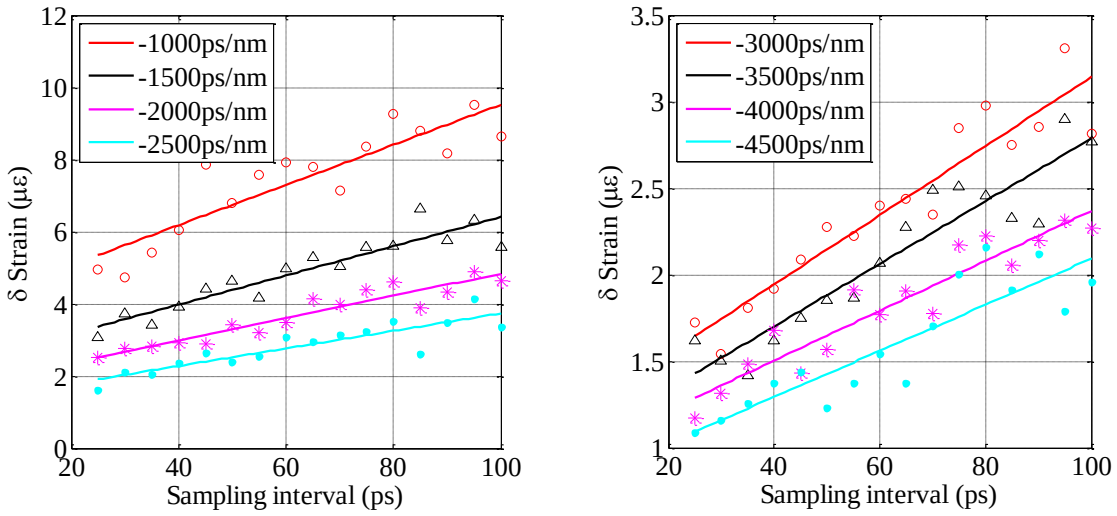

(a) With low dispersion

(b) With high dispersion

Figure 2-27 Dependence of strain resolution on sampling interval

Furthermore, commercial analog-to-digital converters (ADCs) are available for sampling speed of around 2GS/s, so it would be useful to find out the performance when the sampling rate is set to this level. In this case, because the sampling interval is several hundreds of picoseconds, to have enough data points from one pulse, FWHM of the pulses has to be increased. According to the previous simulation, a broader pulse requires a larger dispersion to maintain the same system performance. The simulations are carried

out for a broader pulse, which is 4ns, larger sampling intervals and higher dispersion. Figure 2-27 plots the results of the simulations. From the results it is noted that when the sampling interval is increased to 500ps, dispersion of -2,000ps/nm gives a strain resolution around 20με, while dispersion of -4,000ps/nm can provide a strain resolution of lower than 8με, and higher dispersion can further improve the performance.

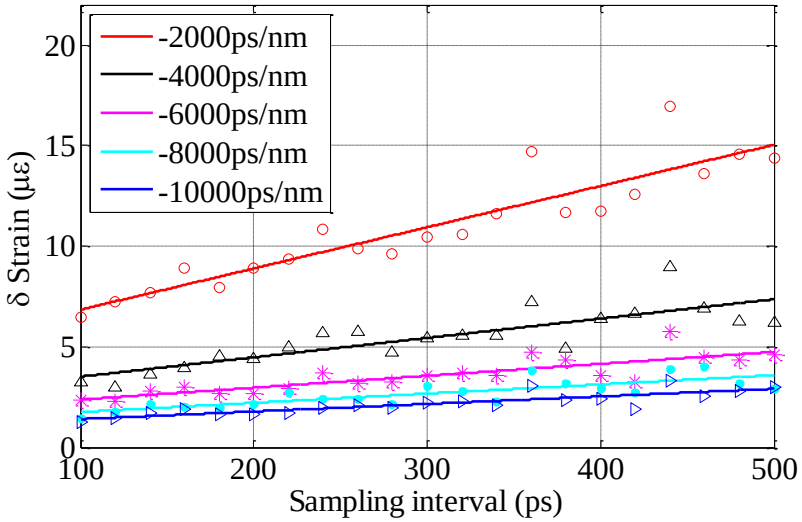

Figure 2-28 Dependence of strain resolution on larger sampling interval

All the simulations were carried out based on some assumptions, such as Gaussian pulse and Gaussian white noise. However, in a real system, these conditions are not guaranteed. Also the timing jitter of the pulses and the sampling clock may also have unnegligible influence on the performance of the system. This simulation is intended to be a general guide line to determine some key factors of the system.

Chapter 3 System implementation and proof of concept demonstration

3.1 System implementation

This chapter discusses the implementation of the sensing system in detail, including the design or selection of the light source, the sensing link, the dispersive unit and the detection part.

3.1.1 Light source

The light source is a key component of the system. It should provide a bandwidth large enough to cover the wavelength range corresponding to the extreme temperatures or strains of interest. In the meantime, the source should also have pulsed output that has appropriate pulse width narrow enough to avoid overlap between adjacent pulses yet permits enough sampled data points within the pulses reflected from the FBGs. In this section, two options to setup the light source are presented, one is to modulate a broadband light source, and the other one is to use a supercontinuum light source.

3.1.1.1 Modulation of broadband light source

One direct way to get pulsed broadband light source is to modulate a CW broadband light. Since the required bandwidth is normally several or maybe ten nanometers, regular laser is not an option. Light emitting diodes (LEDs) usually have very large bandwidth so they could be used. Similarly, ASE from an EDFA, which ranges from 1530nm to 1560nm, can also act as a broadband light source.

An LED and ASE sources are both suitable for building the light source but they both have a drawback of low spectral power density for the light coupled into a singlemode fiber.

Superluminescent diode (SLD), which is an edge emitting light source, has broad bandwidth as LED but higher output power similar to laser diode. SLDs can have a bandwidth ranging from several tens of nanometers to the order of 100nm, and the total

power could be as high as several tens of milliwatts. This feature makes it a better option comparing with LED and ASE sources.

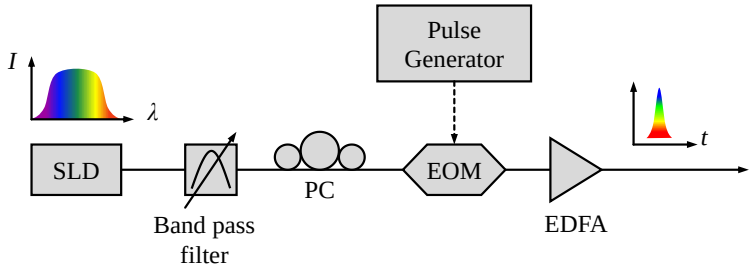

Figure 3-1 Light source based on SLD

Figure 3-1 shows the proposed light source based on an SLD and external modulation. Before the modulation, a bandpass filter is inserted to limit the bandwidth to a desired value. The light then passes through a polarization controller and is modulated by an EOM driven by a pulse generator. The pulse width and repetition rate can be controlled by the pulse generator. An EDFA follows the modulator to amplify the pulse to a higher level, which is needed because the FBGs are expected to be weak.

A benchtop superluminescent light source (Thorlabs S5FC1005P) with central wavelength of 1559.5nm, bandwidth of 63.3nm and output power of 11.5dBm was used to demonstrate this design. The bandpass filter which followed the SLD was a tunable filter with both the center wavelength and the bandwidth adjustable (Santec OTF-350). The filter was centered at 1553nm and the bandwidth was set to 8nm. For FBGs with a thermal coefficient of 12pm/ºC, this allows a dynamic range of more than 650ºC.

The pulse generator (AVTECH AVM-C) driving the 2.5GHz EOM had a tunable pulse width and repetition rate, giving more flexibility to the measurement. A low noise EDFA was used here to amplifier the signal. By changing the driving current of the EDFA, the peak power of the output pulse can range from several mW to 0.5W.

The quality of the pulse was investigated under various conditions, as it is shown in Figure 3-2. The detector used had bandwidth of 12GHz and conversion gain of -600V/W. The pulses in Figure 3-2 are inverted because of the negative gain. The data was digitized by an oscilloscope (LeCroy 720Zi) and plotted in persistent mode with duration of 1s.

The pulse width was set to 1ns for the measurement and the bandwidth of the oscilloscope was 2.5GHz. The initial pulse (Figure 3-2 (a)) does not have a Gaussian shape because the output of pulse generator becomes flat-topped when the pulse width is greater than 0.5ns. The initial pulse is noisy partly because of the amplification and partly because the electrical pulse applied to the EOM has high timing jitter, but averaging can reduce the noise effectively. It could be found from comparison that after being reflected, and amplified and passing through the DCF, the signal to noise ratio (SNR) of the pulse has degraded significantly, but certain times of averaging provide an obvious improvement.

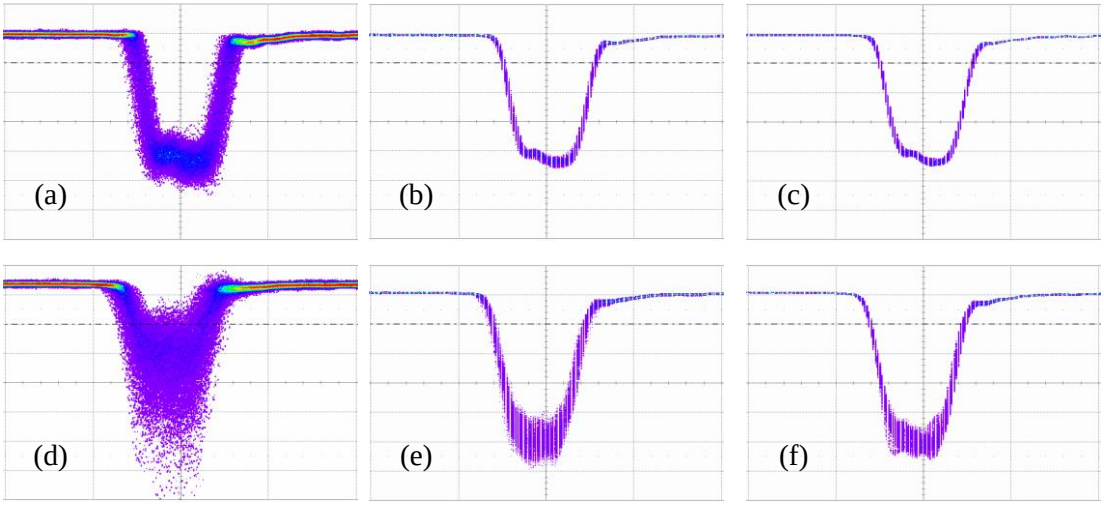

Figure 3-2 Pulse from the SLD based light source (1ns/div). (a), (b) and (c): pulse after amplification with no average, 10 times of average and 20 times of average respectively. (d), (e) and (f): pulse reflected by a FBG with -15dB reflectance, amplified again and passed through the DCF, with no average, 10 times of average and 20 times of average

Although the signal to noise ratio seems not satisfactory even after the data averaging, further strain test shows that a reasonable standard deviation can be obtained using the algorithm proposed, of which details are provided in Section 3.2.4. Not to mention that the detector and oscilloscope have large bandwidth. When broader pulses are used, the bandwidth can be reduced and it will help to filter out part of the noise.

3.1.1.2 Supercontinuum light source

Another option to build a required light source is to start from a light source that already has broadband and pulsed light. One example is a supercontinuum source. A

supercontinuum source is a coherent light source with ultra-wide bandwidth. The broad bandwidth is generated by the effect of multiple nonlinear effects, including self-phase modulation, cross-phase modulation and four-wave mixing, when a super strong short pulse is injected to a nonlinear medium [41]. The pulse width of the original pulse is usually on the order of picoseconds and some are even narrower, at the level of femtoseconds. Due to the nonlinear effect induced broadening of the spectrum, the pulse gets broadened in time domain at the same time because of the dispersion. When the supercontinuum light is generated, the pulses are usually broadened. A supercontinuum light source can cover wavelengths ranging from several hundreds of nanometers to several micrometers [41]. Over the years, different nonlinear media have been used for supercontinuum generation, some of which include liquids, gases, single- or multi-mode fiber, high-nonlinear fiber, photonic crystal fibers and other special fibers. In nowadays, PCF is quite commonly used as the nonlinear medium to generator supercontinuum spectrum.

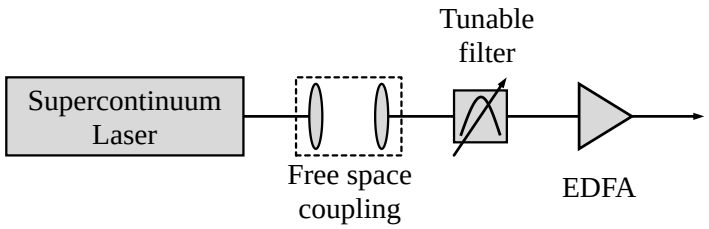

Figure 3-3 Light source based on supercontinuum light source

Figure 3-3 is the setup of the light source based on a supercontinuum light source (NKT Photonics superK COMPACT), whose spectrum covers the wavelength range from 450nm to 2400nm. It has output with a repetition rate of about 21kHz and a pulse with of about 2ns, neither the pulse width nor the repetition rate is tunable. It uses a PCF as the nonlinear medium. Because of its special structure, the fiber end could easily be damaged by reflections if it is connected to a regular fiber. A free space coupling system (Thorlabs FBP-C-FC) was used to couple the light to another single mode fiber without causing damage. A tunable filter centered at 1553nm was then used to limit the bandwidth to 8nm before the light was amplified by an EDFA. The peak power of the pulse after amplification was about 250mW.

The filtering was necessary because the bandwidth of the supercontinuum light is more than sufficient for the system's needs. The additional wavelength components will compromise the amplification to the part of the spectrum that was useful, because the gain of the EDFA would be contributed to a larger range other than only to the several nm range as needed. Besides, when the full bandwidth of the supercontinuum light source was used, part of the light at unwanted wavelengths could go from port 1 to port 3 of the circulator in Figure 2-1. Usually the isolation between port 1 and port 3 of a circulator is lower than -50dB, but the light passing through the circulator had large bandwidth and the total power was not negligible comparing with the power reflected by UW-FBGs, and this was a source of crosstalk. For the two reasons above, limiting the bandwidth was necessary and will benefit the SNR of the signal.

Pulses with and without passing through the components following the EDFA were captured and are shown in Figure 3-4. Similar to the case when an SLD was used as the source, pulses are noisy but data averaging can improve the signal quality significantly. Comparing with the pulse produced by the previous scheme, pulses here have a shape closer to a Gaussian profile but they do have some fine features, which may arise from the nonlinear effects.

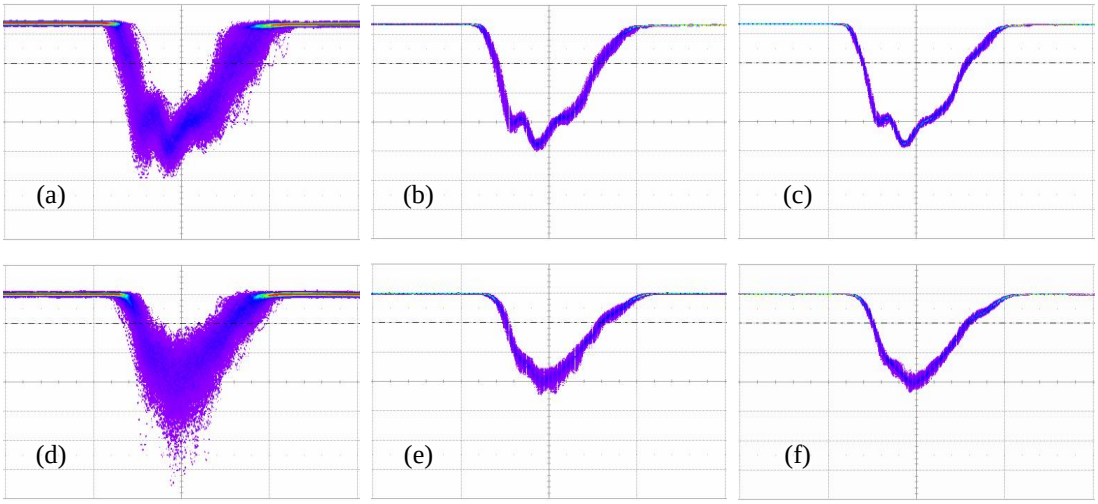

Figure 3-4 Pulse from the supercontinuum based light source (2ns/div). (a), (b) and (c): pulse after amplification with no average, 10 times of average and 20 times of average respectively. (d), (e) and (f): pulse reflected by FBG with reflectance of -15dB, amplified again and passed through the DCF, with no average, 10 times of average and 20 times of average

The two setups have their advantages and disadvantages respectively. The supercontinuum light source based design is more compact but the repetition rate is not stable, which is the characteristic of a supercontinuum light source. Also the pulse width and repetition rate are both not adjustable. The SLD based source in contrast is less compact and pulses are flat-topped, but it provides the possibility of changing both the pulse width and repetition rate, so the pulse could be optimized and the sensing speed can be increased for a smaller sensing range.

3.1.2 Sensing link

3.1.2.1 FBG fabrication introduction

The sensing link consists of a large number of UW-FBGs, which can be fabricated in different methods. But the basic idea is to use ultra-violet light to induce periodic refractive index variation in the fiber core. This is achievable because the dopant in most of regular single mode fiber is Germanium. Germanium doped silica exhibits photorefractivity and its refractive index can be permanently changed by ultra-violet (UV) light exposure. The FBG can be either inscribed during the fiber drawing process or after the fiber is fabricated [62, 69].

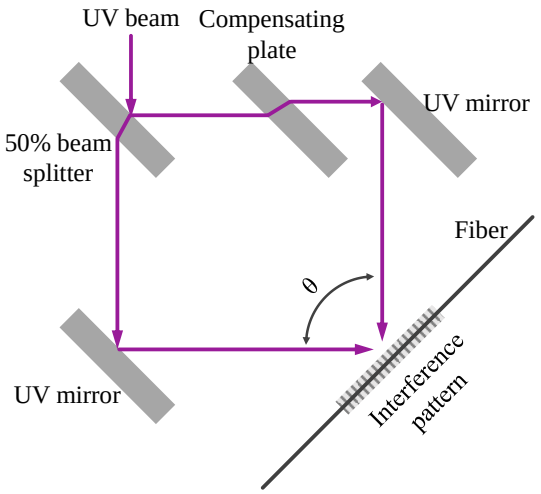

Figure 3-5 The bulk interferometer method for fabricating FBG using UV radiation [69].

In the past decades, many methods of FBG inscription in a fiber are proposed and demonstrated. One of them is called bulk interferometer [69], as illustrated in Figure 3-5.

The idea is to split one UV beam into two, then arrange the light paths such that the two laser beams interfere with each other with an angle of θ. Due to the interference, there will be a periodic laser intensity pattern at the intersection of the two beams. The period or pitch of the interference fringes is dependent on the angle between the two beams. By the placement of a fiber in this interference pattern, an FBG may be inscribed, of which the reflecting wavelength can be controlled by adjusting θ. The relation between the FBG's reflecting wavelength and the angle is [69]:

$$\lambda_{FBG} = \frac{n_{eff}\lambda_{uv}}{n_{uv}\sin(\theta/2)} \tag{3.1}$$

where λ_{FBG} is the reflecting wavelength of the FBG, n_{eff} is the effective refractive index of the fiber, λ_{uv} is the wavelength of the UV light, and n_{uv} is the refractive index of silica at λ_{Fuv}. The compensating plate is used to balance the two paths if the UV beam has low coherence.

The beam splitting could be achieved by the use of mirrors or a phase mask, as the setup in Figure 3-6 shows [69].

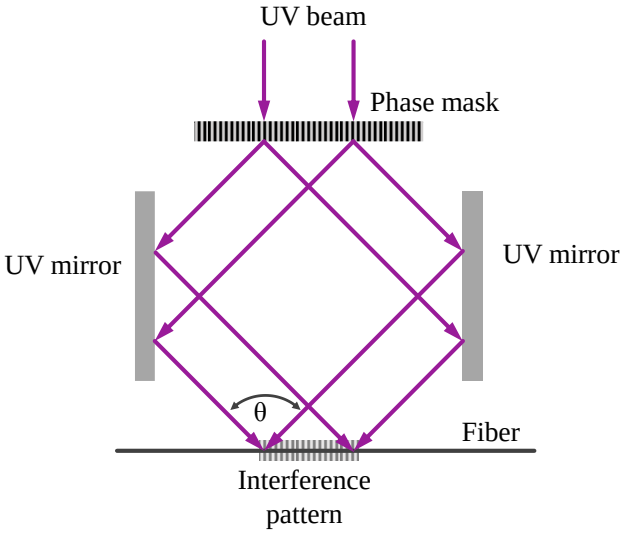

Figure 3-6 FBG fabrication using phase mask as beam splitter and wavelength defining component

The incident beam is diffracted by the phase mask to -1, 0 and 1 order, of which the angle between the -1 and 1 orders is defined by the period of the phase mask. If these two beams are brought together by two parallel UV mirrors, which are also perpendicular to the phase mask, an interference pattern can be formed as the previous setup, and an FBG can be inscribed by placing the fiber at the intersection of the two beams. The wavelength is also adjustable by rotating one or both of the UV mirrors. A cylindrical lens could be added right before the fiber or the phase mask to increase the density of the light on the fiber.

The fiber could also be placed right beneath the phase mask, in the region where the two beams overlap. In this case the wavelength of the inscribed FBG is purely determined by the phase mask itself. It should be noted that the fiber has to be placed close to the phase mask in order to maximize the FBG length. This scheme is simpler than the previous two methods, but it also has the drawbacks of inability to avoid the 0 order light as well as the possible higher order beams if the incident light is not strictly perpendicular to the phase mask.

For an FBG with a reflecting wavelength of 1.5μm, its period is around 0.5μm. Since the diffraction limit of UV light is around 0.25μm, it is possible to write FBGs in a fiber by the point-by-point method [69]. The period of the FBG is determined by the step size of fiber movement. This method is straight forward but may not be practical for writing long gratings because it requires very high position accuracy.

The UW-FBG link used as the sensing link here was fabricated in the fiber drawing process, by placing the fiber next to the phase mask before the bare glass fiber was coated [62]. Each grating was written by only one pulse, so by controlling the fiber drawing speed and the repetition rate of the UV pulses, the spacing between FBGs can be precisely controlled. This method is suitable for mass production given its fabrication efficiency and uniformity.

3.1.2.2 FBG Modeling

As it is briefly described in Section 2.1.2.1, the reflecting and transmitting characteristics of an FBG can be explained by multiple beam interference. Usually the characteristics of an FBG are analyzed by the mode coupling theory, based on the assumption of weak coupling and slow varying envelop approximation (SVEA). The weak coupling assumption is satisfied in most of the FBGs because the UV light induced refractive index change is considerably lower than that of silica refractive index itself. The SVEA, which is expressed as:

$$\frac{\partial^2 A_\mu}{\partial z^2} << \beta_\mu \frac{\partial A_\mu}{\partial z} \tag{3.2}$$

in which A_μ is the envelop of the μ-th mode, and β_μ is the propagation constant of this mode. This relation indicates that the variation of the envelop of the electric field in the direction of propagation is slow over a distance of the wavelength of the light [69], which is satisfied in most of the cases because the pulse duration in space is much longer than the light wavelength.

The reflection of an FBG can be described as the mode coupling between the forward and backward propagating fundamental modes in the fiber, which are both LP_{01} modes.

Assuming the refractive index profile of the FBG in the fiber core is [70]:

$$n(z) = n_1 \left\{ 1 + \sigma(z) \left[1 + m \cdot \cos\left(\frac{2\pi}{\Lambda} z \right) \right] \right\} \tag{3.3}$$

where n_1 is the refractive index of the core when the FBG does not exist, $\sigma(z)$ is the profile of the FBG, m indicates the amplitude of the refractive index variation, and Λ is the period of the FBG.

The mode coupling equations between the forward and backward propagating core modes are [70]:

$$\begin{aligned}\frac{dA}{dz} &= j\kappa A + j\frac{m}{2}\kappa B\exp\left[-j\left(2\beta-\frac{2\pi}{\Lambda}\right)z\right]\\ \frac{dB_{\mu}}{dz} &= -j\kappa B - j\frac{m}{2}\kappa A\exp\left[j\left(2\beta-\frac{2\pi}{\Lambda}\right)z\right]\end{aligned} \tag{3.4}$$

where A is the amplitude of the mode traveling in the +z direction, B is the amplitude of the mode traveling in the –z direction, β is the propagating constant of the LP_{01} mode, and κ is the mode coupling coefficient, which is determined by the overlap of the two modes:

$$\kappa = \frac{\omega\epsilon_0 n_1^2\sigma(z)}{2}\int_0^{2\pi}d\phi\int_0^a rdr\left(\left|E_r\right|^2+\left|E_\phi\right|^2\right) \tag{3.5}$$

in which ω is the angular frequency of the light, ϵ_0 is the permittivity of the vacuum, a is the radius of the fiber core, E_r and E_ϕ are the electrical field component in the r and ϕ direction. Here κ is the 'DC' mode coupling coefficient, while $m\kappa/2$ is the 'AC' component.

For non-uniform FBGs, of which $\sigma(z)$ is not a constant, the coupled differential equations can be solved numerically. For uniform FBGs, the coupling coefficient is also a constant. In this case Equation 3.4 is a set of differential equations with constant coefficients, and they can be analytically solved and the reflecting spectrum is given by [71]:

$$R = \frac{\left|\frac{m}{2}\kappa\right|^2\sinh^2\left(\sqrt{\left|\frac{m}{2}\kappa\right|^2+\left(\kappa+\frac{\Delta\beta}{2}\right)^2}\,L\right)}{\left|\frac{m}{2}\kappa\right|^2\cosh^2\left(\sqrt{\left|\frac{m}{2}\kappa\right|^2+\left(\kappa+\frac{\Delta\beta}{2}\right)^2}\,L\right)-\left(\kappa+\frac{\Delta\beta}{2}\right)^2} \tag{3.6}$$

where L is the length of the FBG and

$$\Delta\beta = 2\beta-\frac{2\pi}{\Lambda} \tag{3.7}$$

Given the parameters of the fiber and the FBG, the transmitting spectrum can be calculated from Equation 3.6 and 3.7 as well.

3.1.3 The dispersive unit

Two types of dispersive units have been discussed in Chapter 2. The two designs of the dispersive unit can be easily modified from one to the other by adding or removing the beaming combing coupler. For the dispersive element, the most comment option is the DCF as it is widely used in optical communication and having a lower cost comparing with the PCF.

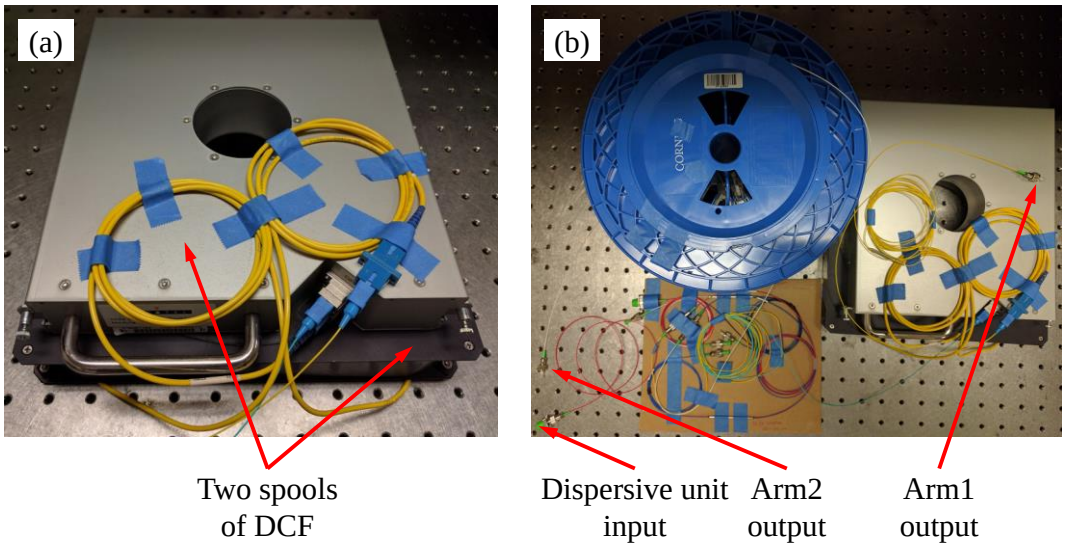

Figure 3-7 Dispersive element and dispersive unit (a) Two spools of DCF as dispersive element (b) dispersive unit based on DCF

The dispersive element used in the system had two sections of DCF, with combined total length of about 22km and total dispersion of -2,387ps/nm, shown in Figure 3-7(a). Figure 3-7(b) shows a branch-structured dispersive unit using the DCF. The two spools of DCF were placed in Arm1 and another spool of 22km long regular single mode fiber (Corning SMF28) was placed in Arm2 to balance the two arms. SMF-28 usually has positive dispersion of 18ps/nm/km, so Arm2 had additional dispersion of about 396ps/nm, making the total effective dispersion of the entire structure to be about -2,783ps/nm. This number is just a rough estimation and a more accurate dispersion measurement will be presented

in Section 3.2.1. This dispersive unit could be easily changed to the Mach-Zehnder structure by combining the two outputs using another fiber coupler. Depending on the length of the sensing fiber, the length of Arm2 could be adjusted to avoid pulse overlap.

It is relatively low cost using DCF as the dispersive element but it has one drawback, which is the difference of the delay introduced by the two arms is sensitive to the temperature of the environment. That is, even if the FBGs are in a stable state, the detected delay can still change if the dispersive unit is not well isolated to the variation of the environment temperature. The influence of temperature on the dispersive unit can have three origins:

a. Temperature difference in the two arms

Considering the fact that the size of both the DCF and the SMF28 are large in this setup, it is possible that the temperature is not uniform in the entire dispersive unit. For equal arm length of about 22km, if the thermo-optic coefficient is 8.6×10^{-6} [72], the extra delay introduced by temperature difference in two arms will be:

$$\Delta\tau_1 = \frac{L\alpha}{\nu} = \frac{22\times10^3 m\times 8.6\times10^{-6}/^o C}{2\times10^8 m/s} \approx 946 ps/^o C \qquad (3.8)$$

where L is the average length of the arms and α is the thermo-optic coefficient of the fiber. The result means if temperature difference between the arms changes by 1ºC in a measurement, the delay will change by 946ps, which is significant. Since this term is proportional to the length of the arms, one way to reduce the influence is to reduce the length of the arms. However, for the DCF, a shorter length means lower total dispersion, which directly affects the wavelength-to-delay conversion coefficient and thus has significant impact on the sensitivity. So it is better to either keep the dispersive unit in a controlled stable environment, or use different device as the dispersive element instead of DCF.

b. Length difference

The length difference is an issue of consideration if the dispersive unit is the Mach-Zehnder structure. For this structure, the two arms should have a length difference which is twice the length of sensing fiber to avoid overlapping. Because of the existence of the length difference, a temperature change to the M-Z structure will also introduce an additional delay, even if the two arms always have the same temperature. For a sensing range of 1km, the minimum required length difference is 2km, if the temperature of the M-Z changes, the additional delay will be:

$$\Delta\tau_2 = \frac{\Delta L\alpha}{v} = \frac{2\times10^3 m\times8.6\times10^{-6}/^o C}{2\times10^8 m/s} \approx 86 ps/^o C \qquad (3.9)$$

which is also not a negligible value. This is not a problem for the branch-structured dispersive unit though. If the Mach-Zehnder structured dispersive unit is used, it is also necessary to keep the unit at a constant temperature

c. Thermo-optic coefficient difference

Because the two arms have different types of fibers, which differ in both structure and material because the dopant type and concentration may be different, it is unavoidable that the thermo-optic coefficients are not exactly the same. Similarly, this will also cause unwanted delay as temperature of the M-Z structure changes, assuming there is 1% difference, the delay introduced by the thermo-optic coefficient difference is:

$$\Delta\tau_3 = \frac{L\Delta\alpha}{v} = \frac{22\times10^3 m\times8.6\times10^{-6}/^o C\times0.01}{2\times10^8 m/s} \approx 9.46 ps/^o C \qquad (3.10)$$

This effect is less significant compared to the previous two, but it still requires precise temperature control of the structure.

There are several methods to get this problem addressed. One direct way is to place the M-Z structure in a space with temperature control. The temperature should be controlled at a calibrated temperature with small fluctuation. However, the size of the structure is

relatively large due to the long lengths of the DCF and SMF, and this makes it difficult to control their temperatures with high stability.

Another possible solution is to use another device that has a compact size and large dispersion as the dispersive element. As it is mentioned in Section 2.1.3.4, some PCFs and chirped FBG can be designed to have very large dispersion yet a small footprint. However, if the Mach-Zehnder structure dispersive unit is used, replacing the dispersive unit has limited effect because the arm imbalance is required. This is a lesser problem if a branch-structured dispersive unit is used.

There is one more method to get this problem solved and it does not require dispersive element with smaller size. The dispersive unit can be placed in an environment without dramatic temperature fluctuations. Meanwhile, by placing a reference FBG at the beginning of the sensing link and having its temperature precisely controlled, any temperature variation of the dispersive unit is reflected by the delay demodulated from this reference FBG. By subtracting this reference delay from the demodulated signal, the influence can be effectively eliminated. Also, because a single FBG has very small size, controlling its temperature can be achieved with low cost and minimum effort.

3.1.4 Signal detection and acquisition

Since UW-FBGs are used, it is expected that the returned pulses are weak. In this case, it is preferred that the photodetectors have a high gain so the detected electrical signal is high enough for digitization.

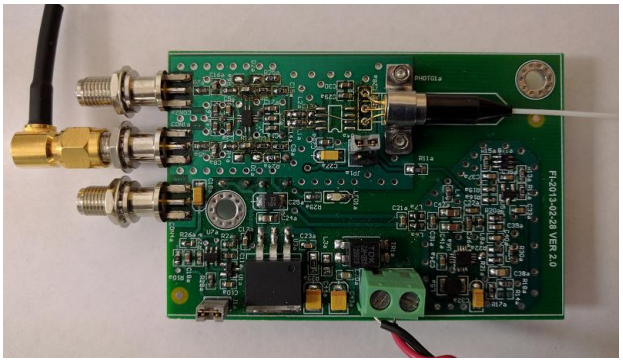

Figure 3-8 APD followed by TIA

The photodetectors used in the systems were two avalanche photodiodes (APDs) with responsivity of 0.85A/W, followed by a transimpedance amplifier with load resistance of 20kΩ. Since the APD magnifies the current by 10 times, the detectors have a conversion gain of 1.7×10^5V/W, and their bandwidth is 200MHz. Figure 3-8 shows one of the actual detectors.

The detected pulses were sent to a high speed oscilloscope (LeCroy 720Zi), and the oscilloscope acted as an analog to digital converter and had the ability of saving the acquired data. The oscilloscope had a maximum bandwidth of 2.5GHz and maximum sampling rate of 40GS/s. Both of the bandwidth and the sampling rate were adjustable, which could help test the performance of the system under different conditions. One drawback was that the oscilloscope had a resolution of only 8bit and the effective number of bits (ENOB) was around 6bit. Usually low ENOB introduces more quantization noise, but in this system, it is a noise source that can be safely ignored. Detailed analysis is given in Section 4.3.

3.2 Proof-of-concept demonstration

An experiment was setup based on the scheme in Figure 2-1, light sources in Figure 3-1, Figure 3-3 and M-Z structure in Figure 2-5(a) to perform a proof-of-concept demonstration. The aim was to test the strain response of the FBG, and demonstrate its ability of high speed sensing. Since it was a proof-of-concept experiment, only two FBGs were used and because the total number was 2, stronger FBGs with reflectance of about -15dB were used.

3.2.1 Setup and split-step test

Figure 3-9 (a) shows the design for static strain response test. Two metal hooks were attached to the two bare fiber ends of one of the FBGs by super glue. Of the two hooks, one was attached to a force gauge (Mark-10 M5-05), which was vertically mounted on an optical table, and the other was loaded with a plastic bottle with a damper at its bottom. Here the FBG with strain applied was named FBG_1 and the other FBG_2, and the spacing between them was 4.4m. In this setup, the output of Arm1 and Arm2 in Figure 3-7 were

recombined using another fiber coupler to from a Mach-Zehnder structured dispersive unit, of which the arm length difference was 12m.

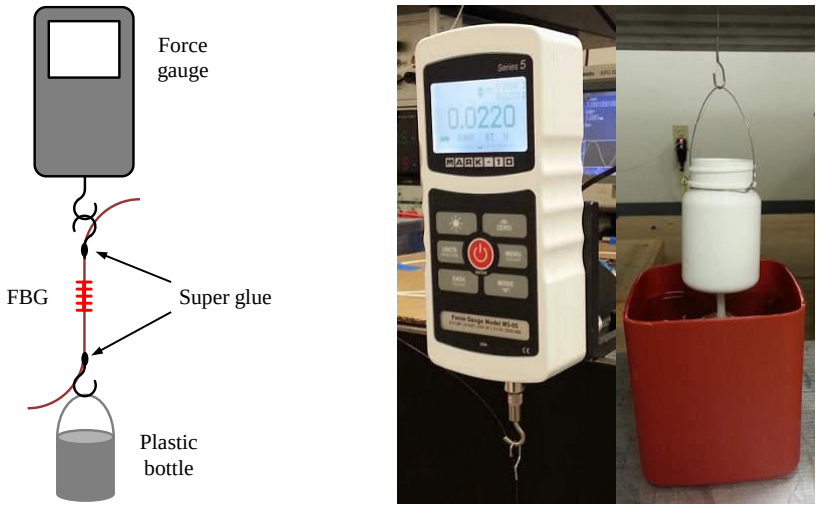

(a) Scheme of strain test (b) Real setup of strain test

Figure 3-9 Setup for static strain test

To reduce the influence of the temperature of the environment, the dispersive unit was placed in a box stuffed with plastic wraps and then placed in a relatively isolated area under the optical table. Also, since the strain was applied to only one of the FBGs, the other one could act as a reference to eliminate the influence of the environment.

The force gauge measured the force applied to the FBG. Knowing the force, cladding radius of the fiber and Young's modulus of silica, strain could be calculated using the following expression:

$$\varepsilon = \frac{F}{\pi a^2 Y} \tag{3.11}$$

where F is the force measured by the force gauge, a is the radius of the fiber cladding, and Y is the Young's modulus of silica. The fiber used for FBG inscription was Corning SMF28 and its radius is of 62.5μm. Young's modulus of silica is 73.1GPa. The

resolution of the force gauge was 0.0005N, so the resolution of measured strain was 0.56με.

Prior to the strain response measurement, a two-step measurement was carried to get the strain coefficient of the FBG and a more accurate total dispersion of the DCFs. The strain to delay conversion factor is the product of the strain coefficient of the FBG and the dispersion of the dispersive unit.

3.2.1.1 Strain coefficient of the FBG

The strain coefficient of the FBG was measured by monitoring the reflecting spectrum of the FBG while changing the applied strain using the setup described in Figure 3-9(a). The spectrum of the FBG was measured using Micron Optics static optical sensing interrogator (SM125). As the strain was increased by adding weights to the plastic bottle, the measured reflecting spectrum of the FBG also shifted accordingly, as shown Figure 3-10.

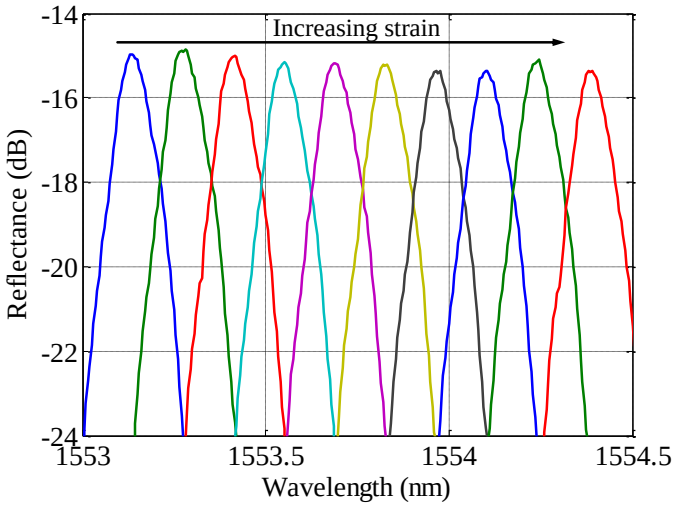

Figure 3-10 FBG reflecting spectrum shift as response to strain

Three measurements were carried out to find out the dependence of the FBG reflecting wavelength on the strain, and the results are plotted in Figure 3-11. The results show excellent repeatability and linearity, with difference of about 0.1% between the three measurements. The averaged strain coefficient is determined to be about 1.23pm/με. This

dependence is expected because the strain stretches the fiber, which in turn increases the effective period of the FBG so the reflecting peak wavelength increases.

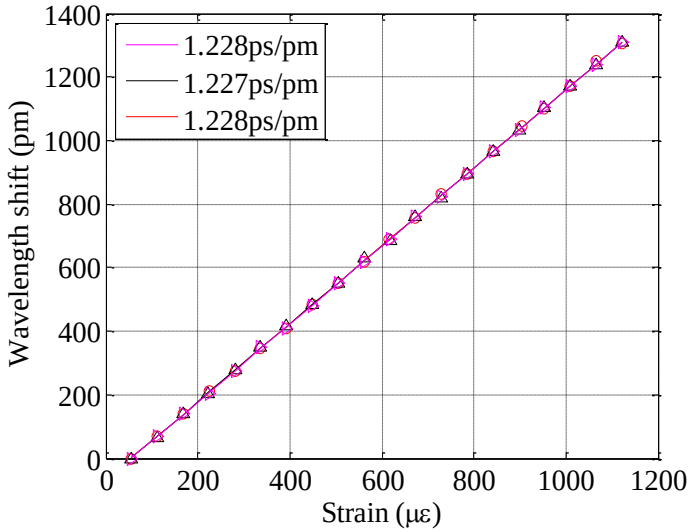

Figure 3-11 Strain coefficient of FBG. Markers: raw data points. Solid lines: linear fitted curve.

3.2.1.2 Measurement of dispersion

The dispersion of the dispersive unit could also be measured by monitoring the delay between the two pulses from the same FBG as the wavelength of the FBG is changed by the strain. The reflecting wavelength of the FBG was also measured using the sm125 so the relation between the wavelength of the pulse and the delay introduced by the dispersive unit can be calculated.

Three measurements were carried out to confirm the repeatability. At each wavelength, the delay was calculated 50 times and the average value was used to find the dependence. In these measurements, the environment was expected to have varied to some degree, which, according to the analysis in Section 3.1.3, will introduce unintended delay variation. Fortunately, FBG_2 was not applied with any strain, so the delay between the two pulses generated by the FBG_2 was purely dependent on the environment. Subtracting the delay calculated from FBG_2's pulses from that from FBG_1, the influence of the environment could be effectively eliminated.

The dependence of the delay on the wavelength, which is the dispersion of the dispersive unit, is plotted in Figure 3-12. The results again show good linearity and repeatability. The average dispersion from the three measurements is -2,743ps/nm, which is quite close to the estimated value, -2,793ps/nm, as given in Section 3.1.3.

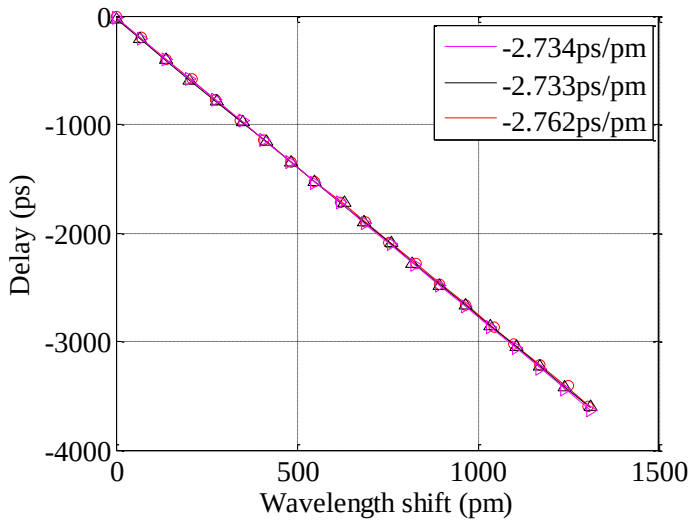

Figure 3-12 Dispersion of the M-Z structure

3.2.2 Static response

Since it has already been demonstrated that reflecting wavelength of the FBG is linearly dependent on the strain applied to it, and the delay between the pulses from different arms is linear to the wavelength of the pulses, it is natural to assume that the delay will be linearly dependent on the strain applied to the FBG.

Figure 3-13 shows the detected pulses with and without strain applied to FBG_1 with sampling rate of 40GS/s. Two traces are plotted, with the solid line as the signal when the applied strain was zero and the dashed line as the signal received when strain of 1,066.8με was applied. There are four pulses in each of the traces, marked as $pulse_1$, $pulse_2$, $pulse_3$ and $pulse_4$ in the figure. Of the four pulses, $pulse_1$ and $pulse_2$ passed from the arm with SMF28, while $pulse_3$ and $pulse_4$ passed through the arm with DCF. The arm with SMF28 was 12m shorter than the arm with DCF so the two sets of pulses are

displaced by about 60ns. Pulse$_1$ and pulse$_3$ were reflected by FBG$_1$ and the other two were reflected by FBG$_2$.

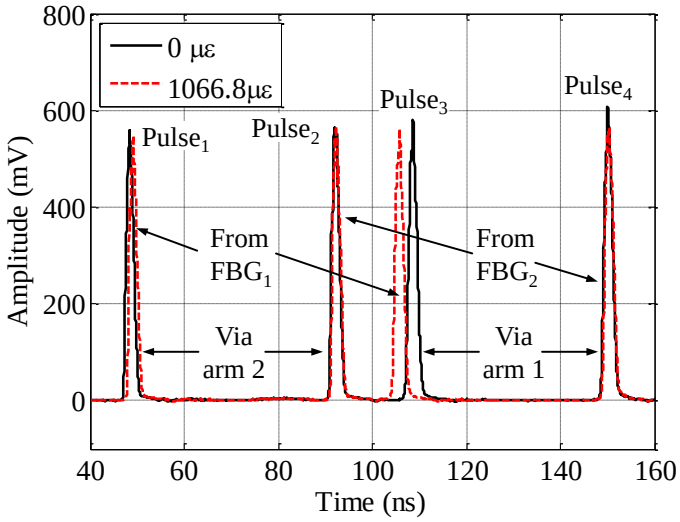

Figure 3-13 Received pulse in time domain with and without strain applied

It is noticed that in Figure 3-13, pulse$_3$ arrived earlier when the strain was applied while pulse$_1$ arrived slightly later. This is because the DCF had negative dispersion, which means the light travels faster for a longer wavelength, and the case is opposite for the Corning SMF28. And this explains why using SMF28 in Arm$_2$ increases the total dispersion of the dispersive unit.

The relation between the delay and the strain is plotted in Figure 3-14, which was obtained using the supercontinuum based light source. 50 sets of data were collected at each strain and the average delay was used for the final curve fitting. The experiment was repeated 4 times to verify that this characteristic was consistent. Figure 3-14(a) gives the results when the influence of the environment was not eliminated, that is, the delay calculated from the pulses from FBG$_1$ was considered only under the influence of the strain. However, it was not the case because the room temperature changed during the measurements, which had an impact on both of the FBGs and the dispersive unit. As a result, it is unavoidable that the curves have different slopes in different measurements.

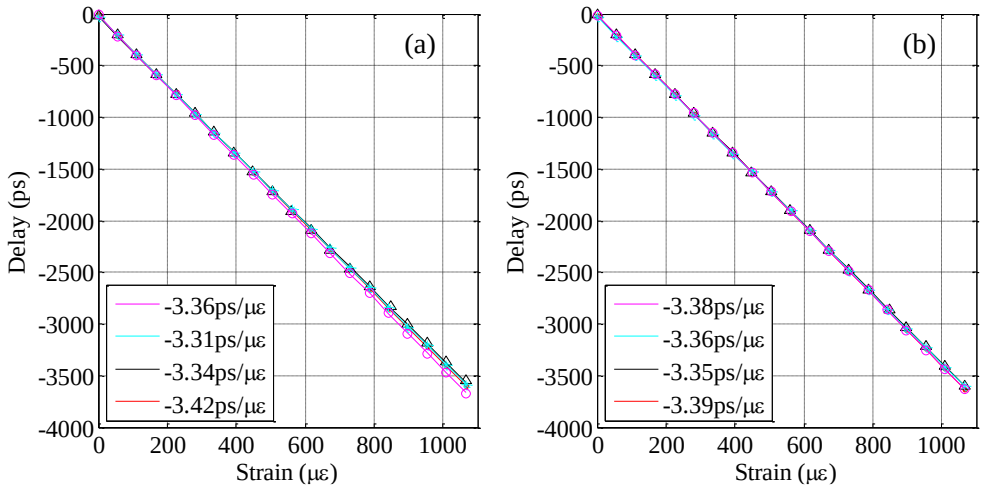

Figure 3-14 Strain response using SLD based source without reference

In the meantime, FBG_2 was placed in the same environment and the only difference between the two FBGs was that FBG_1 was applied with strain. So the delay calculated from the pulses from FBG_2, τ_2, reflects the influence of the environment. Subtracting τ_2 from the delay calculated from FBG_1, τ_1, will give the result that in theory only dependent on the strain, and the results are plotted in Figure 3-14(b). Comparing the two sets of curve, it is obvious that using FBG_2 as a compensation significantly improves the repeatability of the slope, reducing the difference of the four slopes from 3.3% to 0.9%. This slope is the strain-to-delay conversion factor, or 'conversion factor'.

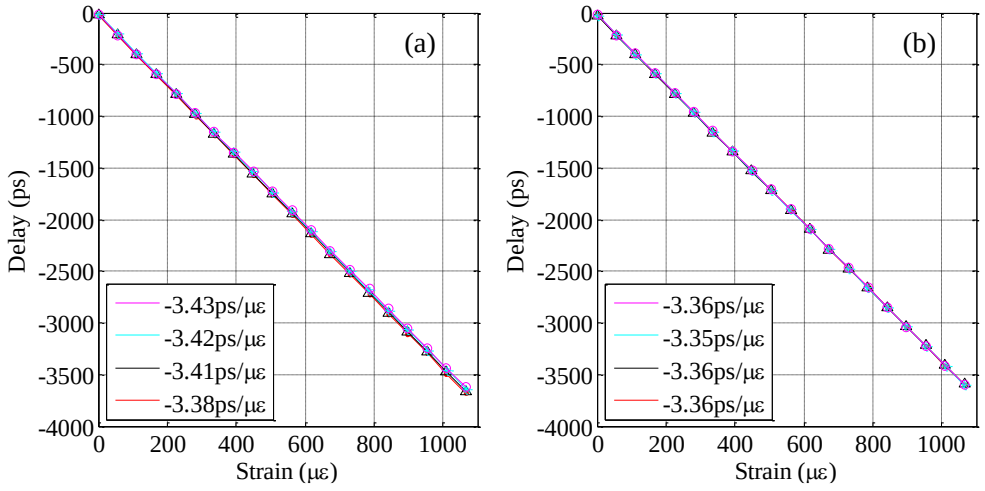

Figure 3-15 Strain response using SC based source without reference

Same experiment was repeated using the SLD based light source illustrated in Figure 3-2, and the results are plotted in Figure 3-15. Similar to the results when the supercontinuum based light source was used, the strain response is linear and the repeatability of the slope is improved using FBG_2 as the reference. The variation of the conversion factor is reduced from 1.5% to 0.3%.

The average conversion factor from the 8 measurements is -3.36ps/με, and it is expected to be the product of the strain coefficient and the dispersion, which is -3.37ps/με. The small difference between the two values comes from the calculations.

3.2.3 Dynamic response

To demonstrate that this system is capable of high speed sensing, an experiment was designed to apply a dynamic strain to an FBG. The system and the setup are illustrated in Figure 3-16. The supercontinuum based light source is used here, and the rest of the setup is the same as described in Figure 2-1.

The dynamic strain was applied to FBG_1 by attaching it to a piezoelectric transducer (PZT) cylinder using super glue. The PZT has inner diameter of 31.45mm, outer diameter of 38.45mn and height of 38.1mm, as it is shown in the inset of Figure 3-16.

Driving the PZT was a high voltage sinusoidal signal, which was generated by amplifying the sinusoidal output of an arbitrary function generator (Tektronix AFG 3252) using a wideband amplifier (Krohn-Hite model 7602). The thickness of the PZT changes with the voltage applied to it, so its outer diameter follows the voltage. Because the FBG was fixed on the outer surface of the PZT, it was stretched accordingly, experiencing a sinusoidal dynamic strain.

The signal was captured at 40GS/s by the oscilloscope in a mode in which data were saved once every three triggers. Since the supercontinuum light source had frequency of 21kHz, the equivalent sensing speed was 7kHz. This value is far less than the maximum frequency allowed, which is 6.25MHz for this setup. The speed is limited here by the non-adjustable repetition rate of the supercontinuum light source.

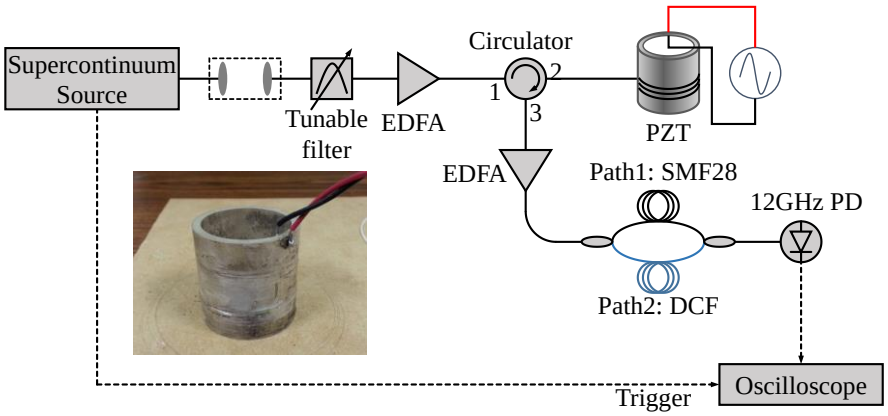

Figure 3-16 Setup for dynamic strain response mesurement

The response of the two FBGs is plotted in Figure 3-17. The results are given in strain and the DC component has been subtracted for easier comparison. FBG_1, which was attached to the PZT driven by the sinusoidal signal, had strain fluctuation and it resembled the waveform of the sinusoidal wave. In contrast, FBG_2 was stable as it was free of strain. This experiment demonstrates that the system is capable of high speed detection of dynamic strain. This could easily be extended to other measurands that can alter the reflecting wavelength of FBGs. Meanwhile, with calibration, the system is also capable of measuring the absolute value of the measurands. Theoretically it does not have low frequency limit and the high limit is determined by the sensing range, as it has been discussed in Section 2.2.2.

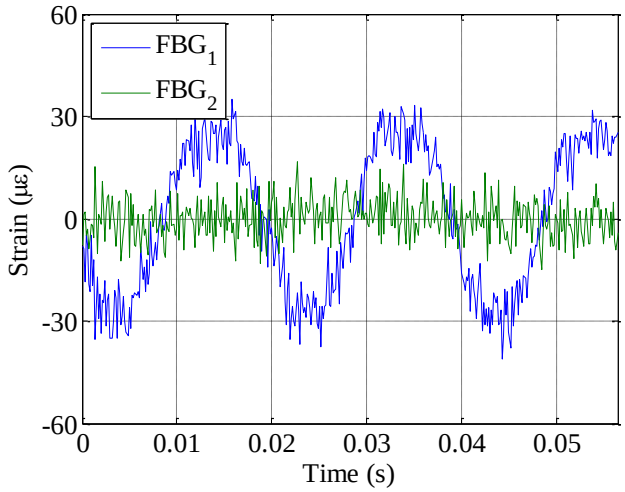

Figure 3-17 Dynamic response of the two FBGs

The responses to signals with different strengths were also measured, as plotted in Figure 3-18. Three curves in red, blue and green are the measured strain when the peak-to-peak voltage applied to the PZT was 140V, 120V and 100V, respectively. The black curves are the fitted sinusoidal wave. The fitted results show that the peak delay is dependent on the voltage, however they are not exactly proportional, this could be due to the nonlinear response of the PZT to the relatively high voltages.

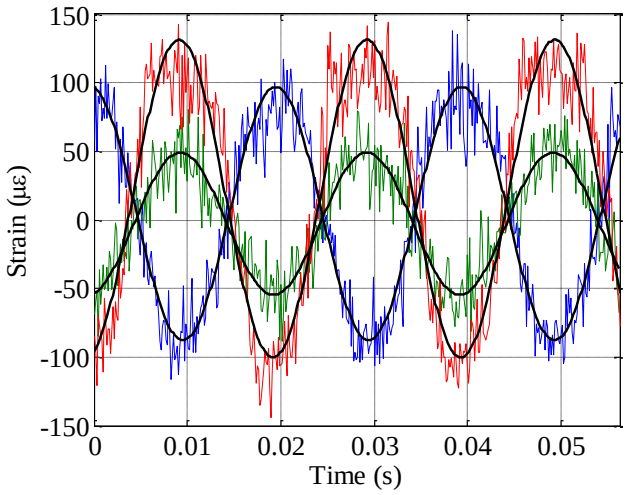

Figure 3-18 Dynamic response from FBG_1 with different voltage was applied. Red-140Vpp, blue-120Vpp, green-100Vpp, black-fitted curves

Another experiment was carried out to evaluate the effectiveness of enhancing the resolution by data average. 400 sets of data were captured in two different ways. One strain response was demodulated using the raw data taken, and it is plotted as the black curve in Figure 3-19. To compare, the data were also averaged 10 times and then demodulated using the same algorithm, and the corresponding result is also plotted in Figure 3-19 as the red curve. It is noted that the quality of the signal is significantly improved by averaging, and it is predictable because averaging enhances the SNR and previous simulation results show that the standard deviation of the demodulated delay decreases exponentially as the SNR increases,

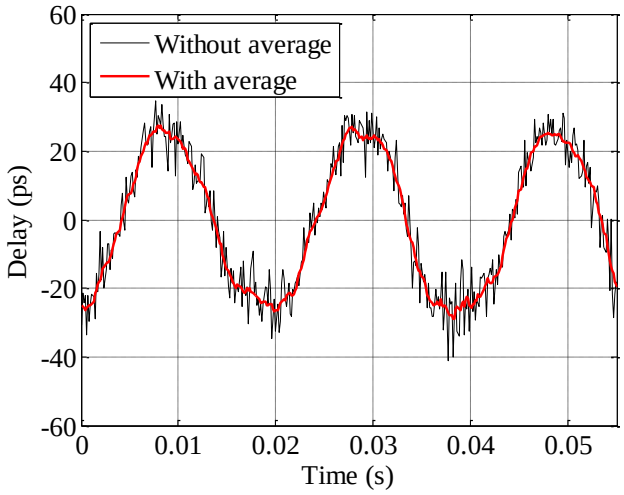

Figure 3-19 Dynaic response with and without 10 times of averaging

3.2.4 Averaging and noise filtering

While the delay-strain coefficient shows how sensitive the system can be in response to variation of strain, or more generally, the variation of the reflecting wavelength of the FBGs. In the sensing link, the standard deviation of the delays obtained under the same condition give the resolution of the measured strain, so it is necessary to investigate the standard deviation and find out how it could be improved.

Previous simulations show that the most influential factor on the performance is the SNR of the received signal. The SNR could be improved by optimizing multiple parameters of the system, for example, by increasing the power of the injected pulse to the sensing link, by replacing the EDFAs in the system with ones with lower noise, or by reducing the bandwidth of the photodetector to reduce the high frequency electrical noise. Meanwhile, there is one effective way to achieve a higher SNR which is data averaging.

Figure 3-20 shows the dependence of the standard deviation of the delay on the number of averaging. Each standard deviation was calculated from 50 measurements while the corresponding FBG was applied with a stable strain.

As it is expected, averaging can significantly reduce the standard deviation. However for both of the light sources, when the number of averaging is greater than 40, the

improvement is not obvious anymore. With 10 times of averaging, the standard deviation measured using supercontinuum based light source reduces from 18.23ps to 3.86ps, which corresponds to strain resolution improvement from 5.43με to 1.15με. For the SLD based light source, the strain resolution improvement was also significant, from 10.54με to 3.28με. This explains why the sinusoidal wave becomes much clearer after averaging in Figure 3-19.

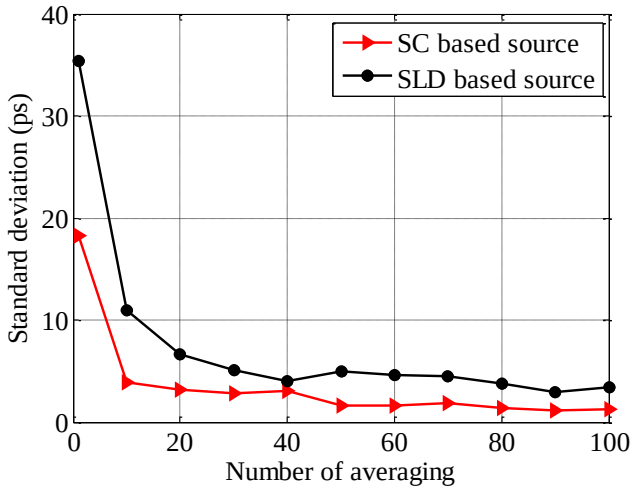

Figure 3-20 Dependence of the standard deviation of the delay on averaging using different light sources

Though averaging provides obvious benefit, it has the drawback of reducing the bandwidth of the detection and/or the sensing speed, depending on in which way the data is averaged. So the number of averaging applied should be decided based on the requirement of the bandwidth of the system and the intended sensing speed.

Another desirable improvement would be to using lower sampling speed to capture the pulse. Although a sampling rate of 40GS/s is achievable using a high speed oscilloscope, it is a requirement that is too high for commercial analog to digital converters, which could work at several Giga samples per second. Simulations show larger sampling interval will increase the standard deviation of the delay, and the result of the experiment provides the same conclusion, as Figure 3-21 shows. Figure 3-21(a) plots the comparison between the standard deviation with sampling rate of 40GS/s and 2.5GS/s when the bandwidth of the oscilloscope was set to 2.5GHz. Without averaging, the standard deviation increases from 17.35ps to67.59ps. Though averaging helps reduce the value,

the results obtained using sampling rate of 2.5GS/s is always 3 to 4 times of the value obtained with sampling rate of 40GS/s.

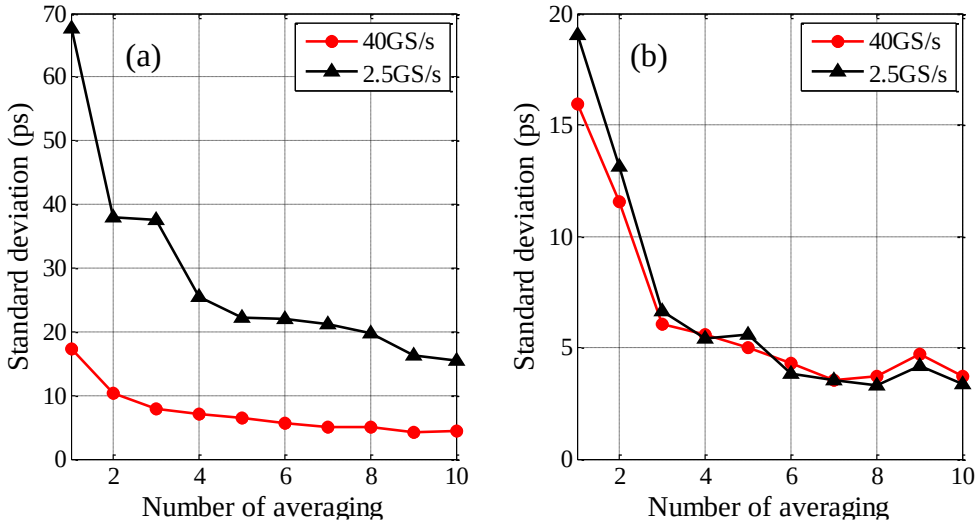

Figure 3-21 Standard deviation of the delay with sampling rate of 40GS/s and 2.5GS/s. (a) Detection bandwidth of 2GHz (b) detection bandwidth of 320MHz.

However, there is another way to improve the performance even when the sampling rate is reduced, which is to apply a noise filter. This was achieved by reducing the bandwidth of the oscilloscope in this experiment. The results are plotted in Figure 3-21(b). When the bandwidth was reduced from 2.5GHz to 320MHz, the standard deviation obtained using the sampling rate of 2.5GS/s is significantly reduced, and with 3 times of averaging, it could further be reduced to the same level as the case when 40GS/s sampling rate was used.

Chapter 4 Sensing with UW-FBG array

4.1 Modification to the light source

In the proof-of-concept demonstration, two light sources were tested and both of them had drawbacks. The SLD based light source had more flexibly of the pulses width and repetition rate, but had low output power due to the limited spectral power density of the SLD and the insertion loss of the EOM. Although an additional EDFA could be added to boost the output power of the light source, the quality of the light would be compromised as the ASE noise accumulated. The supercontinuum based light source had higher output power but still not sufficient for the demodulation of UW-FBGs, not to mention the non-adjustable pulse width and repetition rate.

The modified light source is shown in Figure 4-1. The same SLD was used, except that the EOM was replaced with an SOA based high-speed optical shutter, which will be called SOA or optical shutter hereafter. The SOA had rising and fall edges of 1ns each. Comparing with the EOM, the shutter offers two advantages. First, instead of introducing insertion loss, it offers a gain because it was originally designed to amplify light. The small signal gain of the SOA was 13dB, comparing with the 5dB insertion loss of the EOM, the total loss could be reduced by 18dB. Second, it offers a higher extinction ratio. A typical EOM has an extinction ratio of around 20dB, and it is significantly dependent on the bias voltage, which could drift and reduce the extinction ratio further. The SOA provides an extinction ratio of 60dB, which is a 40dB improvement. The extinction ratio of the light source may not be important when only few FBGs are involved, but it becomes crucial when the number of FBG is large. When the extinction ratio is low, the leaked light, which is a continuous wave, will be continuously reflected by the FBGs. The reflected CW light will accumulate and eventually be high enough to be comparable to the peak power of the reflected pulses by the FBGs. Although the pulses are still distinguishable, this unwanted continuous light wave can consume the majority of the gain of $EDFA_2$ and saturates the photodetectors.

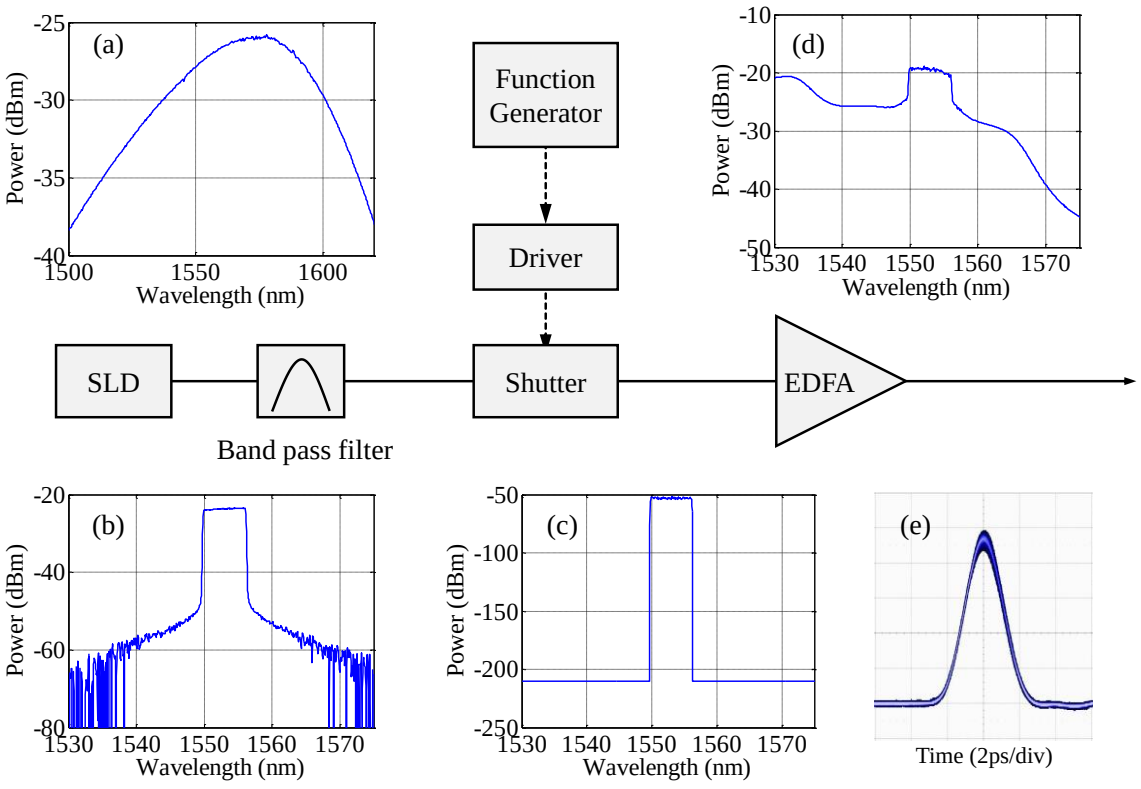

Figure 4-1 The modified light source using SOA based high-speed shutter (a) Spectrum of the SLD (b) Spectrum after bandpass filter (c) spectrum after the shutter (d) spectrum after EDFA (e) pulse shape after EDFA

The rest of the light source is the same as the previous SLD based design, only that the bandwidth of the bandpass filer was reduced to 6nm from 8nm. This could still offer sufficient sensing capability. For example, assuming FBGs have a thermal coefficient of 11pm/^{o}C, this allows a temperature detection range of more than 540 ^{o}C.

The spectrum of the SLD is plotted in inset (a) of Figure 4-1, and the total power at this point was 11.5dBm. The bandpass filter reduced the power to about -2.8dBm due to bandwidth reduction and the insertion loss of the filter. The spectrum of the light after the bandpass filter is shown in inset (b). At the output of the filter, the optical signal to noise ratio was higher than 30dB.

This filtered continuous light was then chopped to pulses by the shutter, which was driven by a high speed pulse generator (AVNET Model AVI-V-2L-P-VTA). The output pulses had a temporal width of 2ns and repetition rate of 20kHz. The repetition rate was

tunable in the range of 1kHz and 100kHz, and the pulse width could also be any value between 1ns and 20ns. Inset (c) in Figure 4-1 shows the spectrum of the light at the output of the shutter. Due to the extremely low duty cycle, which was about 0.0004%, the average power at the output of the shutter was as low as -34dBm. Figure 4-2 shows the pulse at the output of the shutter measured by the APD whose bandwidth was 200MHz. Inset (e) in Figure 4-1 is the pulse measured in persistent mode using the oscilloscope, the actual SNR of the optical signal was better than that shown in the figure because a large portion of the noise was from the APD.

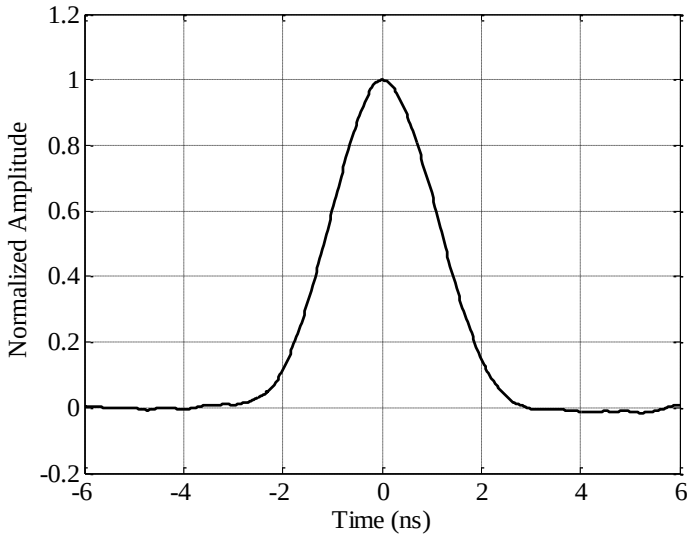

Figure 4-2 Pulse measured by the APD at the output of the optical shutter

The EDFA which followed the shutter amplified the mean power to 3.7dBm, which is a very high power considering the extremely low duty cycle. However, because the input power to the EDFA was extremely low, a large portion of the output power was ASE noise which did not belong to the pulse. Inset (d) of Figure 4-1 shows the spectrum of pulses at the output of the EDFA. It shows that due to the large portion of the ASE noise, the OSNR was reduced to about 6dB. Using a photodetector with a known conversion gain, the actual peak power was estimated to be about 33dBm.

4.2 Sensing with UW-FBG array

With the modified light source, a sensing link consisting of a large amount of UW-FBGs can now be measured. The results will be discussed in detail in the following sections.

4.2.1 System setup

A complete sensing system is illustrated in Figure 4-3, of which the light source and the dispersive unit have already been described in detail in the previous sections. Here the dispersive unit had the branch structure. The sensing link consists of 2,014 UW-FBGs with spacing of 1m and reflectance of about -35dB. These UW-FBGs were inscribed in the fiber drawing process using the method discussed in [62].

Inset (a) in Figure 4-3 shows the spectrum of light at port 3 of the circulator, which is the combination of the contribution of all the FBGs in the sensing link. It shows that the FBGs have wavelength around 1552.5nm. Comparing with inset (d) in Figure 4-4, the OSNR has significant improvement, and this is because the FBGs filtered out the majority of the ASE noise introduced by $EDFA_1$. The reflected signal was then amplified by $EDFA_2$ before it was sent to the dispersive unit. Inset (b) shows the spectrum of the amplified signal. Comparing the spectrum of signal before and after the amplification, it could be figured out that the gain was around 10dB.

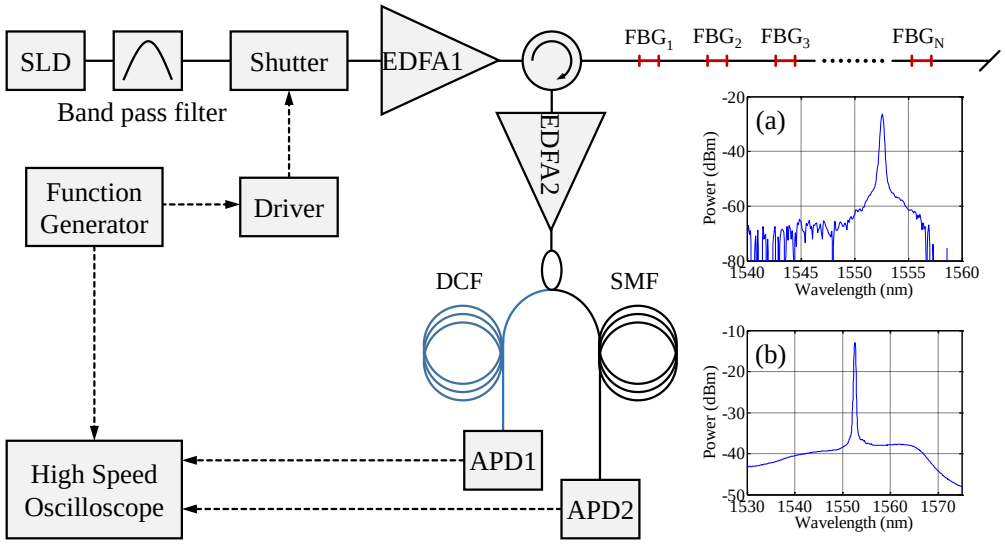

Figure 4-3 Sensing system for detecting large number of UW-FBGs

The detected signal was sent to a high speed oscilloscope (LeCroy Zi725), which was triggered by the same clock as that for the pulsed driver for high speed shutter. The oscilloscope saved the data at each trigger and the saved data were later processed using the algorithm proposed in Section 2.3.

The linewidth of the reflected pulses is determined by the bandwidth of the FBGs, which is about 0.1nm. Given the large dispersion, the pulse could be broadened and this could influence the performance of the system according to the previous simulation.

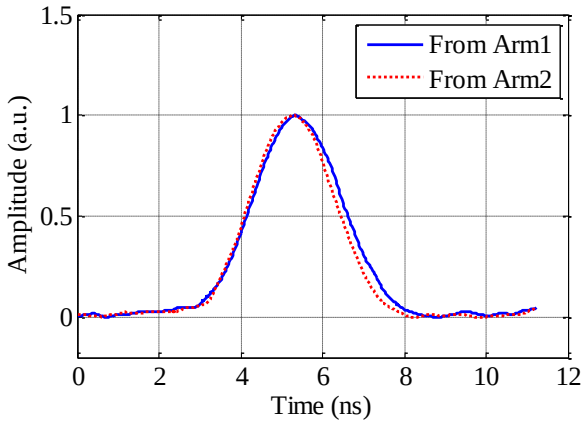

Figure 4-4. Comparison of the pulse from the two arms

Knowing the dispersion of the DCF in the system and the bandwidth of the FBG, the pulse broadening could be calculated. In the dispersive unit, the DCF had dispersion of -2,387ps/nm and the SMF had dispersion of about 396ps/nm, assuming the initial pulse was not chirped, the maximum pulse broadening was predicted to be about 0.24ns and the temporal width difference between the two pulses from the two arms was estimated to be about 0.2ns. Figure 4-4 compares the two pulses from the two arms, and the width difference was about 0.13ns, which according to the simulation, has insignificant influence on the performance of the system.

The wavelength distribution of the FBGs in the sensing link was measured by an FBG interrogator (Sentek Instrument LLC Model LG1-100B), which had a wavelength resolution of 7pm, is plotted in Figure 4-5. In this figure, the mean wavelength of the entire sensing link was subtracted. It is noticed that the wavelengths of the UW-FBGs

had some variations, which were from the FBG inscribing process and the additional strain when the optical fiber was wound on the spool.

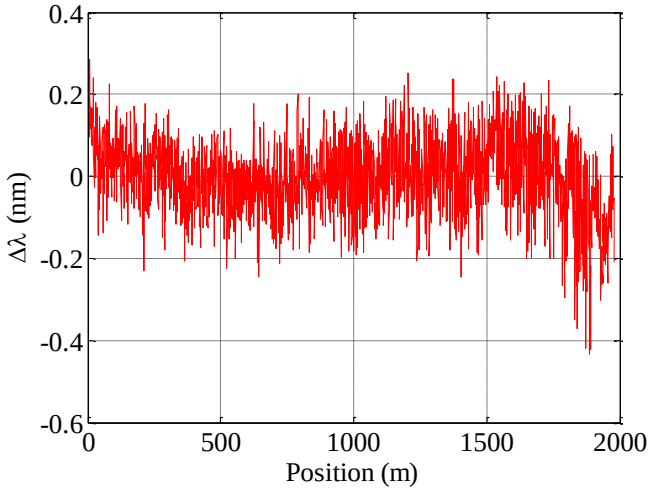

Figure 4-5 Wavelength distribute of the FBG in the sensing link

Figure 4-6 provides a typical reflecting spectrum of the FBGs, which shows that the 3dB bandwidth of the FBG was about 0.1nm and the reflectance was around -35dB. There was non-uniformity of the reflectance as well, but it was in the range of +/- 3dB range.

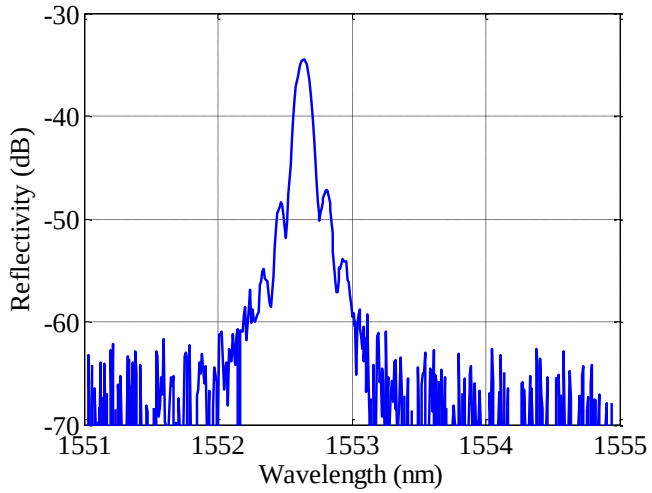

Figure 4-6 Typical spectrum of FBGs

As discussed before, when a large number of gratings with nearly the same wavelength are multiplexed in one sensing link, power could be depleted if the total number or the

reflectance is too high. Also, crosstalk could happen due to the multiple reflections between the FBGs in the sensing link. According to the previous analysis in Section 2.4, for this sensing link, the maximum power difference is expected to be about 7.2dB and the crosstalk is estimated to be -7dB. Both numbers are in an acceptable range although it would be better if the FBGs were weaker.

However for the actual sensing link, the FBGs were not exactly identical. The previously estimated crosstalk could be considered to be the worst case so the influence of the crosstalk is a lesser concern. The 7.2dB power difference will not make the weakest FBG undetectable, but it will have observable influence on the performance because it will reduce the SNR of the pulses from the farther end of the sensing link.

4.2.2 Performance of the system

4.2.2.1 Static response

Pulses reflected by a randomly picked grating located at the center range was used to evaluate the performance of the system under different conditions.

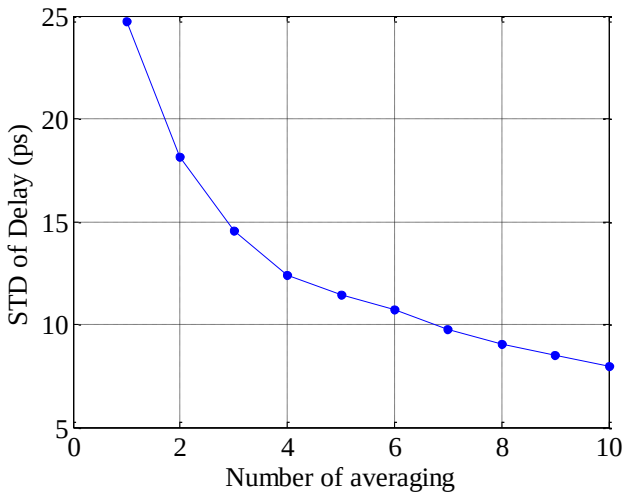

Figure 4-7 STD versus number of averaging

Figure 4-7 gives the standard deviation of the delay versus the number of data averaging with a sampling interval of 25ps. Without averaging, the standard deviation of delay is calculated to be 24.7ps, which corresponds to a static strain resolution of 7.35με because

the previously measured conversion factor was -3.36ps/με. As it has been proved before, an increased number of averaging helps reduce the standard deviation. With 10 times of averaging, the standard deviation of the delay is reduced to 7.94ps, corresponding to a static strain resolution of 2.36με.

Reducing the sampling rate is also desirable because it will reduce the system cost and the work load of data processing, and will make the system more practical. The curve in Figure 4-8 shows that standard deviation of the delay has tendency to increase as the sampling interval increases, but the relation cannot be described as being linear or deterministic. This is because the received signal has a very low SNR due to the multiple stages of amplifications each of which introduces extra noise, and the electrical noise. Without averaging and with sampling interval of 375ps, standard deviation of delay is 27.92ps, which corresponds to static strain resolution of 8.29με. However, it is noticed that the standard deviation does not increase significantly as sampling interval increases, this maybe because the main factor which affects the performance is not the sampling interval but instead the signal to noise ratio.

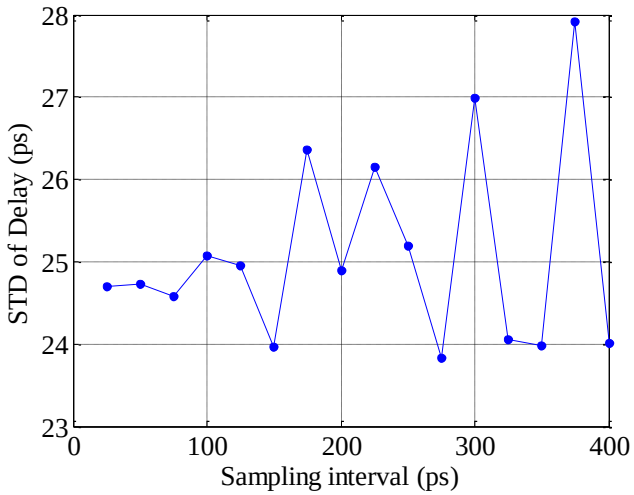

Figure 4-8 STD versus sampling interval

By recording all the reflected pulses from the two arms, a position dependent delay can be calculated. Divided by the measured total dispersion, the relative wavelength distribution of the sensing link can be obtained. The absolute wavelength can also be

obtained if one of the FBGs is used as a wavelength reference. The calculated relative wavelengths, with the average value subtracted, is plotted in Figure 4-9.

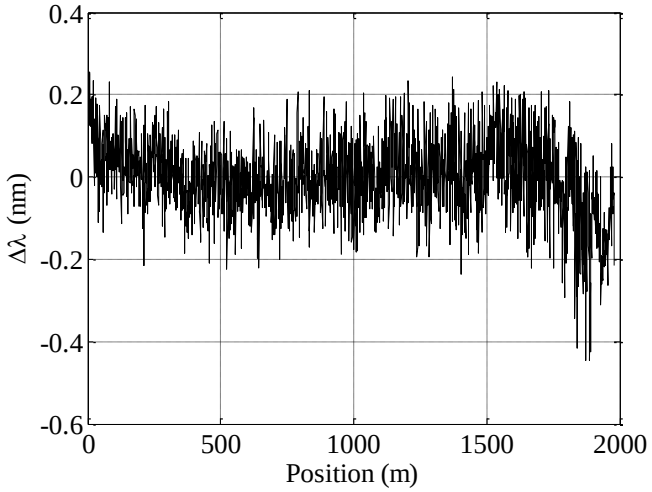

Figure 4-9 Relative wavelength distribution

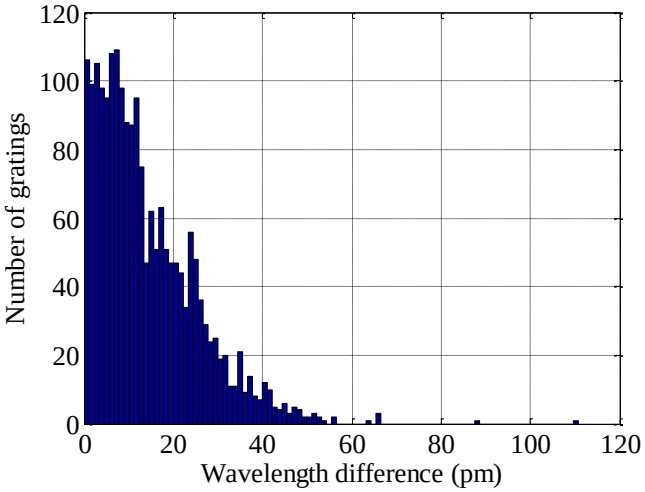

Figure 4-10 Wavelength error distribution

Comparison was made between the results in Figure 4-5 and the results from this sensing system. Figure 4-10 shows the distribution of the absolute wavelength difference obtained by subtracting the data in Figure 4-9 from those in Figure 4-5. Assuming the wavelength measured by the FBG interrogator was accurate, the horizontal axis of Figure 4-10 can be considered as a wavelength error. Statistics shows that though few gratings have a wavelength error as high as 0.1nm, 44.99% of the gratings have an error less than

10pm, and 73.78% of the results have an error less than 20pm. And if the error limit is lifted to 50pm, the ratio increases to 99.21%.

It is also desirable to know the standard deviation of the measured wavelengths of the UW-FBGs, as they determine the resolution of the sensing. 50 measurements were performed and the wavelength of each FBG was calculated. The wavelength standard deviation of each FBG was then calculated by dividing the standard deviation of the delay by the dispersion of the dispersive unit. The wavelength standard deviation is plotted against the position in Figure 4-11.

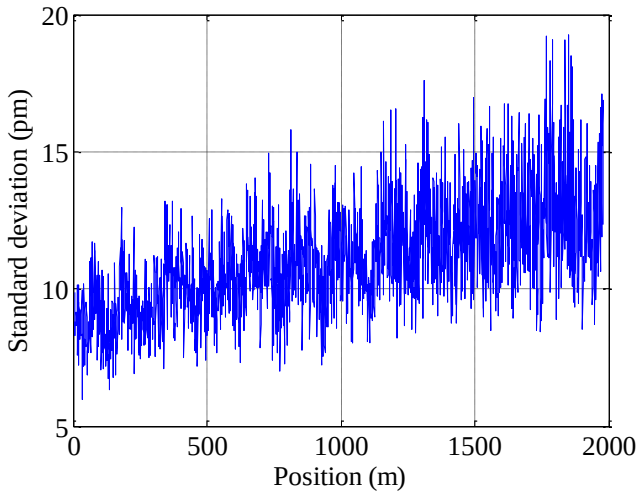

Figure 4-11 Standard deviation versus position

The curve shows that as the FBG becomes farther from the light source, the standard deviation becomes larger. This can originate from multiple causes. The first one may be the influence of the power depletion. As it has been discussed before, the pulses from the farther end get weaker due to the previous reflections as well as the fiber loss, resulting in a weaker signal strength and lower SNR. This effect is the most influential factor to the performance of the system and the standard deviation increases exponentially as the SNR reduces. The crosstalk is another possible factor, because the FBGs at the farther end experience greater crosstalk according to the previous analysis. Any instability of the FBGs before the target FBG will have a contribution to the result, so it is more likely that the measured wavelength has a larger standard deviation if it is farther away. However, it is less likely to be the main issue because the 50 sets of data were captured in a very short

period of time (2.5ms) during which neither temperature or strain is expected to have noticeable change.

To verify that the standard deviation of the wavelength is indeed influenced by the SNR which is directly related to the amplitude of the pulse. The standard deviation is plotted versus the pulse amplitude of the corresponding pulses in Figure 4-12. It is noted that the standard deviation of the measured wavelength reduces rapidly as the amplitude of the pulse increase, which is similar to the simulation results in Section 2.5.1. To verify this relation further, the standard deviation of the measured wavelength is plotted versus the signal to noise ratio in Figure 4-13, the similar dependence holds. So the conclusion is that the SNR is the main factor determining the performance in this case.

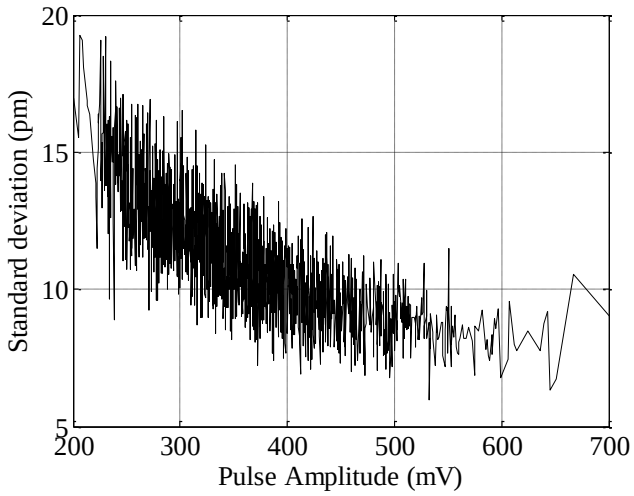

Figure 4-12 Standard deviation versus signal strength

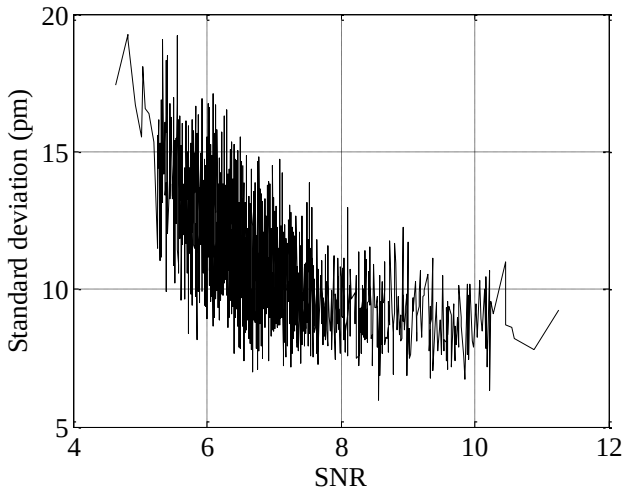

Figure 4-13 Standard deviation versus signal to noise ratio

The distribution of the wavelength standard deviation is given in Figure 4-14, which shows all of the values are less than 20pm and 95.83% of them are less than 15pm. The expected value is about 11pm, corresponding to the strain resolution of about 8.7με and temperature resolution less than 1^{o}C.

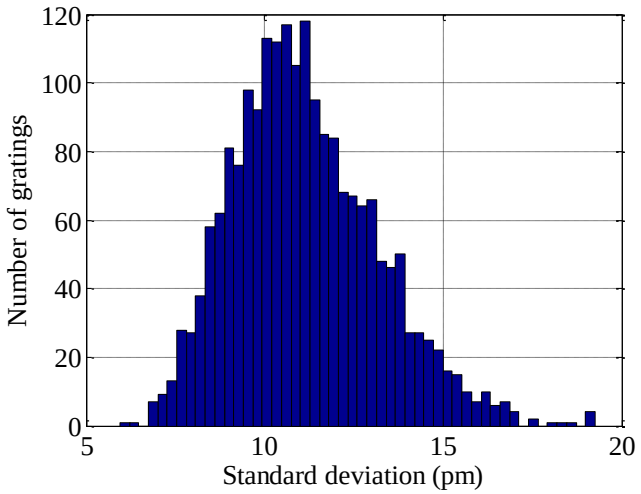

Figure 4-14 Wavelength standard deviation distribution of all gratings

4.2.2.2 Dynamic strain response

The dynamic response was also measured using the same setup in the proof-of-concept demonstration, except that the sinusoidal signal driving the PZT had a higher frequency

and the FBG attached to the PZT was the last one in the sensing link. Figure 4-15 shows the results obtained with a trigger frequency of 20kHz, sampling rate of 40GS/s and no averaging.

The peak to peak voltage was set to 130V when the frequency was 100Hz, and the frequency was then changed to 250Hz, 500Hz and 1kHz to demonstrate that the system's capability of measuring high speed signal. Higher frequency was not applied as the output from the high voltage amplifier became unstable. For each case, the spectral density was also calculated and both the time domain response and its spectral density are plotted in Figure 4-15. The results are converted to strain in the figure.

It is noticed that for all the cases, higher order harmonics exist. This could be caused either by the sinusoidal wave driving the PZT or the nonlinear response of the PZT. However, the periodical signal is easily identified in the time domain. If the harmonics are ignored, the noise level is always lower than $0.3\mu\varepsilon/\sqrt{Hz}$.

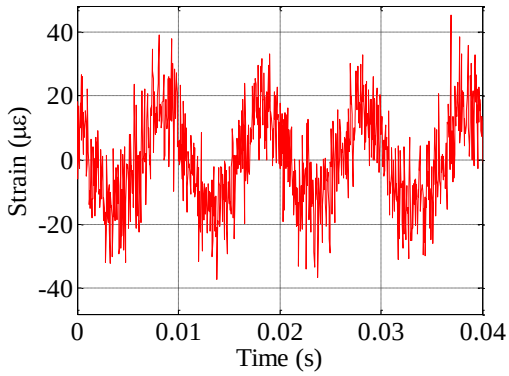

(a)Time domain response of 100Hz signal

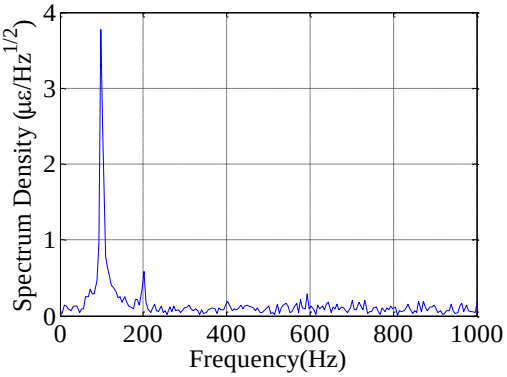

(b)Spectral density of the 100Hz signal

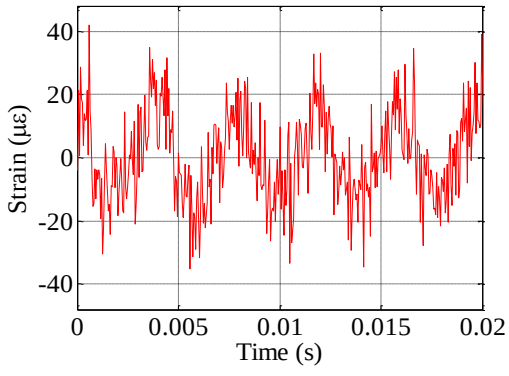

(c) Time domain response of 250Hz signal

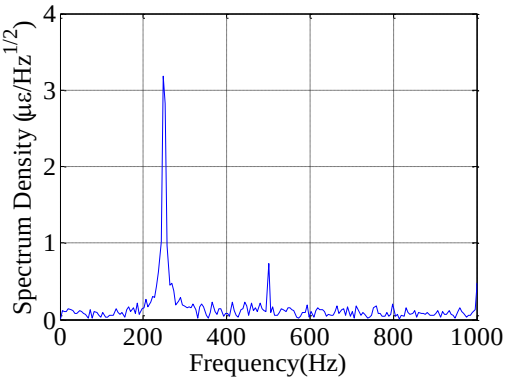

(d)Spectral density of the 250Hz signal

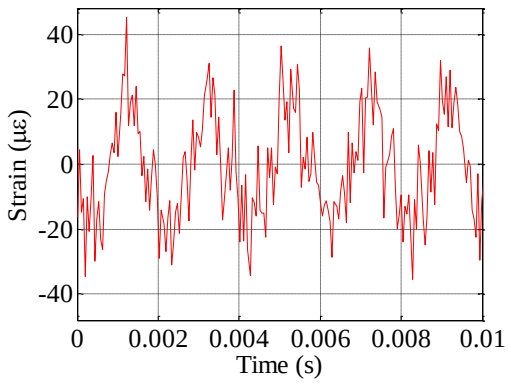

(e) Time domain response of 500Hz signal

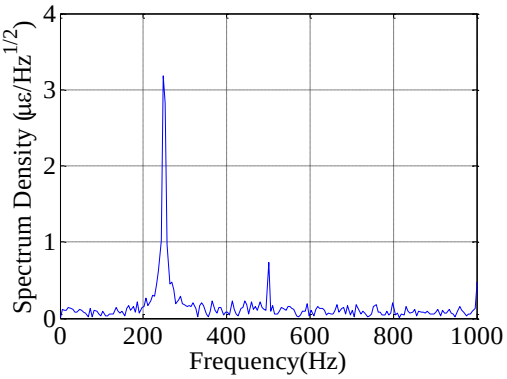

(f) Spectral density of the 500Hz signal

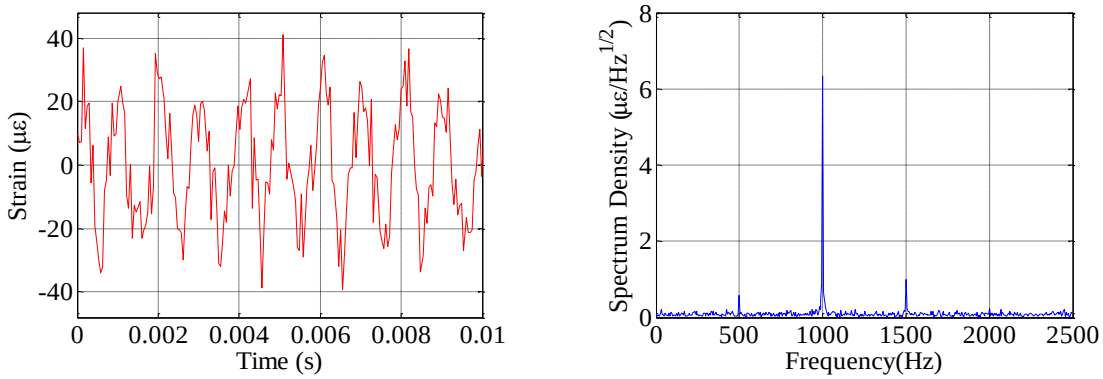

(g) Time domain response of 1kHz signal

(h) Spectral density of the 1kHz signal

Figure 4-15 Dynamic strain response with signal of different frequencies

4.3 Noise analysis

As it has been analyzed before, the signal to noise ratio is the most influential factor to the performance of the system, and the resolution improves exponentially as the SNR increases. It is thus important to find out the factors that contribute to the noise of the system and subsequently the findings will provide a clear path to further improve the performance of the system in the future.

4.3.1 Relative intensity noise

First noise source coming into the picture is the relative intensity noise (RIN), which is the power fluctuation of the light source and has various origins. The light source used in the system is illustrated in Figure 4-16.

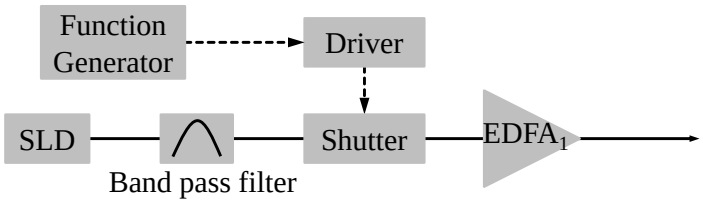

Figure 4-16 Light source for UW-FBG measurement

In the light source, the light originally comes from the SLD, which is an incoherent source and its RIN is usually higher than that of a quality laser diode. The SLD was then followed by an optical shutter and an EDFA, both of which will add additional noise. These additional noises will be discussed in Section 4.3.2.

A broadband incoherent light source, like the SLD, has relative intensity noise from three sources: shot noise, thermal noise and excess photon noise, and the excess photon noise is dominant for high power light sources [73]. The relative intensity noise is expressed as:

$$RIN = \left(\frac{\left\langle \Delta i_{th}^2 \right\rangle + \left\langle \Delta i_{sh}^2 \right\rangle + \left\langle \Delta i_{ex}^2 \right\rangle}{\left\langle I \right\rangle^2 \Delta f} \right) \tag{4.1}$$

in which $\left\langle \Delta i_{th}^2 \right\rangle$ is the thermal noise given by:

$$\left\langle \Delta i_{th}^2 \right\rangle = \frac{4k_B T \Delta f}{R_L} \tag{4.2}$$

where k_B is the Boltzmann constant, T is the temperature, Δf is the bandwidth of detection and R_L is the load resistance of the detector.

$\left\langle \Delta i_{sh}^2 \right\rangle$ is the shot noise is expressed by:

$$\left\langle \Delta i_{sh}^2 \right\rangle = 2q \left\langle I \right\rangle \Delta f \tag{4.3}$$

where q is the electron charge and $\left\langle I \right\rangle$ is the averaged current.

$\left\langle \Delta i_{ex}^2 \right\rangle$, which is the excess photon noise, is dependent on the polarization of the light, bandwidth of the detector and the linewidth of the light:

$$\left\langle \Delta i_{ex}^2 \right\rangle = \frac{\left(1+\alpha^2\right)\left\langle I \right\rangle^2 \Delta f}{\Delta \nu_{eff}} \tag{4.4}$$

where α is the degree of polarization and $\Delta\nu_{eff}$ is the effective linewidth. As Figure 4-17 shows, it decreases rapidly as linewidth increases.

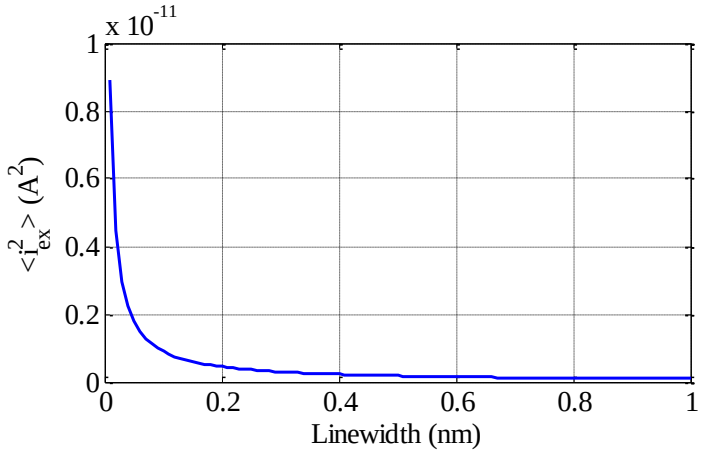

Figure 4-17. Dependence of excess photon noise on linewidth

Since for high power broadband sources the noise mainly comes from the excess photon noise, the RIN is expected to decrease as the bandwidth increases. And naturally for the purpose of lowering the noise level, a broader linewidth is more desirable. However, the amplification of the light pulse will be compromised if the bandwidth of the light is too wide because the total power will be distributed in a larger wavelength span. More importantly, the linewidth of the returned pulse is determined by the UW-FBGs, not the incident light, so ultimately it is not necessary to increase the bandwidth too much for the purpose of reducing the excess photon noise.

The bandwidth of an FBG should not be too large because pulse broadening will increase as the bandwidth becomes larger, which influences the resolution of the system. Also, fabrication of broadband FBGs takes more effort, thus increasing the cost.

The peak power of the pulse entering the circulator was measured to be 33dBm, and all the losses and gains of the components from the system are listed in Table 4-1. In Table 4-1, the loss introduced by the FBGs comes from two mechanisms: reflecting and

filtering. The FBG only reflects a small portion of the incident light, and this can be considered as a loss. The reflectance of the FBGs was around -35dB so loss from the reflecting was 35dB. Meanwhile, in the spectrum domain, the FBGs had a reflecting bandwidth of only 0.1nm when the bandwidth of the incident light was 6nm. The power in the wavelength range which is out of the FBG's reflecting band was lost, so this introduced another 17.8dB loss.

Table 4-1. Gain and loss of each element in the system using Mach-Zehnder structured dispersive unit

Device	Circulator	FBGs	Fiber	EDFA	Dispersive unit
Gain/Loss (dB)	-1.5	-35-17.8	-0.5	14	-19.3

Based on this table, the peak power of the pulses at the avalanche photodetectors (APDs) is calculated to be 2.08μW. The APD had responsivity of 0.85A/W and the current by 10 times, so the peak current was 1.77×10^{-5}A. Assuming the degree of polarization was 0.5 and linewidth of the reflected light was 0.1nm, the value of each type of noise can be estimated, as Table 4-2 shows. The excess photon noise is more than 3 orders of magnitude higher than the combination of the other two. So for the relative intensity noise, the excess photon noise is dominant.

Table 4-2. Estimation of intensity noise at the receiver

Noise	$\langle i_{th}^2 \rangle$	$\langle i_{sh}^2 \rangle$	$\langle i_{ex}^2 \rangle$
Current (A^2)	1.66×10^{-16}	1.13×10^{-15}	6.27×10^{-12}

4.3.2 Amplified spontaneous emission noise

Besides the relative intensity noise which is dependent on the light source and detection, optical amplifiers can also reduce the signal to noise ratio. This is because the amplifiers not only amplify the input light, which is the combination of signal and noise, but also add additional noise due to amplified spontaneous emission (ASE). This characteristic is given by the parameter, noise figure (NF) and it is defined as [74]:

$$NF[dB] = 10\log\left(SNR_{in} / SNR_{out}\right) \tag{4.5}$$

Haus discussed in detail in [74] how the noise figure of an optical amplifier should be defined to make it consistent with the IEEE standard: signal should not be defined as the square of the photon number because it is not a linear amplifier of photon number but rather the amplitude of the electromagnetic wave.

Two EDFAs were used in the system, $EDFA_1$ was in the light source, which followed the SOA to increase the peak power of the incident pulse to the sensing link. $EDFA_2$ was used just before the dispersive unit as a preamplifier. Both of them had noise figure of 5dB and the gains of $EDFA_1$ and $EDFA_2$ were 23dB and 14dB, respectively.

According to [74], the total noise figure of a pair of cascaded amplifiers is:

$$F = F_1 + \frac{F_2 - 1}{G_1} \tag{4.6}$$

where F_1 and F_2 are the noise figures of the two amplifiers, and G_1 is the gain of the first amplifier.

However, Equation 4.6 cannot be used because through the entire link there are multiple components, including the two EDFAs, the SOA and the sensing link, so the signal degradation is not solely caused by the two EDFAs.

The sensing link not only attenuates the optical power due to the low FBG reflectivity and the fiber loss, but also generates Rayleigh back scattering, which is another noise source. Additionally, the returned pulses have a much narrower bandwidth compared with that of the input pulse, so it has the ability of filtering out the ASE noise from the SOA and $EDFA_1$. The evaluation of sensing link's noise characteristics will be discussed in the next subsection.

4.3.3 Rayleigh backscattering

An incident pulse into a length of fiber is continuously scattered because of the irregular microscopic structures formed during the fiber fabrication process, and the scattering is called Rayleigh backscattering. And because the structures are not controllable and

random, the scattered light has fluctuations in the time domain, and in the case when the incident light is coherent, interference will occur, making the fluctuations larger

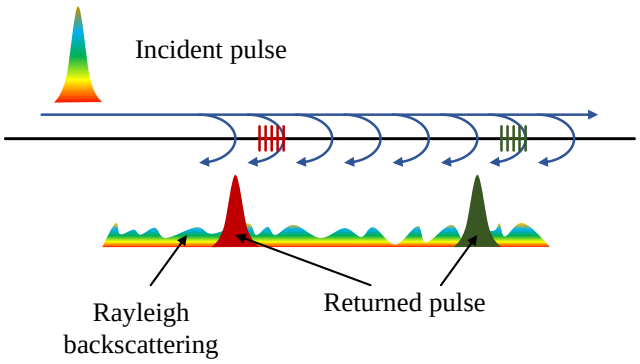

Figure 4-18. Noise from Rayleigh backscattering

Since the Rayleigh backscattering occurs all along the fiber, the signal, which is the reflected pulses by the FBGs, will overlap with the Rayleigh backscattering so additional noise is introduced to the signal and the SNR is reduced, as Figure 4-18 illustrates.

If the characteristics of the sensing link can also be described by a noise figure, it can be deduced for the given reflectivity of the FBGs and fiber's Rayleigh backscatter coefficient. Assuming the incident pulse has signal power of S_{in} and noise power of N_{in}, and the Rayleigh backscattering light is additive to the reflected pulse, the reflected light P_{out} will be:

$$P_{out} = R\cdot\left(S_{in} + N_{in}\right) + N_{ray} \tag{4.7}$$

where N_{ray} is the Rayleigh scattering, given by:

$$N_{ray} = r\cdot\left(S_{in} + N_{in}\right) \tag{4.8}$$

According to the definition of the noise figure, the noise figure of the sensing fiber, mostly determined by the Rayleigh scattering, is expressed as:

$$F_{sensor} = \frac{S_{in}}{N_{in}} \Big/ \frac{R \cdot S_{in}}{R \cdot N_{in} + N_{ray}} \tag{4.9}$$

Inserting Equation 4.8 into Equation 4.9, the noise figure becomes:

$$F_{sensor} = 1 + \frac{r}{R} \cdot \left(SNR_{in} + 1 \right) \tag{4.10}$$

This analysis is based on the assumption that the reflected light has the same bandwidth as the input light, which is not the case in the system. However, the majority of the noise in the incident light is from the excess photon noise and according to Equation 4.4, excess photon noise $\left\langle i_{ex}^2 \right\rangle$ is proportional to $\left\langle I \right\rangle^2 / \nu_{eff}$. When the bandwidth is reduced by N times due to the reflection of the grating, the power is reduced by the same amount, as is the generated current. So finally $\left\langle i_{ex}^2 \right\rangle$ is 1/N of the input value, and the input SNR increased by approximately $10 \cdot \log_{10} N$ (dB), which 17.8dB in this system.

The analysis above is based on the assumption that the noise is additive to the signal and no interference would occur. But if the light source is coherent, the interference effect should be taken into account.

When taking the interference into account, the added noise in the fiber is:

$$N_{ray} = r \cdot S_{in} + r \cdot N_{in} + \sqrt{\beta r} \cdot S_{in} \tag{4.11}$$

And the noise figure is modified to:

$$F_{sensor} = 1 + \frac{r}{R} \cdot \left(SNR_{in} + 1 \right) + \frac{\sqrt{\beta r}}{R} \cdot SNR_{in} \tag{4.12}$$

in which β is a weighting factor for the interference.

4.3.4 Quantization noise

The detected pulses are digitized by analog-to-digital converters (ADCs) before being used to calculate the delay. Because there is a limit to the number of bits in the quantization, the reconstructed pulse will not be exactly the same as it is in the analog form. The difference can is characterized as quantization noise and it is reflected by the effective number of bits (ENOB) of the ADCs.

In the system, the process of quantization was done by a digital oscilloscope which has a resolution of 8bits and ENOB of about 6bits. ENOB can be related to signal to noise ratio by:

$$SNR(dB) = 6.02 \cdot ENOB + 1.76 \tag{4.13}$$

For ENOB of 6bits, the SNR is 38.9dB.

Quantization noise should be taken into account when the input signal has similar or higher SNR, but if the input signal already has low SNR, the influence of the quantization noise can be ignored.

4.3.5 Measurement of the noise

The signal to noise ratio of the system can be measured at various stages, including at the outputs of the SLD, the SOA and $EDFA_1$. The pulse returned from the sensing link without amplification is too weak to be detected, so the next state is at the output of $EDFA_2$ or at the input of the APDs, which have small difference if a low noise detector is used to measure the signals.

To measure the SNR, a detector with low noise and conversion gain of -600V/W was used to detect the pulse, and the signal was then measured by the same oscilloscope used in the system. The bandwidth of the oscilloscope was set to be 200MHz, which was the same as the bandwidth of the APDs used in the experiments.

The output power of the SLD was attenuated to 1mW to make sure it was under the input power limit of the detector. The signal was detected to be 606mV and the noise was 2.6mV, giving a SNR of 23.6dB. At the output of the SLD, the majority of the noise was originated from the excess photon noise, of which the theoretical value is calculated to be 3.3mV by assuming the degree of polarization was 0.5, shown in in Table 4-3. The difference between the measured value and the theoretical value may be from the inaccuracy of the degree of the polarization and the estimation of the bandwidth of the light source.

Table 4-3. Noise from the SLD source

Measured	Theoretical		
Total	$\langle i_{th}^2 \rangle$	$\langle i_{sh}^2 \rangle$	$\langle i_{ex}^2 \rangle$
2.63mV	0.06mV	0.20mV	3.38mV

The bandpass filter which followed the SLD helped reduce the bandwidth of the light, as well as the total power. According to Table 4-4, the level of the signal was measured to be 42.6mV and the noise level was 0.95mV, resulting in a SNR of 16.53dB. The SNR is lower because the reduction in the bandwidth significantly increases the portion of the excess photon noise, which is still the main contribution to the total noise, with theoretical value of 0.78 mV.

Table 4-4. Noise after filtering

Measured	Theoretical		
Total	$\langle i_{th}^2 \rangle$	$\langle i_{sh}^2 \rangle$	$\langle i_{ex}^2 \rangle$
0.95mV	0.06mV	0.05 mV	0.78mV

Although the SOA is an optical amplifier and is expected to add additional ASE noise when it is operated in the small gain condition, previous research has shown that, instead of introducing additional noise to the output light, a gain saturated SOA can help suppress intensity noise [73], as was also observed in this system, as Table 4-5 shows. The measured total noise was only around 1/3 of the theoretical value of the excess photon noise and the SNR was 22.12dBm after the modulation of the SOA, while the

theoretical value is 17.38dB. This characteristic of the SOA cannot be taken into account if Equation 4.6 is used.

Table 4-5. Noise after SOA modulation

Measured	Theoretical		
Total	$\langle i_{th}^2 \rangle$	$\langle i_{sh}^2 \rangle$	$\langle i_{ex}^2 \rangle$
3.65mV	0.06mV	0.20 mV	10.88 mV

The output of $EDFA_1$ was also attenuated before measurement because it was too high for direct detection. The measured noise as well as the theoretical values are listed in Table 4-6. Because the noise level was already reduce by the SOA, the actual noise level was much lower than the theoretical value. Although the noise figure of the EDFA was 5dB, which means the SNR will be reduced by 5dB by the amplification, the EDFA did not have this impact. This is because the EDFA was not working under the same condition as the NF was measured. The NF of the EFDA was measured when the EDFA had CW input of less than -15dBm, while in the experiment, its input was pulsed and the peak power was around 10dBm. The EDFA was working under saturated condition and the in-band ASE noise was significantly suppressed. So at the output of $EDFA_1$, the SNR was measured to be 23.3dB. There was out-band ASE noise but it was CW, which was low compared with the low duty cycle pulse signals.

Table 4-6. Noise after $EDFA_1$ amplification

Measured	Theoretical		
Total	$\langle i_{th}^2 \rangle$	$\langle i_{sh}^2 \rangle$	$\langle i_{ex}^2 \rangle$
2.92mV	0.06mV	0.20mV	11.44mV

Figure 4-19 plots the pulse at the output of the SOA and $EDFA_1$, each consisting of 50 traces from consecutive measurements. The quality of the pulse did not change significantly after amplification, as the measured SNR suggested.

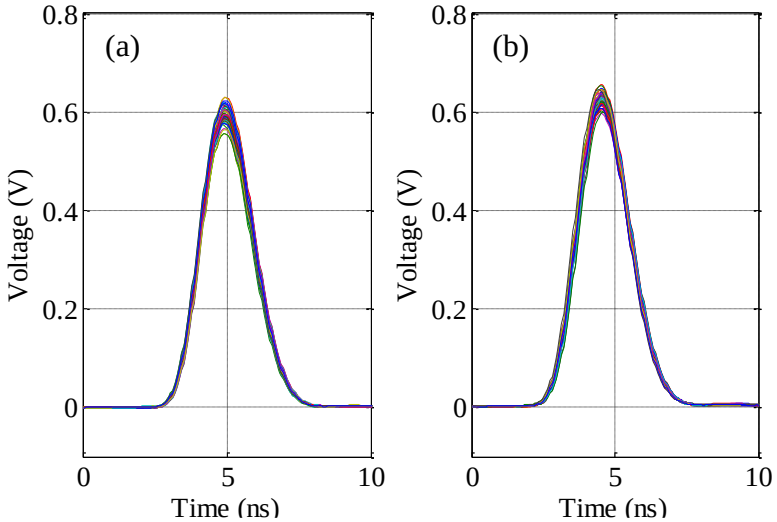

Figure 4-19 50 traces of the pulse at the output of (a) SOA and (b) EDFA

As it is analyzed in Section 4.3.3, the signal to noise ratio will be reduced after reflection because of the Rayleigh backscattering. According to Equation 4.10, the noise figure of the sensor was estimated to be 11dB, so the SNR was supposed to be reduced to about 12.3dB. But because the returned pulses were too weak to be measured, the signals could only be measured after the amplification of $EDFA_2$. Knowing the EDFA has NF of 5dB, the SNR of the signal was expected to be reduced to 7.3dB after amplification.

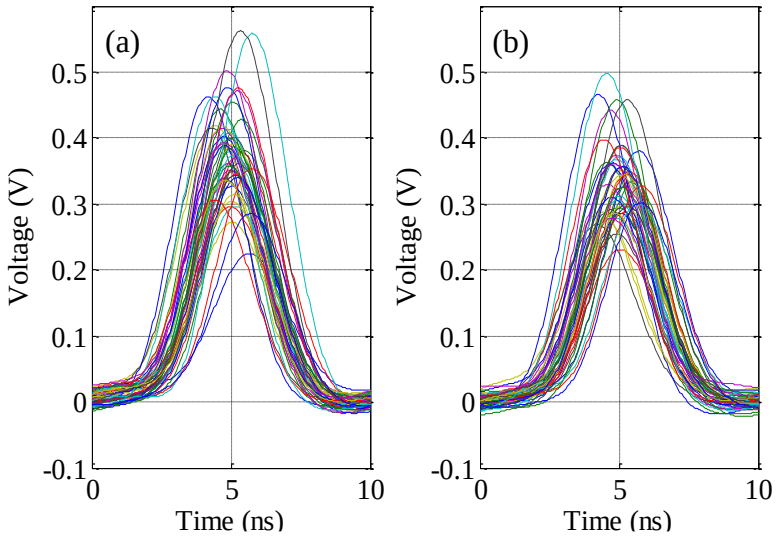

Figure 4-20. 50 traces of the detected pulse by the APD. (a) from Arm1 (b) from Arm2

Figure 4-20 shows 50 traces of the detected signals by the two APDs. It is obvious that the SNR was significantly reduced compared with the pulses in Figure 4-19, and the SNR of the signals from the two detectors were both measured to be 7.6dB, which was close to the estimated value.

In the system, the SNR was reduced most significantly in the process of reflection and amplification, which are inevitable. For a smaller sensing range, stronger FBGs could be used, which help reduce the influence of the Rayleigh backscattering and also increase the input power to the EDFA at the receiving end, both of which can lead to a higher SNR. However it is not an option if a large number of FBGs are required. For the case when FBGs cannot be changed, one way to increase the SNR at the receiving end is to use an EDFA with lower NF, which usually is pre-amplifier. There is a trade-off between the sensing range and the reflectance of the UW-FBGs. So if stronger FBGs are used, alternative solutions should be found to ensure the sensing range remains intact.

One way to extend the sensing range while maintaining the reflectance of the FBGs is illustrated in Figure 4-21. If the bandwidth of the light source permits, two groups of UW-FBGs centered at different wavelengths could be used as the sensing link. This is feasible because the system does not require a bandpass filter at the receiving end. Despite the two sections of the sensing link increase the cost, it is not significant because each of them still consist identical FBGs and they can be fabricated separately and then connected together.

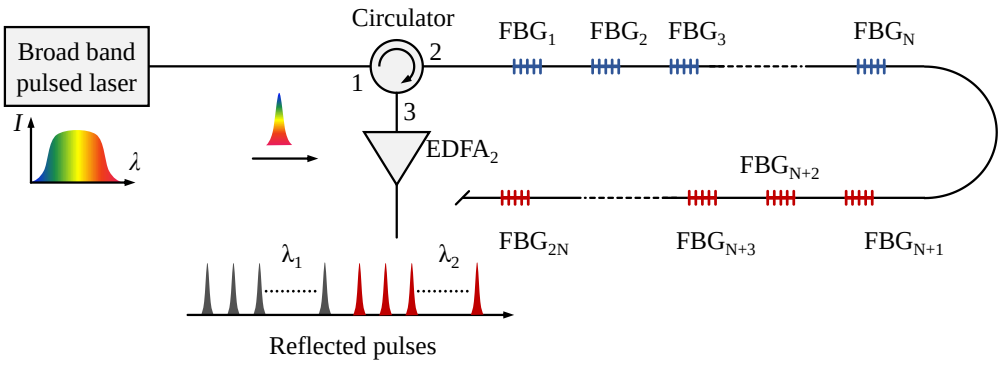

Figure 4-21 Using two groups of FBGs as sensors to extend the sensing range

Although it is expected that the wavelength of the FBGs will shift because of the change of the environment, there is negligible chance that the two groups of FBGs overlap with each other significantly in the spectrum domain.

Chapter 5 Conclusions

In this dissertation, a high-speed fiber sensing system based on time domain multiplexed UW-FBGs is proposed and experimentally demonstrated. The ultra-low reflectance of the UW-FBGs allows a large number of serial gratings to be multiplexed in the sensing link, thus allowing long range measurement. Meanwhile, the detection of the wavelength shift of the FBGs is based on spectral-temporal conversion, which converts the wavelength shift of an FBG to the time delay of the pulses reflected by that FBG. As a result, the time consuming measurement of the spectra of the FBGs is avoided and the system can work at high speed, whose theoretical limit is only dictated by the time of flight of light in the sensing link. The work presented in this dissertation can be summarized as:

Proposal of the sensing system for long distance high speed sensing. This system exploits the chromatic dispersion to convert the wavelength shifts of the UW-FBGs to changes of time delay. An algorithm which has high tolerance of noise was also proposed. Using cross-correlation and curve fitting, the delay calculation can give high quality results while maintaining the high speed and sensing range.

Design and implementation of a complete sensing system. Two types of broadband pulse light sources were built for the system. Two designs of the dispersive unit were proposed, of which the Mach-Zehnder structured dispersive unit requires only one channel of detection, the branch-structured dispersive unit allows higher sensing speed and reduces the complexity of signal processing. The influence of the environment on the dispersive unit was also analyzed and solutions were provided to minimize or eliminate this influence.

Comprehensive system analysis. Various factors that have influence on the system performance including the sensing speed and spatial resolution were analyzed in detail. Simulations were carried out to find out the dependence of the system's performance on the signal to noise ratio, pulse width and data sampling rate. The simulation results showed that the wavelength resolution has exponential dependence on the signal to noise ratio, and the pulse width and sampling rate of the detection also have an impact on the

system performance. These analyses offered a guideline for system implementation and performance optimization.

Proof of concept demonstration. Two regular FBGs were used to demonstrate the proposed concept of high speed FBG interrogation, which intrinsically permits distributed long range sensing. The static and dynamic response of the system were both tested and the ability of high speed sensing was experimentally demonstrated. The dispersion and the strain-delay conversion factor were measured to be -2743ps/nm and -3.36ps/με, respectively. The effectiveness of system performance improvement by data averaging and noise filtering was also investigated in detail.

Full scale sensing system demonstration. A completed sensing system that comprised more than 2,000 UW-FBGs was built and the interrogation of all the serial gratings was carried out with a speed of 20kHz. To our best knowledge, this is the highest speed of more than 2,000 serial FBGs in a single fiber to date. Static response showed a wavelength error less than 20pm and a wavelength standard deviation of 15pm without data averaging. The data averaging was proved to be effective to further improve the system performance. It was also demonstrated that reasonable system performance could still be achieved when the sampling rate of the detection system was reduced the level of commercial low cost ADCs.

Systematic noise analysis. Major noise sources, including the relative intensity noise, Rayleigh backscattering, amplified spontaneous emission and analog to digital quantization, are theoretically analyzed. The signal to noise ratios at different stages of the system were measured and found to be in good agreement with the theoretical predictions. Solutions were also proposed to further improve the performance of the system in the future.

References

1. Ko, J.M. and Y.Q. Ni, *Technology developments in structural health monitoring of large-scale bridges.* Engineering Structures, 2005. **27**(12): p. 1715-1725.
2. Li, H.-N., D.-S. Li, and G.-B. Song, *Recent applications of fiber optic sensors to health monitoring in civil engineering.* Engineering Structures, 2004. **26**(11): p. 1647-1657.
3. Paul, C., et al., *Measurement of crack formation in concrete using embedded optical fibre sensors and differential strain analysis.* Measurement Science and Technology, 2008. **19**(6): p. 065301.
4. Kumagai, Y., et al. *Enhancement of BOCDA system for aircraft health monitoring*. in *SICE Annual Conference, 2008*. 2008.
5. Cusano, A., et al., *Experimental modal analysis of an aircraft model wing by embedded fiber Bragg grating sensors.* IEEE Sensors Journal, 2006. **6**(1): p. 67-77.
6. Lieberman, R.A., L.L. Blyler, and L.G. Cohen, *A distributed fiber optic sensor based on cladding fluorescence.* Lightwave Technology, Journal of, 1990. **8**(2): p. 212-220.
7. Yamate, T. *Fiber-optic sensors for the exploration of oil and gas*. in *2009 14th OptoElectronics and Communications Conference*. 2009.
8. Fu, H.Y., et al., *High pressure sensor based on photonic crystal fiber for downhole application.* Applied Optics, 2010. **49**(14): p. 2639-2643.
9. Nellen, P.M., et al., *Reliability of fiber Bragg grating based sensors for downhole applications.* Sensors and Actuators A: Physical, 2003. **103**(3): p. 364-376.
10. Qi, W., et al., *Multiplexed Fiber-Optic Pressure and Temperature Sensor System for Down-Hole Measurement.* Sensors Journal, IEEE, 2008. **8**(11): p. 1879-1883.
11. Xiao, H., et al., *Fiber optic pressure sensor with self-compensation capability for harsh environment applications.* Optical Engineering, 2005. **44**(5): p. 054403-054403-10.
12. Martinez Manuel, R., M.G. Shlyagin, and S.V. Miridonov, *Location of a time-varying disturbance using an array of identical fiber-optic interferometers interrogated by CW DFB laser.* Optics Express, 2008. **16**(25): p. 20666-20675.
13. Sun, Q., et al., *Distributed fiber-optic vibration sensor using a ring Mach-Zehnder interferometer.* Optics Communications, 2008. **281**(6): p. 1538-1544.
14. Li, X., et al., *Hybrid TDM/WDM-Based Fiber-Optic Sensor Network for Perimeter Intrusion Detection.* Journal of Lightwave Technology, 2012. **30**(8): p. 1113-1120.

15. Fang, N., et al. *Walking intrusion signal recognition method for fiber fence system*. 2009.

16. Kim, D.W., et al., *In-fiber reflection mode interferometer based on a long-period grating for external refractive-index measurement.* Applied Optics, 2005. **44**(26): p. 5368-5373.

17. Lam, C.C.C., et al., *Optical Fiber Refractive Index Sensor for Chloride Ion Monitoring.* IEEE Sensors Journal, 2009. **9**(5): p. 525-532.

18. Kim, D.W., et al., *Simultaneous measurement of refractive index and temperature based on a reflection-mode long-period grating and an intrinsic Fabry–Perot interferometer sensor.* Optics Letters, 2005. **30**(22): p. 3000-3002.

19. Han, M., et al., *Fiber-optic physical and biochemical sensing based on transient and traveling long-period gratings.* Optics Letters, 2009. **34**(1): p. 100-102.

20. Wang, Z. and H. Xiao, *Optical intensity-based long-period fiber grating biosensors and biomedical applications [Life Sciences]*. IEEE Signal Processing Magazine, 2009. **26**(2): p. 121-122, 124-127.

21. Niklès, M., L. Thévenaz, and P.A. Robert, *Simple distributed fiber sensor based on Brillouin gain spectrum analysis.* Optics Letters, 1996. **21**(10): p. 758-760.

22. Liang, H., et al., *High-resolution DPP-BOTDA over 50 km LEAF using return-to-zero coded pulses.* Optics Letters, 2010. **35**(10): p. 1503-1505.

23. Horiguchi, T., et al., *Development of a distributed sensing technique using Brillouin scattering.* Lightwave Technology, Journal of, 1995. **13**(7): p. 1296-1302.

24. Brown, A.W., et al., *Spatial resolution enhancement of a Brillouin-distributed sensor using a novel signal processing method.* Lightwave Technology, Journal of, 1999. **17**(7): p. 1179-1183.

25. Kwang-Yong, S., et al., *Time-Domain Distributed Fiber Sensor With 1 cm Spatial Resolution Based on Brillouin Dynamic Grating.* Lightwave Technology, Journal of, 2010. **28**(14): p. 2062-2067.

26. Bao, X., D.J. Webb, and D.A. Jackson, *32-km distributed temperature sensor based on Brillouin loss in an optical fiber.* Optics Letters, 1993. **18**(18): p. 1561-1563.

27. Bao, X., D.J. Webb, and D.A. Jackson, *Combined distributed temperature and strain sensor based on Brillouinloss in an optical fiber.* Optics Letters, 1994. **19**(2): p. 141-143.

28. Dakin, J.P., et al., *Distributed optical fibre Raman temperature sensor using a semiconductor light source and detector.* Electronics Letters, 1985. **21**(13): p. 569-570.

29. Farahani, M.A. and T. Gogolla, *Spontaneous Raman scattering in optical fibers with modulated probe light for distributed temperature Raman remote sensing.* Lightwave Technology, Journal of, 1999. **17**(8): p. 1379-1391.

30. Hill, W., J. Kübler, and M. Fromme. *Single-mode distributed temperature sensing using OFDR*. 2010.

31. Parvaneh, F., et al., *Forward-scatter frequency-derived distributed optical fibre sensing using the optical Kerr effect.* Electronics Letters, 1992. **28**(12): p. 1080-1082.

32. Dakin, J.P., et al. *A Distributed Fibre Temperature Sensor Using The Optical Kerr Effect*. 1987.

33. Zhang, Z. and X. Bao, *Distributed optical fiber vibration sensor based on spectrum analysis of Polarization-OTDR system.* Optics Express, 2008. **16**(14): p. 10240-10247.

34. Yuelan, L., et al., *Distributed Vibration Sensor Based on Coherent Detection of Phase-OTDR.* Lightwave Technology, Journal of, 2010. **28**(22): p. 3243-3249.

35. Huttner, B., B. Gisin, and N. Gisin, *Distributed PMD Measurement with a Polarization-OTDR in Optical Fibers.* Journal of Lightwave Technology, 1999. **17**(10): p. 1843.

36. Zhou, D.-P., et al., *Distributed vibration sensing with time-resolved optical frequency-domain reflectometry.* Optics Express, 2012. **20**(12): p. 13138-13145.

37. Froggatt, M. and J. Moore, *High-Spatial-Resolution Distributed Strain Measurement in Optical Fiber with Rayleigh Scatter.* Applied Optics, 1998. **37**(10): p. 1735-1740.

38. Soller, B., et al., *High resolution optical frequency domain reflectometry for characterization of components and assemblies.* Optics Express, 2005. **13**(2): p. 666-674.

39. Froggatt, M.E., et al. *Distributed Strain and Temperature Discrimination in Unaltered Polarization Maintaining Fiber*. in *Optical Fiber Sensors*. 2006. Cancun, Mexico: Optical Society of America.

40. Boyd, R.W., *Nonlinear Optics*. Third ed2008: Academic Press.

41. P, A.G., *Nonlinear Fiber Optics*. Fifth ed2013: Academic Press.

42. Mizuno, Y., et al., *Proposal of Brillouin optical correlation-domain reflectometry (BOCDR).* Optics Express, 2008. **16**(16): p. 12148-12153.

43. Song, K.-Y., Z. He, and K. Hotate. *Distributed Strain Measurement with Millimeter-Order Spatial Resolution Based on Brillouin Optical Correlation Domain Analysis and Beat Lock-in Detection Scheme*. in *Optical Fiber Sensors*. 2006. Cancun, Mexico: Optical Society of America.

44. Barnoski, M.K., et al., *Optical time domain reflectometer.* Applied Optics, 1977. **16**(9): p. 2375-2379.

45. Han, M., Y. Wang, and A. Wang, *Grating-assisted polarization optical time-domain reflectometry for distributed fiber-optic sensing.* Optics Letters, 2007. **32**(14): p. 2028-2030.

46. Eickhoff, W. and R. Ulrich, *Optical frequency domain reflectometry in single-mode fiber.* Applied Physics Letters, 1981. **39**(9): p. 693-695.

47. Kaur, A., et al., *Microcavity strain sensor for high temperature applications.* Optical Engineering, 2014. **53**(1): p. 017105-017105.

48. Juncheng, X., et al., *Miniature temperature-insensitive Fabry-Pe/spl acute/rot fiber-optic pressure sensor.* Photonics Technology Letters, IEEE, 2006. **18**(10): p. 1134-1136.

49. Wenyuan, W., et al., *Quasi-Distributed IFPI Sensing System Demultiplexed With FFT-Based Wavelength Tracking Method.* Sensors Journal, IEEE, 2012. **12**(9): p. 2875-2880.

50. Chan, C.C., et al., *Intrinsic crosstalk analysis of a serial TDM FGB sensor array by using a tunable laser.* Microwave and Optical Technology Letters, 2003. **36**(1): p. 2-4.

51. Cooper, D.J.F., T. Coroy, and P.W.E. Smith, *Time-Division Multiplexing of Large Serial Fiber-Optic Bragg Grating Sensor Arrays.* Applied Optics, 2001. **40**(16): p. 2643-2654.

52. Yunmiao, W., et al., *A Quasi-Distributed Sensing Network With Time-Division-Multiplexed Fiber Bragg Gratings.* Photonics Technology Letters, IEEE, 2011. **23**(2): p. 70-72.

53. Hu, C., H. Wen, and W. Bai, *A Novel Interrogation System for Large Scale Sensing Network With Identical Ultra-Weak Fiber Bragg Gratings.* Journal of Lightwave Technology, 2014. **32**(7): p. 1406-1411.

54. Sano, Y. and T. Yoshino, *Fast optical wavelength interrogator employing arrayed waveguide grating for distributed fiber Bragg grating sensors.* Lightwave Technology, Journal of, 2003. **21**(1): p. 132-139.

55. Huang, J.-T., X.-G. Huang, and H.-W. Zhao, *A Distributed Fibre Bragg Grating Sensor Interrogator Employing a Reformative Arrayed Waveguide Grating.* Chinese Physics Letters, 2008. **25**(4): p. 1329.

56. Koo, K.P., A.B. Tveten, and S.T. Vohra, *Dense wavelength division multiplexing of fibre Bragg grating sensors using CDMA.* Electronics Letters, 1999. **35**(2): p. 165-167.

57. A., C.B., et al., *Use of 3000 Bragg Grating Strain Sensors Distributed on Four Eight-Meter Optical Fibers During Static Load Tests of a Composite Structure*, 2001, NASA Langley Technical Report Server.

58. Fu, H.Y., et al., *High-speed fibre Bragg grating sensor interrogation using dispersion compensation fibre.* Electronics Letters, 2008. **44**(10): p. 618-619.

59. Haiyun, X., et al., *Ultrafast and Precise Interrogation of Fiber Bragg Grating Sensor Based on Wavelength-to-Time Mapping Incorporating Higher Order Dispersion.* Lightwave Technology, Journal of, 2010. **28**(3): p. 254-261.

60. Chao, W. and Y. Jianping, *Ultrafast and Ultrahigh-Resolution Interrogation of a Fiber Bragg Grating Sensor Based on Interferometric Temporal Spectroscopy.* Lightwave Technology, Journal of, 2011. **29**(19): p. 2927-2933.

61. Goda, K. and B. Jalali, *Dispersive Fourier transformation for fast continuous single-shot measurements.* Nat Photon, 2013. **7**(2): p. 102-112.

62. Guo, H., et al., *On-line writing identical and weak fiber Bragg grating arrays.* Chinese Optics Letters, 2013. **11**(3): p. 030602.

63. Cao, B., et al., *Dispersion Compensating Fibers with Improved Splicing Performance.* Physics Procedia, 2013. **48**: p. 96-101.

64. Basu, M. and S. Roy, *Design considerations of depressed clad W-shaped single mode dispersion compensating fibers.* Optik - International Journal for Light and Electron Optics, 2006. **117**(8): p. 377-387.

65. Gérôme, F., J.L. Auguste, and J.M. Blondy, *Design of dispersion-compensating fibers based on a dual-concentric-core photonic crystal fiber.* Optics Letters, 2004. **29**(23): p. 2725-2727.

66. Yi, N., et al., *Dual-core photonic Crystal fiber for dispersion compensation.* IEEE Photonics Technology Letters, 2004. **16**(6): p. 1516-1518.

67. Ouellette, F., *Dispersion cancellation using linearly chirped Bragg grating filters in optical waveguides.* Optics Letters, 1987. **12**(10): p. 847-849.

68. Lachance, R.L., S. Lelièvre, and Y. Painchaud. *50 and 100GHz Multi-Channel Tunable Chromatic Dispersion Slope Compensator*. in *Optical Fiber Communication Conference*. 2003. Atlanta, Georgia: Optical Society of America.

69. Kashyap, R., *Fiber Bragg gratings*. Second ed2009: Academic Press.

70. Erdogan, T., *Cladding-mode resonances in short- and long-period fiber grating filters.* Journal of the Optical Society of America A, 1997. **14**(8): p. 1760-1773.

71. Qiu, Y. and Y. Sheng, *Fiber Bragg Grating Modeling.*

72. Jewell, J.M., *Thermooptic coefficients of some standard reference material glasses.* Journal of the American Ceramic Society, 1991. **74**(7): p. 1689-1691.

73. Shin, S., et al., *Characterization and Analysis of Relative Intensity Noise in Broadband Optical Sources for Optical Coherence Tomography.* IEEE Photonics Technology Letters, 2010. **22**(14): p. 1057-1059.

74. Haus, H.A., *The noise figure of optical amplifiers.* IEEE Photonics Technology Letters, 1998. **10**(11): p. 1602-1604.